UNDERSTANDING THE EFFECT OF CRYSTALLINE STRUCTURE AND ATOMIC ARRANGEMENT IN METAL OXIDE ELECTRODES FOR SODIUM ION BATTERIES

by

Changjian Deng

A dissertation

submitted in partial fulfillment

of the requirements for the degree of

Doctor of Philosophy in Materials Science and Engineering

Boise State University

May 2019

BOISE STATE UNIVERSITY GRADUATE COLLEGE

DEFENSE COMMITTEE AND FINAL READING APPROVALS

of the dissertation submitted by

Changjian Deng

Dissertation Title: Understanding the Effect of Crystalline Structure and Atomic Arrangement in Metal Oxide Electrodes for Sodium Ion Batteries

Date of Final Oral Examination: 04 December 2018

The following individuals read and discussed the dissertation submitted by student Changjian Deng, and they evaluated his presentation and response to questions during the final oral examination. They found that the student passed the final oral examination.

Hui (Claire) Xiong, PhD	Chair, Supervisory Committee
Eungje Lee, PhD	Member, Supervisory Committee
Yanliang Zhang, PhD	Member, Supervisory Committee
David Estrada, PhD	Member, Supervisory Committee

The final reading approval of the dissertation was granted by Hui (Claire) Xiong, PhD, Chair of the Supervisory Committee. The dissertation was approved by the Graduate College.

ACKNOWLEDGEMENTS

First, I would like to thank my parents who raised me up and offered me the best at every effort. Second, I would like to thank Dr. Hui (Claire) Xiong who chose me as a graduate student at Boise State University. I thank her for providing me with thoughtful mentorship and generous funding resources to support my training toward my Ph.D degree. I also thank her training on my technical skills and professional connections.

Furthermore, I would like to thank the rest of committee members, Dr. Eungje Lee, Dr. David Estrada and Dr. Yanliang Zhang, for their kind guidance on my research projects. Particularly, I would like to thank Dr. Eungje Lee who provided me with important technical skills and instructive comments on my cathode projects. I also thank the collaborators, Dr. Yang Ren, Dr. Hua Zhou, Dr. Yuzi Liu, Dr. Wenqian Xu, Dr. Jing Xu, Dr. Wei Tong, for their contribution of advanced data collection and analysis.

Moreover, I would like to thank the group members at Electrochemical Energy Materials lab for their help. Particularly, I would like to thank Dr. Kassiopeia Smith, Paige Skinner and Andy Lau who supported me with great deal of technical and personal assistance. I would also thank the office staff for the administrative assistance and the local funding from Boise State University to fulfill the research.

Last but not least, I would like to thank the financial support from National Science Foundation under Grant No. DMR-1454984 and U.S. Department of Energy, Office of Science, Office of Basic Energy Sciences program under Award DE-SC0019121.

ABSTRACT

This dissertation investigates the fundamental understanding in the influences of order-disorder and atomic arrangement on electrochemical properties of electrode materials for sodium ion batteries (SIBs). In specific, TiO_2 anode and $NaNi_xFe_yMn_xO_2$ cathode materials are studied. Due to their low cost and relatively high abundance of raw materials SIBs are attractive for large-scale energy storage systems for high round trip efficiency and long cycle life. Recent studies suggest that various polymorphs of TiO_2 are suitable as anode material. However, the impact of crystallinity on the electrochemical properties of the material has not been explored. Meanwhile, the $NaNi_xFe_yMn_xO_2$ cathode exhibits promising performance but detrimental irreversibility at high voltages as well as poor cycling stability and rate capability remain issues for its practical application.

This dissertation presents the study which suggests that the increase of crystallinity in anatase TiO_2 nanoparticle electrode leads to better electrochemical performance in terms of Coulombic efficiency, rate capability and cycle life. To understand the discrepancy in performance, various structural and electrochemical characterizations are conducted to explore the Na ion diffusion process and the local structural evolution of the material. Metal oxide cathode is also investigated. The atomic rearrangement of transition metals in $NaNi_xFe_yMn_xO_2$ at high voltages attributes to irreversibility and instability. It becomes significant with the increase of either Fe composition or upper cut-off operation voltage. X-ray spectroscopy is used to investigate the oxidation state and local environment of the transition metals. The result suggests that

the redox and bonding activity of Ni-O mainly attributes to irreversibility and instability. In addition, intergrown phases have been shown to improve structural stability and Na mobility in layered cathode materials. A new Li-substituted $NaNi_xFe_yMn_xO_2$ intergrowth cathode is designed and synthesized. The improvement in stability and rate capability of the new intergrowth cathode is investigated, which is associated with the mixed layered-spinel phase that possibly offers improved ion diffusion and stability through direct channels between the 2D layered and 3D spinel component.

TABLE OF CONTENTS

LIST OF TABLES

LIST OF FIGURES

LIST OF ABBREVIATIONS

ESS	Energy Storage Systems
SIB	Sodium Ion Batteries
TiO_2	Titanium Oxide
mAh	milliamp-hour
TiO_2-(B)	TiO_2 Bronze
TM	Transition Metal
NCM	$LiNi_yCo_xMn_yO_2$
XRD	X-Ray Diffraction
BMS	Battery Management System
NaNFM	$Na_{1.05}Ni_yFe_xMn_yO_2$
PDF	Pair Distribution Function
XAS	X-ray Absorption Spectroscopy
GITT	Galvanostatic Intermittent Titration Technique
CV	Cyclic Voltammetry
A-TiO_2	Amorphous TiO_2
PC-TiO_2	Partially-Crystalline anatase TiO_2
FC-TiO_2	Fully-Crystalline anatase TiO_2
NFM-Fe1/3	$Na_{1.05}Ni_{1/3}Fe_{1/3}Mn_{1/3}O_2$
NFM-Fe0.5	$Na_{1.05}Ni_{0.25}Fe_{0.5}Mn_{0.25}O_2$
NFM-Fe0.8	$Na_{1.05}Ni_{0.1}Fe_{0.8}Mn_{0.1}O_2$

Fe1/3-2-4	$Na_{1.05}Ni_{1/3}Fe_{1/3}Mn_{1/3}O_2$ cycled between 2.0V-4.0V
Fe1/3-2-4.3	$Na_{1.05}Ni_{1/3}Fe_{1/3}Mn_{1/3}O_2$ cycled between 2.0V-4.3V
Fe08-2-4	$Na_{1.05}Ni_{0.1}Fe_{0.8}Mn_{0.1}O_2$ cycled between 2.0V-4.0V
TEM	Transmission Electron Microscopy
SAED	Selected Area Electron Diffraction
HRTEM	High-Resolution Transmission Electron Microscopy
NFM	$NaNi_{0.4}Fe_{0.2}Mn_{0.4}O_2$
LS-NFM	$Na_{0.87}Li_{0.25}Ni_{0.4}Fe_{0.2}Mn_{0.4}O_{2+\delta}$
3D	Three-Dimensional
CCP	Cubic Close-Packed
NASICON	NA Super Ionic CONductor
eV	electron Volts
sXAS	soft X-ray Absorption Spectroscopy
TEY	Total Electron Yield
TFY	Total Fluorescence Yield
XANES	X-ray Absorption Near Edge Structure
NEXAFS	Near Edge X-ray Absorption Fine Structure
EXAFS	Extended X-ray Absorption Fine Structure
HOMO	Highest Occupied Molecular Orbital
LUMO	Lowest Unoccupied Molecular Orbital
SEI	Solid Electrolyte Interface
C_g	Gravimetric theoretical capacity
C_v	Volumetric theoretical capacity

CE	Coulombic Efficiency
ED	Energy Density
GITT	Galvanostatic Intermittent Titration Technique
ΔE_p	Peak-to-peak separation
TBOT	Tetrabutyl orthotitanate
HPC	Hydroxypropyl cellulose
DI	De-Ionized
PC	Propylene Carbonate
CMC	Carboxymethylcellulose
FWHM	Full Width at Half Maximum
ICP	Inductively Coupled Plasma
GSAS	General Structure Analysis System
PVDF	Poly(vinylidene fluoride)
SOC	State Of Charge
LMCT	Ligand-to-Metal Charge Transfer
$E_{0,Ni}$	Energy of first inflection point of Ni
$E_{0,Fe}$	Energy of first inflection point of Fe
TM-O	Transition Metal-Oxygen
TM-TM	Transition Metal- Transition Metal
FFT	Fast Fourier Transform
BET	Brunauer-Emmett-Teller

CHAPTER ONE: INTRODUCTION

1.1 Dissertation Overview

This dissertation is composed of six chapters. Chapter one describes the motivation of this dissertation. The objective for this dissertation is to understand the effect of structural order-disorder and atomic arrangement in metal oxide electrodes for their application in sodium-ion batteries (SIBs). Metal oxides (e.g., TiO_2 and layered oxide) that are candidates for both anode and cathode materials for SIBs are investigated. The structure-processing-performance relationship of the metal oxide electrode materials under study is established with the aid of advanced electrochemical, structural and spectroscopic characterization. Chapter 2 of this dissertation outlines the background information, including the working principles of SIBs, current research related to titanium dioxide (TiO_2) anode and layered oxide cathode materials. Chapter 3 presents the details of experimental procedures. Chapter 4 describes the systematic study of the impact of crystallinity in the charge storage and transport mechanism of anatase TiO_2 nanoparticles anode. Chapter 5 presents the investigation of the origin of irreversibility in layered oxide cathode materials. Chapter 6 discusses the design and synthesis of a new Li-substituted layered-spinel intergrowth cathode material and the fundamental understanding of its charge compensation mechanism as well as the causes of its structural stability.

1.2 Motivation

Large scale energy storage systems (ESS) have become increasingly important for intermittent renewable energy sources, such as wind and solar, used for the electrical grid.[1] Among different types of ESSs, rechargeable battery technology is attractive due to its high round trip efficiency, long cycle life and low maintenance.[2] Lithium ion batteries have dominated the rechargeable battery market for decades. However, the surging demand of lithium ion batteries in the electric vehicle market with the limited and geographically-constrained lithium mineral reserves has driven up the price. Therefore, there is an urgent need to explore low-cost and stable rechargeable batteries based on abundant resources. Among all candidates SIBs manufactured with low cost and abundant raw materials, are promising due to the similar chemistry and technology as lithium ion batteries.[2-4] It has been reported that different polymorphs of TiO_2 are promising for anode materials but the influence of degree of ordering on the electrochemical performance is seldom explored. In addition, $NaNi_xFe_yMn_xO_2$ cathode exhibits attractive performance but the harmful irreversibility as well as poor rate capability and cycle life impede the commercial application.

We believe the crystalline structure and atomic arrangement of electrode materials have significant impact on their electrochemical performance. Therefore, the impact of crystallinity on anatase TiO_2 anode material is investigated. Moreover, the atomic arrangement in $NaNi_xFe_yMn_xO_2$ cathode is studied to understand the origin of irreversibility in this material. We also develop a new layered-spinel intergrowth cathode to improve the rate capability and cycle life.

1.2.1 The Impact of Crystallinity on Anatase TiO_2 Anode Material

Graphite has been the state-of-the-art anode for lithium ion batteries, however, it cannot incorporate the large sodium ions (1.02 Å) within its layered structure.[5] Therefore, efforts have been made to search for new anode materials for SIB. Hard carbon has been intensively studied but its low insertion voltage (0-0.1V) is close to the sodium plating voltage, which leads to dendrite formation and unsafe operation.[6] Alloy-type anodes including P, Sn and Sb, deliver higher specific capacities but suffer from large volume expansions which leads to large irreversible capacity and poor cycle life.[7-9] Organic materials are also investigated as the anode materials for SIB, but they have limitations due to poor electronic conductivity and dissolution in the organic electrolyte.[10,11]

TiO_2 anode materials are promising due to the safe operation voltage, stable structure during the charging and discharging process, and acceptable electronic conductivity.[12] Amorphous[13], anatase[14-18], bronze[19] and rutile[20] TiO_2 materials have been studied for SIB. Although amorphous, single-phased, binary mixed-phased[21] crystalline TiO_2 materials have been investigated, the impact of crystallinity on sodium (de)insertion into TiO_2 is underexplored. Therefore, we conducted a systematic study of crystallinity effect on electrochemical charge storage properties of mesoporous TiO_2 nanoparticle anode.

1.2.2 The Origin of Irreversibility in Layered Cathode Materials

In terms of cathode materials in sodium ion batteries, layered oxides are of great interest due to their high theoretical capacity and the abundance, low-cost, and environmentally-friendliness of the raw materials.[22] The electrochemical performance of $NaFeO_2$ has been significantly improved by substitution of Fe ions by other transition

metals (TMs).[23] Although various TMs have been studied as the dopants[23], nickel and manganese substitution is particularly attractive because the $NaNi_yFe_xMn_yO_2$ cathode exhibits enhanced electrochemical performance and structural stability.

The practical application of a $NaNi_yFe_xMn_yO_2$ cathode has been limited by the significant irreversibility during the cycling process. The irreversibility can reduce the energy density of the cell,[25] complicates the battery management system (BMS),[25] and leads to a low round-trip efficiency.[26] In this dissertation, we used a $NaNi_yFe_xMn_yO_2$ cathode as a model system to study origin of the irreversibility in various cation compositions and different voltage windows.

1.2.3 Li-substituted Layered-Spinel Cathode Material

Due to their high theoretical capacities, the technology of O3-type layered $NaNi_yFe_xMn_yO_2$ cathodes for SIBs has rapidly developed, however, the cycling stability of such materials especially at high voltages (above 4.0 V vs. Na/Na^+) remains an issue.[27] Recently, several groups have reported that the overall electrochemical performance of O3-type layered cathodes can be enhanced by lithium substitution.[28-31] In addition to the single-phased Li-substituted O3-type layered cathodes, Lee et al. varied the Li content and obtained the layered P2/O3 intergrowth cathode that exhibited a synergistic effect to improve Na^+ diffusion for high rate performance.[32]

Aside from the layered intergrowth cathodes, Gao et al. reported a novel design of mixed layered-tunneled P2+T phase $Na_xCo_{0.1}Mn_{0.9}O_2$ ($0.44 \leq x \leq 0.7$) with interface-rich characteristic for high performance sodium storage, whereby the tunneled T phase offers fast Na ion diffusivity and excellent structural stability and the layered P2 phase contributes to high specific capacity.[33]

In addition to T phase, the post-spinel $NaMn_2O_4$ cathode material with tunneled structure showed high structural stability and Na mobility for sodium ion batteries based on both computational and experimental studies.[34,35]

Inspired by the advantages of O3-$Na(Ni_xFe_yMn_z)O_2$ cathode materials, the design strategies of Li substitution, layered-tunneled intergrown phases and tunneled spinel phase with improved structural stability and Na mobility, we develop a Li-substituted layered-tunneled O3/spinel $Na(Ni_xFe_yMn_z)O_2$ cathode material, $Na_{0.87}Li_{0.25}Ni_{0.4}Fe_{0.2}Mn_{0.4}O_{2+\delta}$ (LS-NFM) for enhanced sodium ion storage and cycling stability.

1.3 References

(1) Slater, M. D.; Kim, D.; Lee, E.; Johnson, C. S. *Adv Funct Mater* **2013**, *23*, 947.

(2) Kundu, D.; Talaie, E.; Duffort, V.; Nazar, L. F. *Angew Chem Int Edit* **2015**, *54*, 3431.

(3) Pan, H. L.; Hu, Y. S.; Chen, L. Q. *Energ Environ Sci* **2013**, *6*, 2338.

(4) Kim, S. W.; Seo, D. H.; Ma, X. H.; Ceder, G.; Kang, K. *Adv Energy Mater* **2012**, *2*, 710.

(5) Wen, Y.; He, K.; Zhu, Y. J.; Han, F. D.; Xu, Y. H.; Matsuda, I.; Ishii, Y.; Cumings, J.; Wang, C. S. *Nat Commun* **2014**, *5*.

(6) Stevens, D. A.; Dahn, J. R. *J Electrochem Soc* **2000**, *147*, 1271.

(7) Qian, J. F.; Wu, X. Y.; Cao, Y. L.; Ai, X. P.; Yang, H. X. *Angew Chem Int Edit* **2013**, *52*, 4633.

(8) Xu, Y. H.; Zhu, Y. J.; Liu, Y. H.; Wang, C. S. *Adv Energy Mater* **2013**, *3*, 128.

(9) Zhu, Y. J.; Han, X. G.; Xu, Y. H.; Liu, Y. H.; Zheng, S. Y.; Xu, K.; Hu, L. B.; Wang, C. S. *Acs Nano* **2013**, *7*, 6378.

(10) Song, Z. P.; Zhou, H. S. *Energ Environ Sci* **2013**, *6*, 2280.

(11) Song, Z. P.; Qian, Y. M.; Zhang, T.; Otani, M.; Zhou, H. S. *Adv Sci* **2015**, *2*.

(12) Guo, S. H.; Yi, J.; Sun, Y.; Zhou, H. S. *Energ Environ Sci* **2016**, *9*, 2978.

(13) Xiong, H.; Slater, M. D.; Balasubramanian, M.; Johnson, C. S.; Rajh, T. *J Phys Chem Lett* **2011**, *2*, 2560.

(14) Wu, L. M.; Buchholz, D.; Bresser, D.; Chagas, L. G.; Passerini, S. *J Power Sources* **2014**, *251*, 379.

(15) Wu, L. M.; Bresser, D.; Buchholz, D.; Giffin, G. A.; Castro, C. R.; Ochel, A.; Passerini, S. *Adv Energy Mater* **2015**, *5*.

(16) Li, W.; Fukunishi, M.; Morgan, B. J.; Borkiewicz, O. J.; Chapman, K. W.; Pralong, V.; Maignan, A.; Lebedev, O. I.; Ma, J. W.; Groult, H.; Komaba, S.; Damboumet, D. *Chem Mater* **2017**, *29*, 1836.

(17) Myung, S. T.; Takahashi, N.; Komaba, S.; Yoon, C. S.; Sun, Y. K.; Amine, K.; Yashiro, H. *Adv Funct Mater* **2011**, *21*, 3231.

(18) Kim, K. T.; Ali, G.; Chung, K. Y.; Yoon, C. S.; Yashiro, H.; Sun, Y. K.; Lu, J.; Amine, K.; Myung, S. T. *Nano Lett* **2014**, *14*, 416.

(19) Huang, J. P.; Yuan, D. D.; Zhang, H. Z.; Cao, Y. L.; Li, G. R.; Yang, H. X.; Gao, X. P. *Rsc Adv* **2013**, *3*, 12593.

(20) Gu, X.; Li, L. J.; Wang, Y.; Dai, P. C.; Wang, H. B.; Zhao, X. B. *Electrochim Acta* **2016**, *211*, 77.

(21) Su, D. W.; Dou, S. X.; Wang, G. X. *Chem Mater* **2015**, *27*, 6022.

(22) Xiang, X. D.; Zhang, K.; Chen, J. *Adv Mater* **2015**, *27*, 5343.

(23) Yabuuchi, N.; Kubota, K.; Dahbi, M.; Komaba, S. *Chem Rev* **2014**, *114*, 11636.

(24) Kasai, M.; Nishimura, S.; Gunji, A.; Konishi, H.; Feng, X. L.; Furutsuki, S.; Takahashi, S. *Electrochim Acta* **2014**, *146*, 79.

(25) Croy, J. R.; Gallagher, K. G.; Balasubramanian, M.; Chen, Z. H.; Ren, Y.; Kim, D.; Kang, S. H.; Dees, D. W.; Thackeray, M. M. *J Phys Chem C* **2013**, *117*, 6525.

(26) Li, L. S.; Jacobs, R.; Gao, P.; Gan, L. Y.; Wang, F.; Morgan, D.; Jin, S. *J Am Chem Soc* **2016**, *138*, 2838.

(27) Li, X.; Wu, D.; Zhou, Y. N.; Liu, L.; Yang, X. Q.; Ceder, G. *Electrochem Commun* **2014**, *49*, 51.

(28) Zhang, S. M.; Liu, Y.; Zhang, N.; Zhao, K.; Yang, J. H.; He, S. Y. *J Power Sources* **2016**, *329*, 1.

(29) Oh, S. M.; Myung, S. T.; Hwang, J. Y.; Scrosati, B.; Amine, K.; Sun, Y. K. *Chem Mater* **2014**, *26*, 6165.

(30) Zheng, S. Y.; Zhong, G. M.; McDonald, M. J.; Gong, Z. L.; Liu, R.; Wen, W.; Yang, C.; Yang, Y. *J Mater Chem A* **2016**, *4*, 9054.

(31) Xu, J.; Liu, H. D.; Meng, Y. S. *Electrochem Commun* **2015**, *60*, 13.

(32) Lee, E.; Lu, J.; Ren, Y.; Luo, X. Y.; Zhang, X. Y.; Wen, J. G.; Miller, D.; DeWahl, A.; Hackney, S.; Key, B.; Kim, D.; Slater, M. D.; Johnson, C. S. *Adv Energy Mater* **2014**, *4*.

(33) Gao, G.; Tie, D.; Ma, H.; Yu, H.; Shi, S.; Wang, B.; Xu, S.; Wang, L.; Zhao, Y. *J Mater Chem A* **2018**, *6*, 6675.

(34) Liu, X. Z.; Wang, X.; Iyo, A.; Yu, H. J.; Li, D.; Zhou, H. S. *J Mater Chem A* **2014**, *2*, 14822.

(35) Ling, C.; Mizuno, F. *Chem Mater* **2013**, *25*, 3062.

CHAPTER TWO: BACKGROUND INFORMATION

2.1 Working Principle of Sodium Ion Batteries

The sodium ion battery operates in a "rocking chair" fashion, which is illustrated in Figure 2.1. The basic components of a sodium ion battery include the anode (negative electrode), the cathode (positive electrode) and the electrolyte. There is a separator between the anode and cathode, which allows electrolyte to pass through but physically separates the anode and cathode. When the battery is discharging, sodium ions move within the ion-conducting electron-impeding electrolyte internally from anode to cathode, at the same time the electrons travel through an external circuit from the anode to cathode producing electricity, and *vice versa*.

2.2 TiO_2 Anode Materials for Sodium Ion Batteries

Titanium dioxide is the most common form of titanium compounds with stable, environmentally-friendly, abundant and inexpensive features. These features make TiO_2 particularly attractive as the anode for large-scale sodium ion batteries. TiO_2 is composed of Ti^{4+} ions with TiO_6 octahedra. The different connection of TiO_6 octahedra leads to different polymorphs including anatase, bronze, and rutile (Figure 2.2). At bulk scale, rutile is the most thermodynamically stable polymorph while anatase and bronze are metastable phases.[1] However, at nanoscale where the size is below 20 nm, the most stable phase is anatase.[2] The phase transition from anatase to rutile occurs under the heat treatment where the temperature reaches 600 ^oC.[3] Rutile features in a tetragonal symmetry with the space group $P4_2/mnm$.[4] The TiO_6 octahedra shares edges along the *c*-

direction and the corners locate along the *ab*-planes.[4] There is a minor orthorhombic distortion in the TiO_6 octahedra.[5] Bronze characterizes a monoclinic structure with C2m symmetry with the sheets of both edge and corner sharing TiO6 polygons.[6] Anatase has the tetragonal structure with the space group I41/amd, where the distorted edge-sharing TiO6 octahedra are stacked in one-dimensional zig-zag chains.[7]

Amorphous[8], anatase[9-13], bronze[14] and rutile[15] TiO_2 materials have been studied for SIB. Xiong et al. directly grew amorphous TiO_2 nanotubes on the current collector without binders and additives, and the electrochemical performance was evaluated within a sodium half-cell, and it was found that only nanotubes with larger diameters (>80 nm I.D.) can host sodium ions.[8] The amorphous TiO_2 nanotube electrode exhibited 150 mAh g^{-1} at 0.05 A g^{-1} cycled between 2.5 – 0.9 V vs. Na/Na^+. Wu et al. prepared anatase TiO_2 nanoparticles for high power sodium ion batteries, where 100 mAh g^{-1} at 5.5C cycled between 2.0 – 0.02 V vs. Na/Na^+ was obtained after 1000 cycles without significant capacity decay.[9] Furthermore, they investigated the sodium ion insertion process and proposed a new reaction mechanism that sodium ions partially reduce the stable titanium oxide and form metallic titanium, sodium oxide, and amorphous sodium titanate.[10] The newly-formed amorphous sodium titanate contributes to the most of reversible capacity.[10] Moreover, Li et al. investigated the sodium insertion/extraction mechanism in anatase TiO_2, where sodium ion insertion leads to the phase transition from anatase ($I4_1/amd$) to layered Na_xTiO_2 (R-3m) with high degree of disorder, and the local structure of the anatase was recovered with short-range order after sodium extraction.[11] Huang et al. reported TiO_2(B) nanotubes with a 50 mAh g^{-1} capacity after 90 cycles obtained and identified that the sodium insertion along (001) interlayer plane.[14] Gu et al. prepared

hierarchical tubular rutile TiO_2 nanorods with a high reversible capacity of 79 mAh g^{-1} at 0.3C after 1000 cycles.[15] In addition to the pure phase, Su et al. compared the electrochemical performance of amorphous, mixed anatase/rutile and pure anatase TiO_2 hollow nanospheres in SIB.[16] It was found that pure anatase exhibited a higher specific capacity than amorphous or anatase/rutile TiO_2 materials because: 1) pure anatase crystalline structure has a two-dimensional diffusion path and more active sites; 2) anatase has a lower diffusion barrier for sodium insertion suggested by density functional theory.[16]

2.3 Layered Cathode Materials for Sodium Ion Batteries

Layered sodium metal oxides adopt the α-$NaFeO_2$ structure and are built up of ordered stacking of TMO_2 (TM: transition metal) layers with edge-sharing TMO_6 octahedra with different orientations along the *c*-axis direction. According to the classification proposed by Delmas et al.[17], The polymorphs of layered oxides can be categorized in terms of (1) a capital letter indicating the surrounding of the interlayer alkali species (O for octahedral, T for tetragonal, and P for prismatic) and (2) a value that equals to the number of MO_2 layers needed for periodicity (Figure 2.3 and Figure 2.4). Among the research of sodium cathode materials two types of layered structures, P2 and O3, were intensively studied (Figure 2.3, Figure 2.4 and Table 2.1).

Both P2 and O3 types consist of cubic close-packed (CCP) oxygen arrays as a basic matrix where one TM atom coordinates with six oxygen atoms to form an octahedron. These octahedra share edges to form TMO_2 layers, leaving octahedral or trigonal prismatic sites between each layer to accommodate sodium ions. When sodium ions are sufficient compared to TM ions (e.g., Na/TM=1), sodium ions take up octahedral

sites to form O3 type structure, along with the oxygen stacking pattern AB-CA-BC. Note that vacancies located at tetrahedral sites face-shared with TM and Na octahedra also exist in O3 type structure. On the other hand, if the amount of sodium ions is insufficient (Na/TM<1), sodium ions tend to sit at prismatic sites with oxygen stacking pattern AB-BA (P2 type). Note that since the radius of sodium ions is much larger than that of TMs, sodium ions can barely migrate to TMO_2 layers. Only one type of sodium ion occupancy exists in O3 structure, where NaO_6 octahedra are all sharing edges with TMO_6 octahedra. However, in P2 structures two types of sodium ion occupancy have been observed, Na (2d) and Na (2b), sharing faces with the upper and lower TMO_6 octahedrons and sharing edges with six TMO_6 octahedra, respectively[18].

Due to the distinct difference of sodium ion coordination in P2 and O3 structure, the mechanism of sodium ions (de)intercalation is also different in these structures. In O3 structure, direct migration of sodium ions from one octahedral site to the adjacent octahedral site requires high activation energy to overcome, thus sodium ions travel through interstitial tetrahedral sites (Figure 2.3). However, in P2 systems, there are open channels with lower diffusion barriers for sodium ion migration, leading to the direct migration from one prismatic site to the adjacent one (Figure 2.4). These different diffusion mechanisms lead to a higher ionic conductivity in P2 structure than that in O3 structure for samples containing similar chemical composition.[19]

Sodium ion migration in both O3 and P2 structures triggers the phase transition by the gliding of TMO_2 layers through vector (1/3, 2/3, 0) without breaking TM-O bonds.[20] With partial extraction of sodium ions during charging process, O3 structure gradually transits to P3 structure, namely sodium ions are located at prismatic sites with

an O stacking pattern of AB-BC-CA. For P2 structure, Na de-intercalation (extraction) leads to phase transition from P2 type to O2 type, where sodium ions are located at octahedral sites with O stacking pattern of AB-AC. The phase transition in both types plays a crucial role in their electrochemical performance. Particularly, the reversibility of the phase transition directly affects the stability of materials during Na intercalation and extraction, which largely influences on the capacity and voltage retention after long-term operation.

The layered O3-type α-$NaFeO_2$ is of great interest due to the high theoretical capacity and the abundant, low-cost, environmentally-friendly materials.[21] The electrochemical performance of $NaFeO_2$ has been significantly improved by substitution of Fe ions by other transition metals (TMs).[22] Although various TMs have been studied as the substituted agent[22], nickel and manganese substitution is particularly attractive because the $NaNi_yFe_xMn_yO_2$ cathode takes advantage of the mature analog $LiNi_yCo_xMn_yO_2$ (NCM) technology of lithium ion batteries with Na and Fe ions replacing the Li and Co ions respectively. Kim et al. reported $NaNi_{1/3}Fe_{1/3}Mn_{1/3}O_2$ and tested it in a Na half-cell with a voltage window of 1.5V-4.0 V.[23] The cathode exhibited an average voltage of 2.75 V, a moderate capacity of 100 mAh g^{-1} for 150 cycles and a capacity of 94 mAh g^{-1} at 1C.[23] Yabuuchi et al. investigated the influence of various Fe compositions in the $NaFe_x(Ni_{0.5}Mn_{0.5})_{1-x}O_2$ system where x=0, 0.2, 0.4, 0.6, 0.8 and 1.[24] The lattice parameter *a* and *c* increased linearly with the increase of Fe composition.[24] The $NaFe_{0.4}Ni_{0.3}Mn_{0.3}O_2$ cathode showed increased electrochemical performance, delivering 130 mAh g^{-1} reversible capacity in a voltage range of 2.0V-3.8V.[24] Meanwhile, Yuan et al. also conducted studies on a similar system, $NaFe_x(Ni_{0.5}Mn_{0.5})_{1-}$

$_xO_2$ where x=0, 0.1,0.2, 0.3, 0.4 and 1.[25] The cathode with Fe=0.2 showed a reversible capacity of 125 mAh g^{-1} after 30 cycles and a high rate capacity of 86 mAh g^{-1} at 10C with the potential window of 2.0V-4.0 V.[25] Wang et al. investigated the commercial process of $NaNi_{1/3}Fe_{1/3}Mn_{1/3}O_2$ cathode materials.[26] The synthesis process was scaled up by using hydroxide co-precipitation followed with solid state reaction, and the cathode obtained a capacity of 125 mAh g^{-1} at 1C.[26] The electrochemical performance under various operating temperatures was also evaluated.[26] Moreover, a soft packed large-scale 1 Ah battery with $NaNi_{1/3}Fe_{1/3}Mn_{1/3}O_2$ as the cathode and hard carbon as the anode was prepared and maintained 0.73 Ah after 500 cycles at 1 C.[26] In addition to the electrochemical performance, the evolution of crystallographic structure was investigated. Xie et al. conducted in operando XRD on the $NaFe_{1/3}Ni_{1/3}Mn_{1/3}O_2$ cathode with the voltage window of 2.0V-4.3V and discovered a highly reversible phase transformation route, O3-P3-O3'-P3-O3 during the charge and discharge process.[27]

Recently, several groups have reported that the overall electrochemical performance of O3-type layered cathodes can be enhanced by lithium substitution.[28-31] When Li ions are introduced to the O3-type layered cathodes, Li ions are thermodynamically favored at the transition metal sites due to the similarity of its ionic radii (0.76 Å) to that of the transition metals (~ 0.5 – 0.7 Å).[29,32] Therefore, the traditional design strategy of Li-substituted layered cathodes follows the rule that the stoichiometric ratio of Na over the sum of transition metals and Li equals 1, so that the as-prepared cathodes maintain single-phased layered structures. Xu et al. investigated $NaLi_xNi_{1/3-x}Mn_{1/3+x}Co_{1/3-x}O_2$ (x = 0.07, 0.13, and 0.2) and the optimal performance was obtained by x = 0.07 with high reversible capacity of 147 mAh g^{-1} and excellent rate capability.[31] The

ex situ synchrotron X-ray diffraction (XRD) suggested that the O3 phase is maintained upon cycling, leading to good capacity retention and excellent rate performance.[31] Oh et al. reported O3-type $Na[Li_{0.05}(Ni_{0.25}Fe_{0.25}Mn_{0.5})_{0.95}]O_2$ cathodes with improved capacity retention and structural stability.[29] The XRD results suggested that the phase transition from hexagonal O3 to monoclinic P′3 was delayed in Li substituted cathode, leading to an enhanced stability.[29]

In addition to the single-phased Li-substituted O3-type layered cathodes, Lee et al. varied the Li content and obtained the layered P2/O3 intergrowth cathode that exhibited a synergistic effect to improve Na^+ diffusion for high rate performance.[33] Intergrowth electrode materials have also been studied by other groups. Chen et al. prepared stable layered P3/P2 $Na_{0.66}Co_{0.5}Mn_{0.5}O_2$ cathode materials with outstanding structural flexibility and electrochemical performance.[34] Zheng et al. demonstrated that $NaLi_{0.1}Ni_{0.35}Mn_{0.55}O_2$ exhibited O3/O'3 structure and the presence of O'3 phase, originating from Li substitution, hindered the O3-P3 phase transformation, thus improving capacity retention, such that 85% of capacity was maintained after 100 cycles.[30] Bianchini et al. prepared layered P2–O3 $Na_{2/3}Li_{0.18}Mn_{0.8}Fe_{0.2}O_2$ cathodes derived from earth abundant elements, where the electrode delivered a capacity of 125 and 105 mA h g^{-1} at C/10 and 1C rates, respectively, with a Coulombic efficiency of 95% to 99.9% over 100 cycles.[35]

Aside from the layered intergrowth cathodes, Gao et al. reported a novel design of mixed layered-tunneled P2+T phase $Na_xCo_{0.1}Mn_{0.9}O_2$ ($0.44 \leq x \leq 0.7$) with interface-rich characteristic for high performance sodium storage, whereby the tunneled T phase offers fast Na ion diffusivity and excellent structural stability and the layered P2 phase contributes to high specific capacity.[36] In addition, the P2-T interface offers additional channels and

active sites for charge storage and transfer. The specific capacity, structural stability, rate capability and Na ion diffusivity were significantly improved in the P2+T phase cathode compared with single P2 or T phase cathodes.[36]

In addition to T phase, the post-spinel $NaMn_2O_4$ cathode material with tunneled structure showed high structural stability and Na mobility for sodium ion batteries based on both computational and experimental studies.[37,38] The post-spinel $NaMn_2O_4$ was prepared under high pressure and it exhibited 94% capacity retention after 200 cycles. The stable cycling performance was attributed to the suppression of the Jahn-Teller distortion due to the high barrier of structural rearrangement of MnO_6 octahedrons.

2.4 Figures and Tables

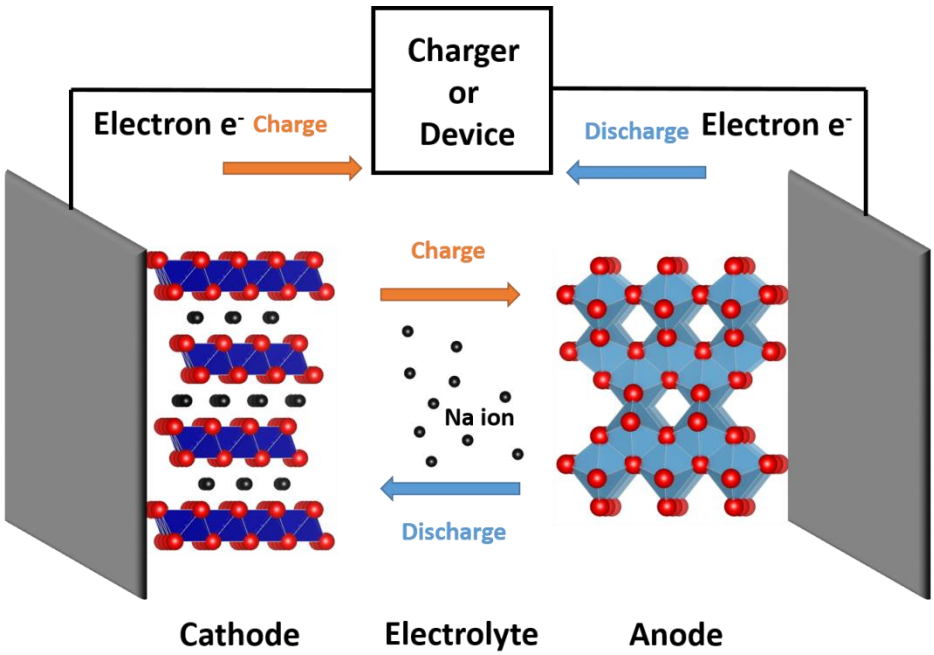

Figure 2. 1. The working principle of sodium ion batteries

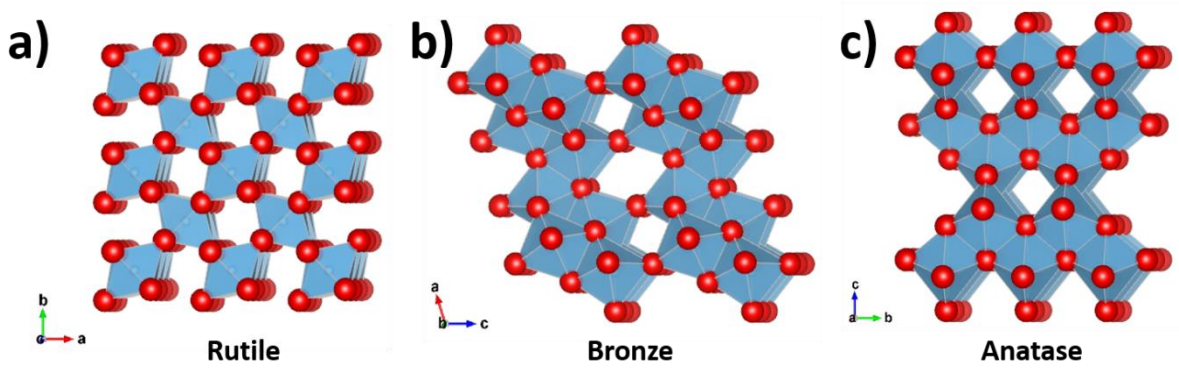

Figure 2. 2. Polymorphs of TiO2. a) Rutile, b) bronze and c) anatase.

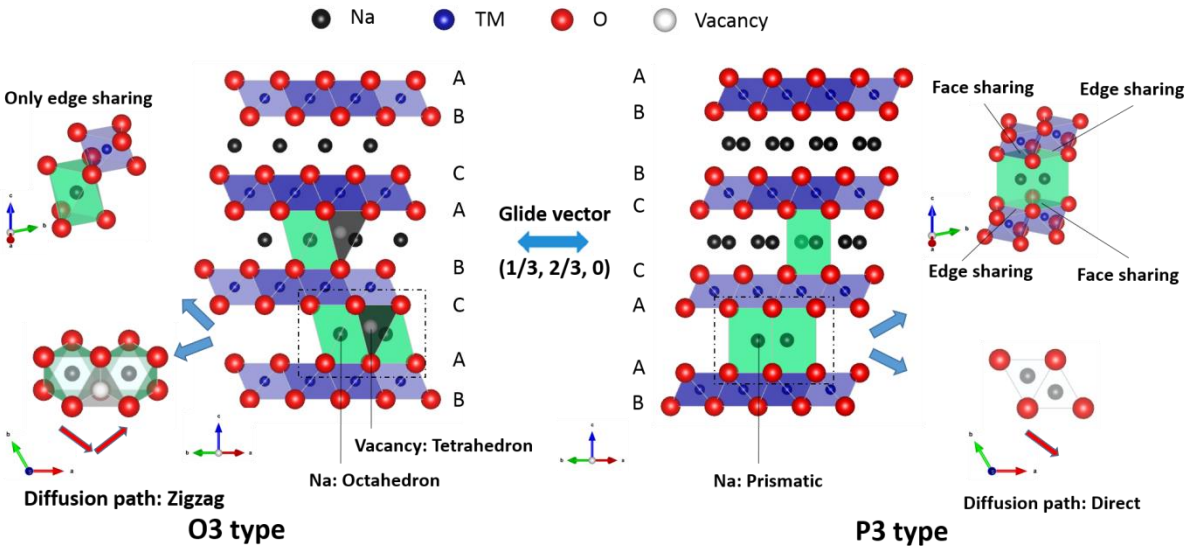

Figure 2. 3. Crystalline structure of layer O3 and P3 cathodes

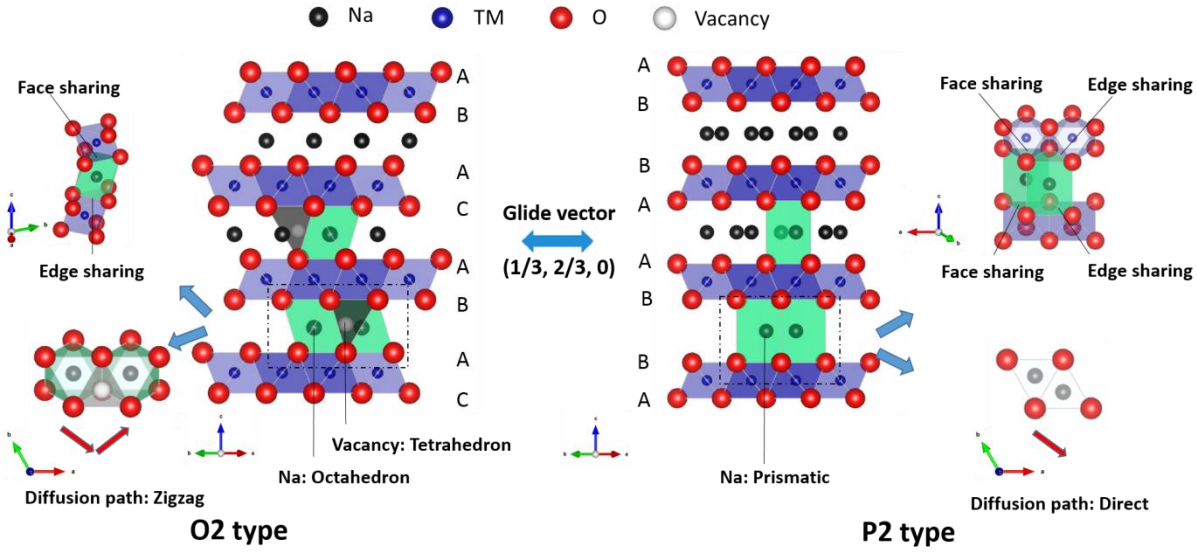

Figure 2. 4. Crystalline structure of layer O2 and P2 cathodes

Table 2. 1: Characteristics of P2 and O3 type of sodium ion batteries

	Na site	O packing	Bravais lattice	Space group	Glide vector	Phase transition
P2	Prismatic Na(2d): Face share Na(2b): edge share	AB-BA	Hexagonal	$P6_3/mmc$	(1/3, 2/3, 0)	O2
O3	Octohedral Na: edge share	AB-CA-BC	Trigonal (H)	R -3 m	(1/3, 2/3, 0)	P3

2.5 References

(1) Dachille, F.; Simons, P. Y.; Roy, R. *Am Mineral* **1968**, *53*, 1929.

(2) Yin, Z. F.; Wu, L.; Yang, H. G.; Su, Y. H. *Phys Chem Chem Phys* **2013**, *15*, 4844.

(3) Czanderna, A. W.; Rao, C. N. R.; Honig, J. M. *T Faraday Soc* **1958**, *54*, 1069.

(4) Zhang, Y. Y.; Jiang, Z. L.; Huang, J. Y.; Lim, L. Y.; Li, W. L.; Deng, J. Y.; Gong, D. G.; Tang, Y. X.; Lai, Y. K.; Chen, Z. *Rsc Adv* **2015**, *5*, 79479.

(5) Yan, X. D.; Wang, Z. H.; He, M.; Hou, Z. H.; Xia, T.; Liu, G.; Chen, X. B. *Energy Technol-Ger* **2015**, *3*, 801.

(6) Vittadini, A.; Casarin, M.; Selloni, A. *J Phys Chem C* **2009**, *113*, 18973.

(7) Su, X.; Wu, Q. L.; Zhan, X.; Wu, J.; Wei, S. Y.; Guo, Z. H. *J Mater Sci* **2012**, *47*, 2519.

(8) Xiong, H.; Slater, M. D.; Balasubramanian, M.; Johnson, C. S.; Rajh, T. *J Phys Chem Lett* **2011**, *2*, 2560.

(9) Wu, L. M.; Buchholz, D.; Bresser, D.; Chagas, L. G.; Passerini, S. *J Power Sources* **2014**, *251*, 379.

(10) Wu, L. M.; Bresser, D.; Buchholz, D.; Giffin, G. A.; Castro, C. R.; Ochel, A.; Passerini, S. *Adv Energy Mater* **2015**, *5*.

(11) Li, W.; Fukunishi, M.; Morgan, B. J.; Borkiewicz, O. J.; Chapman, K. W.; Pralong, V.; Maignan, A.; Lebedev, O. I.; Ma, J. W.; Groult, H.; Komaba, S.; Damboumet, D. *Chem Mater* **2017**, *29*, 1836.

(12) Myung, S. T.; Takahashi, N.; Komaba, S.; Yoon, C. S.; Sun, Y. K.; Amine, K.; Yashiro, H. *Adv Funct Mater* **2011**, *21*, 3231.

(13) Kim, K. T.; Ali, G.; Chung, K. Y.; Yoon, C. S.; Yashiro, H.; Sun, Y. K.; Lu, J.; Amine, K.; Myung, S. T. *Nano Lett* **2014**, *14*, 416.

(14) Huang, J. P.; Yuan, D. D.; Zhang, H. Z.; Cao, Y. L.; Li, G. R.; Yang, H. X.; Gao, X. P. *Rsc Adv* **2013**, *3*, 12593.

(15) Gu, X.; Li, L. J.; Wang, Y.; Dai, P. C.; Wang, H. B.; Zhao, X. B. *Electrochim Acta* **2016**, *211*, 77.

(16) Su, D. W.; Dou, S. X.; Wang, G. X. *Chem Mater* **2015**, *27*, 6022.

(17) Delmas, C.; Fouassier, C.; Hagenmuller, P. *Physica B & C* **1980**, *99*, 81.

(18) Yu, H. J.; Ren, Y.; Xiao, D. D.; Guo, S. H.; Zhu, Y. B.; Qian, Y. M.; Gu, L.; Zhou, H. S. *Angew Chem Int Edit* **2014**, *53*, 8963.

(19) Guo, S. H.; Sun, Y.; Yi, J.; Zhu, K.; Liu, P.; Zhu, Y. B.; Zhu, G. Z.; Chen, M. W.; Ishida, M.; Zhou, H. S. *Npg Asia Mater* **2016**, *8*.

(20) Yabuuchi, N.; Kajiyama, M.; Iwatate, J.; Nishikawa, H.; Hitomi, S.; Okuyama, R.; Usui, R.; Yamada, Y.; Komaba, S. *Nat Mater* **2012**, *11*, 512.

(21) Xiang, X. D.; Zhang, K.; Chen, J. *Adv Mater* **2015**, *27*, 5343.

(22) Yabuuchi, N.; Kubota, K.; Dahbi, M.; Komaba, S. *Chem Rev* **2014**, *114*, 11636.

(23) Kim, D.; Lee, E.; Slater, M.; Lu, W. Q.; Rood, S.; Johnson, C. S. *Electrochem Commun* **2012**, *18*, 66.

(24) Yabuuchi, N.; Yano, M.; Yoshida, H.; Kuze, S.; Komaba, S. *J Electrochem Soc* **2013**, *160*, A3131.

(25) Yuan, D. D.; Wang, Y. X.; Cao, Y. L.; Ai, X. P.; Yang, H. X. *Acs Appl Mater Inter* **2015**, *7*, 8585.

(26) Wang, H.; Liao, X. Z.; Yang, Y.; Yan, X. M.; He, Y. S.; Ma, Z. F. *J Electrochem Soc* **2016**, *163*, A565.

(27) Xie, Y. Y.; Wang, H.; Xu, G. L.; Wang, J. J.; Sheng, H. P.; Chen, Z. H.; Ren, Y.; Sun, C. J.; Wen, J. G.; Wang, J.; Miller, D. J.; Lu, J.; Amine, K.; Ma, Z. F. *Adv Energy Mater* **2016**, *6*.

(28) Zhang, S. M.; Liu, Y.; Zhang, N.; Zhao, K.; Yang, J. H.; He, S. Y. *J Power Sources* **2016**, *329*, 1.

(29) Oh, S. M.; Myung, S. T.; Hwang, J. Y.; Scrosati, B.; Amine, K.; Sun, Y. K. *Chem Mater* **2014**, *26*, 6165.

(30) Zheng, S. Y.; Zhong, G. M.; McDonald, M. J.; Gong, Z. L.; Liu, R.; Wen, W.; Yang, C.; Yang, Y. *J Mater Chem A* **2016**, *4*, 9054.

(31) Xu, J.; Liu, H. D.; Meng, Y. S. *Electrochem Commun* **2015**, *60*, 13.

(32) Shannon, R. D. *Acta Crystallogr A* **1976**, *32*, 751.

(33) Lee, E.; Lu, J.; Ren, Y.; Luo, X. Y.; Zhang, X. Y.; Wen, J. G.; Miller, D.; DeWahl, A.; Hackney, S.; Key, B.; Kim, D.; Slater, M. D.; Johnson, C. S. *Adv Energy Mater* **2014**, *4*.

(34) Chen, X. Q.; Zhou, X. L.; Hu, M.; Liang, J.; Wu, D. H.; Wei, J. P.; Zhou, Z. *J Mater Chem A* **2015**, *3*, 20708.

(35) Bianchini, M.; Gonzalo, E.; Drewett, N. E.; Ortiz-Vitoriano, N.; del Amo, J. M. L.; Bonilla, F. J.; Acebedo, B.; Rojo, T. *J Mater Chem A* **2018**, *6*, 3552.

(36) Gao, G.; Tie, D.; Ma, H.; Yu, H.; Shi, S.; Wang, B.; Xu, S.; Wang, L.; Zhao, Y. *J Mater Chem A* **2018**, *6*, 6675.

(37) Liu, X. Z.; Wang, X.; Iyo, A.; Yu, H. J.; Li, D.; Zhou, H. S. *J Mater Chem A* **2014**, *2*, 14822.

(38) Ling, C.; Mizuno, F. *Chem Mater* **2013**, *25*, 3062.

CHAPTER THREE: EXPERIMENTAL METHODS

3.1 Synthesis

3.1.1 Synthesis of TiO_2 Materials

TiO_2 nanoparticle materials are synthesized by sol-gel method. A sol-gel synthesis is a reaction of inorganic polymerization, which is composed of hydrolysis, poly-condensation and drying process.[1] The size of the product nanoscale particles can be tuned by solution composition, temperature and pH value.[2] The major advantages of sol-gel synthesis can be listed as i) product homogeneity, ii) low temperature of synthesis, iii) simple manipulation of particle size and distribution.[3]

3.1.2 Synthesis of Layered Oxide Cathodes

The basic synthesis method for the layered cathodes is solid state reaction. Generally, based on the stoichiometry of each metal in the target compound formula, the desired amount of metal oxides or metal oxalate precursors are well-mixed and well-grinded with lithium and/or sodium carbonates. Subsequently, the mixture is calcined. Note that the as-prepared cathode materials are very sensitive to the air and moisture, thus it should be stored in the glovebox immediately after the calcine process finishes. Ceder et al. plotted the phase diagram with Na_xCoO_2 as a model system[4]. It is illustrated that precise control of calcine temperature and amount of sodium played a crucial role to obtain pure phase. Otherwise, the distorted phases, for example, O'3 and P'3 were found. Generally, pure O3 type is prepared with lower temperature and higher sodium amount than the P2 counterpart.

3.2 Structural Characterization

3.2.1 X-Ray Diffraction (XRD)

XRD is a basic technique to examine the crystallographic structure, grain size and preferred orientation. A monochromatic X-ray beam with the wavelength λ hits the atomic plane at the incident angle of **θ**. As a result, the beam is reflected and only intensified at a certain angle according to Bragg's law (defined as following), leading to an identical peak intensity in the XRD pattern as the following equation:

$$n\lambda = 2d\sin\theta \quad (1)$$

Where n is integer, λ is the wavelength of incident beam, d is the d-spacing and θ is the incident angle. Since n is an integer and λ and d are constant for a given equipment and crystal structure, the Bragg law is only valid for a particular incident angel where the reflected beam interfere constructively.

3.2.2 Pair Distribution Function (PDF)

XRD characterization has been successfully used to analyze a variety of crystalline materials. However, materials with nanoscale crystallites or disordered structure usually exhibit diffusive Bragg-like peaks, which are neither as sharp nor as many as those observed in the XRD patterns of regular bulk crystalline materials.[5] Therefore, it is challenging to obtain structural information of highly disordered or nanoscale materials using standard XRD. This limitation of traditional XRD can be tackled by PDF.[5] PDF is also known as the total scattering analysis, which analyzes not only Bragg peaks but also the scattering from X-ray, electron, or neutron diffraction.[6] Synchrotron X-ray source is required for the PDF analysis to have a great signal to noise ratio. The general process of PDF analysis is briefly summarized as following: the X-ray

diffraction pattern is obtained and corrected, and then the pattern is Fourier transformed to obtain reduced G(r) function.[6] G(r) indicates the probability of two atoms separated by the distance r. The peak position, peak width and integrated intensity suggest the atom pair distance, probability distribution of the distance (disorder) and the number of adjacent atoms (coordination).[6]

3.2.3 X-ray Adsorption Spectroscopy (XAS)

X-ray absorption spectroscopy (XAS) is widely used to determine chemical environment of specific element. When a monochromatic x-ray beam hit the sample, the oscillating electric field interacts with the electron bond. The X-ray could be absorbed and then excite the electrons if the energy is equal or greater than the bonding energy of core electrons, which results in absorption edges corresponding to the shell where the core electron originally located. The specific elements with diverse chemical environment could be determined by these edges at the corresponding bonding energy.

The XAS technique applied in the battery research can be generally categorized into two parts by the energy range of the beam. The soft XAS refers to the beam with the photon energy ranging from several tens of electron volts (eV) to 2 keVs while the hard XAS ranges from a few keVs to tens of keVs.[6] Both soft and hard XAS have been widely used in battery material research, particularly in the layered cathode material to characterize transition metals (e.g. Ni, Fe, Mn). For the general characterization of transition metals, soft XAS is to probe L-edge where electrons are excited from 2p to 3d states while hard XAS is to test K-edge where electrons are excited from 1s to 4p orbitals.

3.2.3.1 Soft XAS

Soft XAS (sXAS) is used to probe chemical environments at the surface or bulk with depth sensitivities. The incident X-rays are absorbed by the sample through excitation of core-level electrons to unoccupied states above the vacuum or Fermi level.[6,7] Total electron yield (TEY) accounts for all the electrons escaping from the surface of the material, and is measured by the net current that flows into the sample to neutralize the positively charged sample by escaped electrons.[8] The probing depth of TEY mode is approximately 2-5 nm due to the mean free path of electrons in the sample, largely representing the surface environment of examined materials.[6] In addition, the mode of total fluorescence yield (TFY) is sensitive with a probe depth of several hundreds of nanometers, which makes the characterization in a bulk scale. However, TEY mode is still considered as surface technique when compared with hard XAS.

3.2.3.2 Hard XAS

Hard XAS offers the probing range from microns to millimeters.[6] There are transition and fluorescence modes in hard XAS tests. Generally, transition mode is preferred when the sample is thin and the concentration of the element is sufficient. Otherwise the fluorescence mode should be selected.[9] There are generally four regions in the hard XAS pattern: 1) pre-edge; 2) X-ray absorption near edge structure (XANES); 3) near edge x-ray absorption fine structure (NEXAFS) and 4) extended x-ray absorption fine structure (EXAFS). XANES corresponds to the region in the spectrum within ~30-50 eV near the absorption energy while EXAFS relates to the region ~20-30 eV above the absorption region.[6] The XANES region of a specific transition metal k-edge provides information to estimate the oxidation state. In addition, the coordination number and local

geometry of specific metals could be determined by XANES region. Note that the structural information provided by both general XRD and PDF is not element-specific. Therefore, XANES and EXAFS is applied to investigate the local environment of each element.

3.3 Electrochemical Characterization

3.3.1 Galvanostatic Cycling

3.3.1.1 Voltage

The voltage of a cell is related to the chemical potentials of Na in anode and cathode, which is defined as the following:

$$V_{oc} = \frac{\mu_a^+ - \mu_c^-}{nF} \quad (2)$$

Where μ_a^+ and μ_c^- are the chemical potentials of Na in the anode and cathode respectively. When the cell is fully charged, μ_a^+ is larger than μ_c^-, giving a positive voltage in the cell. Once the cell is fully discharged, μ_a^+ is equal to μ_c^-, giving a zero voltage in the cell. Note that this operation voltage should be carefully selected because of the electrochemical window of electrolyte, formed by the highest occupied molecular orbital (HOMO) and the lowest unoccupied molecular orbital (LUMO) (Figure 3.1). The passive solid electrolyte interface (SEI) forms when either μ_a^+ located above the LUMO or μ_c^- located below the LUMO, which leads to electrolyte deposition on anode and cathode respectively.

The behavior of Na intercalation and de-intercalation is governed by Gibbs phase rule and exhibited in voltage profile. The rule is defined as following:

$$F = C - P + 2 \quad (3)$$

Where F is the number of degrees of freedom, C as the number of components and P as the number of phases. In terms of intercalation mechanism in a half cell, the number of components in the system is two, which are the host cathode, and sodium ions. The voltage profile with a sloping curve indicates the one-phase region where three degrees of freedom applies, which are temperature, pressure and voltage. Whereas a plateaus in a voltage profile indicates a two-phase region where there is no freedom for voltage as temperature and pressure are fixed.

3.3.1.2 Capacity

Capacity is the amount of charge that is stored in the active materials. It is usually reported in terms of gravimetric (unit, mAh g^{-1}) or volumetric (unit, mAh cm^{-3}) specific capacity with the emphasis on different applications. The nanoscale materials with high surface area generally exhibit higher gravimetric capacity than the bulk counterpart. However, the volumetric capacity is an issue due to the low tap density. The gravimetric (C_g) and volumetric (C_v) theoretical capacity is defined as following:

$$C_g = \frac{xF}{M_W} \quad (4)$$

$$C_v = \rho C_g \quad (5)$$

Where x is the amount of Na extracted from the active material, M_W as the molecular weight of the material, ρ as the density of active materials.

One crucial parameter in terms of specific capacity is Coulombic efficiency (CE), which indicates the reversibility of redox reaction. It is defined as the ratio of charge capacity over discharge capacity in the following equation,

$$CE = \frac{C_{discharge}}{C_{charge}} \quad (6)$$

Ideally, the CE equals 1 assuming all of electrons are contributed to the sodium intercalation and de-intercalation. However, some of the electrons are consumed by other processes, resulting in irreversible reaction.

3.3.1.3 Energy Density

The energy density (ED) is the amount of energy stored in the specific material, which is defined as:

$$ED = \int VdC \quad (7)$$

Where V is the voltage platform at which capacity is output, C as the specific capacity. We know from the equation that high energy density requires both a high voltage platform and high output specific capacity, which is illustrated in voltage profile. Generally, layered cathode materials exhibits lower voltage platform and higher capacity than other cathode materials with diverse crystal structures, for example, poly-anionic cathode. Therefore, the approach to increase the voltage platform is extremely important for layered cathode materials.

3.3.1.4 Power Density

Power density is how fast the energy can be transferred with the specific material, which is tested under various current rate during charge and discharge, and then plotted by the diagram of rate capability. The current rate is usually defined as C rate. For example, the rate of C/10 means it takes 10 hours to fully discharge a cell. Generally, high rate leads to high polarization at the interface of electrode and electrolyte, which leads to the loss of capacity.

3.3.2. Galvanostatic Intermittent Titration Technique (GITT)

GITT is proposed by Weppner and Huggins and becomes one of the most applied chronoamperometry techniques. During a GITT process, a constant current is applied for a certain time and then the cell is relaxed without current to reach an open circuit condition until the voltage change is negligible. This process is repeated until the potential reaches cut-off potential. Therefore, the equilibrium potential during the galvanostatic process is obtained. Moreover, The GITT can be used to determine the diffusion coefficient of the insertion materials under the assumption of i) diffusion subject to Fick's law and ii) uniform current distribution throughout the electrode.[10]

The diffusion coefficient can be expressed as the following equation:

$$D_{Na+} = \frac{\pi}{4}\left(\frac{m_B V_M}{M_B S}\right)^2 \left(\frac{\Delta E_S}{\tau\left(dE_\tau / d\sqrt{\tau}\right)}\right)^2, \tau \ll \frac{L^2}{D_{Na+}} \quad (8)$$

where m_B, V_M, M_B, S and τ are the mass (g), molecular volume (cm^3/mol), molecular weight (g/mol), active surface area (cm^2) and current pulse time (s) of the active material. If E versus $\sqrt{\tau}$ shows a linear behavior during the current pulse (Figure 3.2a and 3.2b), the equation can be transformed into:

$$D_{Na+} = \frac{\pi}{4\tau}\left(\frac{m_B V_M}{M_B S}\right)^2 \left(\frac{\Delta E_S}{\Delta E_\tau}\right)^2, \tau \ll \frac{L^2}{D_{Na+}} \quad (9)$$

Where ΔE_S and ΔE_τ for each titration are illustrated in Figure 3.2 b) and 3.2 d).

3.3.3 Cyclic Voltammetry

Cyclic voltammetry (CV) is a powerful technique to understand the electrochemical reduction and oxidation. One of the most common uses is the linear sweep voltammetry where the cell is scanned at a constant rate of potential over time between lower and upper cut-off voltage. The anodic and cathodic peak refer to the

depletion of oxidation and reduction at the surface respectively. The potential variation between a pair of anodic and cathodic peak is the peak-to peak separation (ΔE_p). In a chemically- and electrochemically-reversible system, ΔE_p is 57 mV at 25 ^oC.[11] The deviation to 57 mV can be applied to indicate the irreversibility of the electrochemical process.

Another application of linear sweep voltammetry is to investigate the charge storage kinetics of the intercalation materials. The sweep voltammetry also provides insights in terms of diffusion and capacitive contribution of the Na storage mechanism, which can be characterized by analyzing the data under various sweep rate according to[12]

$$i = av^b \quad (10)$$

Where measured current i obeys a power law relationship with scan rate. Both a and b in the equation are adjustable parameters. A b value of 1 indicates that the charge storage is controlled by a capacitor-like kinetics, which is one of the characteristic features of capacitive contribution.[13] A b=0.5 indicates that the charge storage process is limited by diffusion[14]. In addition, the diffusion and capacitive contribution to the current response at the fixed potential can be quantitatively examined by the following equation[13]:

$$i(V) = k_1 v + k_2 v^{1/2} \quad (11)$$

where the term $k_1 v$ and $k_2 v^{1/2}$ represent the contributions from surface capacitive and diffusion controlled process, respectively. Therefore, by determining both k_1 and k_2, we

are able to quantitatively estimate the fraction of current contributed by capacitor-like process and those from the diffusion-limited process.

3.4 FIGURES AND TABLES

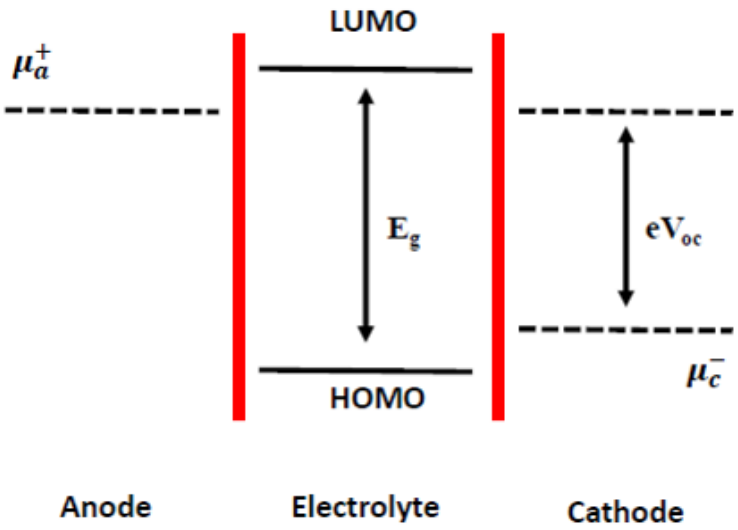

Figure 3. 1: Scheme of the electrochemical (voltage) window of the electrolyte.

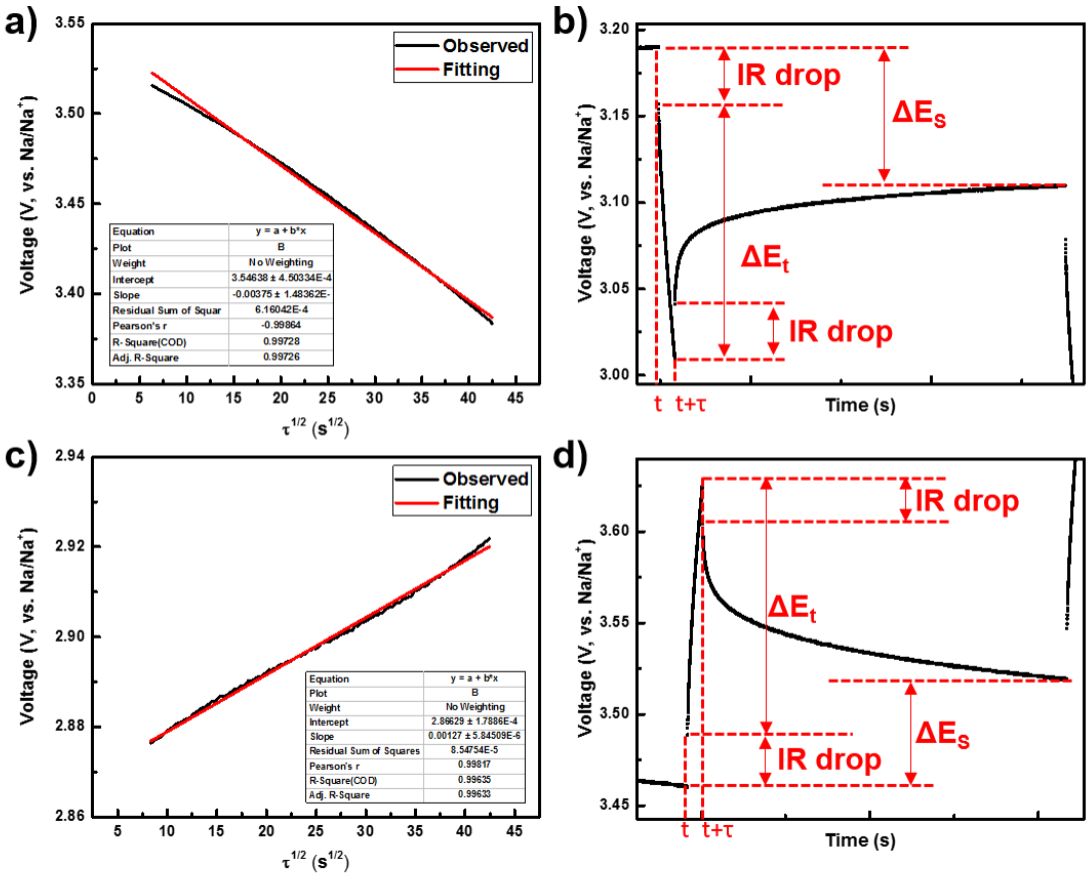

Figure 3. 2: Linear behavior of the E vs $\tau^{1/2}$ relationship in (a) discharge and (c) charge process. Schematic of GITT technique in (b) discharge and (d) charge process.

3.5 References

(1) Gupta, S. M.; Tripathi, M. *Cent. Eur. J. Chem.* **2012**, *10*, 279.

(2) Burda, C.; Chen, X. B.; Narayanan, R.; El-Sayed, M. A. *Chem. Rev.* **2005**, *105*, 1025.

(3) Ganguli, D. *B. Mater. Sci.* **1992**, *15*, 421.

(4) Lei, Y. C.; Li, X.; Liu, L.; Ceder, G. *Chem. Mater.* **2014**, *26*, 5288.

(5) Petkov, V. *Mater. Today* **2008**, *11*, 28.

(6) Lin, F.; Liu, Y. J.; Yu, X. Q.; Cheng, L.; Singer, A.; Shpyrko, O. G.; Xing, H. L. L.; Tamura, N.; Tian, C. X.; Weng, T. C.; Yang, X. Q.; Meng, Y. S.; Nordlund, D.; Yang, W. L.; Doeff, M. M. *Chem. Rev.* **2017**, *117*, 13123.

(7) Yang, W.; Devereaux, T. P. *J. Power Sources* **2018**, *389*, 188.

(8) Lin, F.; Nordlund, D.; Markus, I. M.; Weng, T. C.; Xin, H. L.; Doeff, M. M. *Energy Environ. Sci.* **2014**, *7*, 3077.

(9) Sharpe, L. R.; Heineman, W. R.; Elder, R. C. *Chem. Rev.* **1990**, *90*, 705.

(10) Weppner, W.; Huggins, R. A. *J. Electrochem. Soc.* **1977**, *124*, 1569.

(11) Elgrishi, N.; Rountree, K. J.; McCarthy, B. D.; Rountree, E. S.; Eisenhart, T. T.; Dempsey, J. L. *J. Chem. Educ.* **2018**, *95*, 197.

(12) Lindstrom, H.; Sodergren, S.; Solbrand, A.; Rensmo, H.; Hjelm, J.; Hagfeldt, A.; Lindquist, S. E. *J. Phys. Chem. B.* **1997**, *101*, 7717.

(13) Wang, J.; Polleux, J.; Lim, J.; Dunn, B. *J. Phys. Chem. C* **2007**, *111*, 14925.

(14) Bard, A. J.; Faulkner, L. R. *Electrochemical Methods: Fundamentals and Applications*; John Wiley & Sons: New York, 1980.

CHAPTER FOUR: THE IMPACT OF CRYSTALLINITY ON ANATASE TIO_2 ANODE MATERIALS

4.1 Introduction

Sodium ion batteries (SIB) are of great interest in terms of large scale energy storage system. TiO_2 is a promising anode for SIB due to the safe operation voltage, abundance and low cost. Although amorphous, single-phased, binary mixed-phased crystalline TiO_2 materials have been investigated as the anode materials for SIB, the impact of crystallinity on sodium (de)insertion into TiO_2 is underexplored. Herein, we report a systematic study of crystallinity effect on electrochemical charge storage properties of mesoporous TiO_2 nanoparticles as an anode for SIB. We have prepared amorphous (A-TiO_2), partially-crystalline (PC-TiO_2) and fully-crystalline (FC-TiO_2) anatase TiO_2 nanospheres with similar particle size ~200 nm to investigate the impact of crystallinity of anatase TiO_2 as the (de)insertion host materials for SIB. The amorphous, partially-crystalline and fully-crystalline features were confirmed in bulk, local and atomic scale by X-ray diffraction (XRD), Raman spectroscopy and transmission electron spectroscopy (TEM) respectively. The uniform particle size distribution (~200 nm) among all TiO_2 samples was confirmed by TEM. A-TiO_2 sample shows a sloping curve on both discharging and charging profile. However, PC-TiO_2 and FC-TiO_2 samples show plateaus on the 1^{st} discharging curve with a sloping curve on 1^{st} charging process, suggesting the irreversible phase transition during Na ion insertion in first activation process. The electrochemical performance in terms of rate capability and cycle life

directly related to the crystallinity, where more crystallinity leads to a higher specific capacity with the same operation condition. Cyclic voltammetry (CV) was conducted to understand the Na ion insertion process where PC-TiO_2 and FC-TiO_2 samples show one pair of reversible redox cathodic and anodic peaks while A-TiO_2 sample shows a single cathodic peak at 0.88V. It suggests the irreversible Na insertion process in A-TiO_2 sample which leads to the lower specific capacity and Coulombic efficiency than PC-TiO_2 and FC-TiO_2 samples. The charge storage mechanism was analyzed by power law that the diffusion controlled intercalation became significant with the increase of crystallinity. In addition, the Na ion diffusion coefficient was investigated by galvanostatic intermittent titration technique (GITT) where more crystallinity leads to a larger diffusion coefficient, consistent with the rate capability. Moreover, the structure of TiO_2 samples with various crystallinity was investigated by pair distribution function (PDF) to understand the Na ion diffusion behavior. The decrease of crystallinity was confirmed by the weakened amplitude and shortened feature range. The corner-shared Ti-Ti distance through Na ion diffusion pathway increased with the increase of crystallinity, leading to the expanded diffusion channels and therefore more active sites and faster diffusion. Our study investigated what the impact of crystallinity on the electrochemical performance and how it works, which will shed light on the next-generation advanced electrode design.

4.2 Experiment

4.2.1 Synthesis

A-TiO_2 samples were prepared by the sol-gel process and PC-TiO_2 and FC-TiO_2 samples were prepared by aging the A-TiO_2 sample in water at different temperature.[1] In

a typical synthesis, 0.85 mL of tetrabutyl orthotitanate (TBOT) was added to a mixture of 50 mL of 200-proof ethanol, 0.15 g of hydroxypropyl cellulose (HPC) and 300 μL of sodium chloride (0.04 M). After stirring in air for 3 hours, the precipitate was obtained by centrifuging and was washed several times by both 200-proof ethanol and de-ionized (DI) water. The product was well-dispersed in a mixture of 19 mL of DI water and 1 mL of NaF solution (1mg/10mL) by sonication. Then, the solution was stirred and heated for 30 minutes at the temperature of 50 ^{o}C, 75 ^{o}C and 100 ^{o}C for the A-TiO_2, PC-TiO_2 and FC-TiO_2 respectively. The samples were washed with 200-proof ethanol and DI water and dried.

4.2.2 Material Characterization

XRD spectroscopy was conducted by Rigaku Miniflex 600 with Cu-Kα radiation (λ = 1.5418Å), at a scan rate of 0.05 °/s in the 2θ range of 20-80°. Raman spectroscopy was obtained by a Horiba Scientific Lab RAM HR Evolution spectrometer using the 442 nm He:Cd laser with signal accumulations of three 30s scans. The incident laser power was 100 mW, and samples were viewed at a magnification of 100x. TEM characterizations were performed by FEI Titan 80-300 ST at the accelerating voltage of 200 kV. PDF was conducted by Synchrotron X-ray with the wavelength of 0.24128Å at beamline 17-BM of the Advanced Photon Source in Argonne National Laboratory. The pristine and cycled samples were carefully sealed in the Kapton tape. The data was collected by a PerkinElmer amorphous silicon detector in transition mode. The collected 2D diffraction data were integrated into 1D diffraction intensity versus 2Θ through program GSAS-II.[2] The 1D data in reciprocal space was subsequently converted to PDF profiles with program PDFgetX3.[3]

4.2.3 Electrochemical Characterization

The electrochemical performance of TiO_2 samples was evaluated in the coin-type half cells. The cells were assembled in an argon filled glovebox ($[O_2]$<0.5 ppm) using glass fiber as the separator, 1M sodium perchlorate ($NaClO_4$) in propylene carbonate (PC) as the electrolyte, metallic sodium as the counter electrode and laminated electrodes as the working electrode. The laminated electrodes are composed of 80% of TiO_2 active materials, 10% of super carbon C45 (Timcal America Inc.) and 10% of sodium carboxymethylcellulose (CMC, Dow Chemical Company). The coin cells were tested with the potential window from 0.1 to 2 V in an Arbin battery tester. Cyclic voltammograms were recorded in three-electrode cells (EL Cell, ECC-REF) with the potential window from 0.1 to 2 V at varying scan rates of 0.1 - 10 mV s^{-1}. GITT was conducted in three-electrode cells between 0.1-2 V at discharge scan rates of 10 mA g^{-1} in intervals of 30 minutes, separated by a rest period of 2 hours.

4.3 Results and Discussion

The crystalline structure of TiO_2 samples is identified by XRD shown in Figure 4.1(a). There are no pronounced fingerprint peaks in the XRD of the A-TiO_2 sample, suggesting the amorphous structure. PC-TiO_2 and FC-TiO_2 samples show broadened characteristic peaks due to the nanoscale crystallite size, which can be indexed as the anatase phase ($I4_1/amd$). The full width at half maximum (FWHM) of PC-TiO_2 sample is significantly broader than that of FC-TiO_2 sample, indicating the weakened diffraction from PC-TiO_2 sample resulted from a lower degree of crystallinity.

In addition to XRD, Raman scattering as a local probe is very sensitive to the crystallinity where the peaks become weak and broad when the sample has local lattice

imperfections.[4] The Raman spectra of TiO_2 samples are shown in Figure 4.1(b). Anatase TiO_2 has a tetragonal structure (space group $I4_1/amd$) and is comprised of two TiO_2 units per primitive cell, leading to six Raman active modes in the vibrational spectrum: three E_g modes centered around 144, 196, 639 cm^{-1} (designated at $E_{g(1)}$, $E_{g(2)}$ and $E_{g(3)}$, respectively), two B_{1g} modes centered around 397 and 519 cm^{-1} (designated at $B_{1g(1)}$, and $B_{1g(2)}$, respectively), and an A_{1g} mode at 513 cm^{-1}.[5] Due to the overlap of $B_{1g(2)}$ and A_{1g} modes the symmetry assignment of the two modes has been difficult. The broad humps in the Raman spectrum of A-TiO_2 sample suggest a highly disordered structure. In PC-TiO_2 sample, the $E_{g(1)}$ and $E_{g(3)}$ peaks of the anatase structure are observable but weak due to the decreased crystallinity. As for the FC-TiO_2 sample, the intensity of the $E_{g(1)}$ peak (148 cm^{-1}) significantly increases and the high-frequency peaks become pronounced, suggesting the fully-ordered structure. The $E_{g(1)}$ mode of FC-TiO_2 sample has a large decrease in FWHM compared with the PC-TiO_2 sample, indicating more ordered structure of FC-TiO_2 sample, consistent with previous study.[4]

The morphology and structural information of TiO_2 nanoparticle samples are further investigated by TEM at atomic scale.[6] Despite a different crystallographic structure, A-TiO_2 (Figure 4.2a), PC-TiO_2 (Figure 4.2b) and FC-TiO_2 (Figure 4.2c) samples are composed of spherical nanoparticles with similar particle size, approximately 200 nm, consistent with a previous study.[1] The degree of ordering on the atomic level of the samples are examined by selected area electron diffraction (SAED) and high resolution TEM (HRTEM). The characteristic diffusive ring (Figure 4.2d) and the lack of pronounced lattice (Figure 4.2g) suggest that the A-TiO_2 sample is amorphous. PC-TiO_2 sample shows faint and broadened diffraction rings on the SAED pattern, which

correspond to the planes of anatase structure illustrated in Figure 4.2(e). The HRTEM image of PC-TiO_2 sample exhibits (101) lattice fringes with a *d*-spacing of 3.49 Å. Both SAED and HRTEM suggest amorphous/anatase domains in the PC-TiO_2 sample. For the FC-TiO_2 sample, the SAED pattern shows well-defined and pronounced diffraction rings attributed to anatase structure, and the HRTEM image is composed of lattice fringes of anatase (101) crystal planes where the d-spacing is 3.51 Å, both of which indicate the fully-crystalline anatase structure of the FC-TiO_2 sample.

The electrochemical performance of TiO_2 samples is shown in Figure 4.3. The first-cycle voltage profiles at the rate of 20 mA g^{-1} with the potential window of 0.1V-2.0V is shown in Figure 4.3(a). The A-TiO_2 sample exhibits sloping feature on both charging and discharging curves, suggesting Na ion diffusion within the single phase. However, PC-TiO_2 and FC-TiO_2 samples have a plateau at 0.44V and 0.40V on the discharging curve respectively, suggesting the possible phase transition of the metastable sodium titanate phase further into metallic titanium, sodium superoxide and amorphous sodium titanate phase.[7] A slightly different plateau voltage was found in comparison to the reported one (0.3V), which possibly resulted from the variation in particle size and/or defect effects of the crystal structure.[8] The plateau voltage of the PC-TiO_2 sample is slightly higher than that of FC-TiO_2. The plateau voltage increases with the increase in the amorphous component, possibly because the accommodation of electronic carriers becomes increasingly difficult as periodicity is lost, which in turn generates the excess value.[8-12] The charging curves of both PC-TiO_2 and FC-TiO_2 samples are absent of plateau features, suggesting the irreversible insertion of sodium ions in the first discharging process, consistent with a previous study.[7] The first charging capacity of FC-

TiO_2 (174 mAh g^{-1}) and PC-TiO_2 (165 mAh g^{-1}) is much larger than that of A-TiO_2 (105 mAh g^{-1}),

The rate capability of the samples are evaluated and presented using the discharge capacity displayed in Figure 4.3(b) at the rate of 0.02 A g^{-1}, 0.1 A g^{-1}, and 0.5 A g^{-1}. The reversible discharge capacity at 20^{th} cycle at 0.02 A g^{-1} of A-TiO_2, PC-TiO_2 and FC-TiO_2 sample are 65 mAh g^{-1}, 116 mAh g^{-1} and 124 mAh g^{-1}. The capacity moderately drops with the increase of current rates. At the high rate of 0.5 A g^{-1}, the A-TiO_2, PC-TiO_2 and FC-TiO_2 samples deliver 26 mAh g^{-1}, 67 mAh g^{-1} and 76 mAh g^{-1}, respectively. When the current rate is ramped back to 0.02 A g^{-1} after a variety of cycling rates, the capacity of the A-TiO_2, PC-TiO_2 and FC-TiO_2 sample recovers to 59 mAh g^{-1}, 105 mAh g^{-1} and 112 mAh g^{-1}, suggesting good capacity retention and rate capability. Moreover, the cycle life performance at the rate of 100 mA g^{-1} of the samples are shown in Figure 4.3(c). The A-TiO_2, PC-TiO_2 and FC-TiO_2 samples deliver reversible capacity of 50 mAh g^{-1}, 82 mAh g^{-1} and 99 mAh g^{-1} after 100 cycles, respectively. Note that both rate capability and cycle life study shown that the FC-TiO_2 performs much better than that of the A-TiO_2 sample and the performance of PC-TiO_2 lies between the FC-TiO_2 and A-TiO_2 samples, suggesting the electrochemical performance of TiO_2 nanoparticle electrode is related to the crystallinity.

CV is conducted to understand the sodium insertion and extraction in TiO_2 samples. Figure 4.4(a) shows the CV curves of TiO_2 samples at the rate of 0.2 mV s^{-1}. Both PC-TiO_2 and FC-TiO_2 samples show a reversible redox pair where the reduction and oxidation peak located at 0.60V and 0.83V, respectively. However, there is one irreversible reduction peak on the A-TiO_2 sample located at 0.88V, suggesting the

irreversible sodium insertion into the A-TiO_2 host structure where the sodium ions are trapped, which possibly leads to a lower specific capacity and Coulombic efficiency than the PC-TiO_2 and FC-TiO_2 samples. The voltammetry with various scan rates of 0.1, 0.2, 0.5, 1 and 2 mV s^{-1} of A-TiO_2, PC-TiO_2 and FC-TiO_2 sample are shown in Figure 4.4(b), 4.4(c) and 4.4(d), respectively to investigate the charge storage mechanism, which can be analyzed according to the power law relationship:

$$i = av^b \quad (1)$$

Where i is the observed current, v as the scan rate, a and b as the adjustable parameters.[13] The *b*-value of 0.5 and 1 represent that the charge storage is limited by capacitive contribution and diffusion controlled intercalation, respectively.[13,14] The *b*-values vs. voltage plots of TiO_2 samples during the discharging process are shown in Figure 4.5(a). The *b*-values of the A-TiO_2 sample are larger than that of the PC-TiO_2 and FC-TiO_2 samples throughout the whole discharging process, suggesting the amorphous component in the structure leads to the increase of capacitive contribution. As for the PC-TiO_2 and FC-TiO_2 samples, the *b*-values are higher than 0.9 when discharge is above 0.8V, suggesting a significantly capacitive-controlled process.[7] When discharged below 0.8V, the *b*-values of both PC-TiO_2 and FC-TiO_2 samples continuously decreased, suggesting a process of complex diffusion-controlled diffusion and phase transitions.[7]

In addition, the charge storage can be quantitatively determined by the following equation:

$$i(V) = k_1 v + k_2 v^{1/2} \quad (2)$$

where $k_1 v$ and $k_2 v^{1/2}$ represent the capacitive contribution and diffusion-controlled intercalation respectively.[13,14] Therefore, we are able to quantitatively investigate the charge storage mechanism by the fraction of $k_1 v$ and $k_2 v^{1/2}$. Figure 4.5(b), 4.5(c) and 4.5(d) demonstrate the CV curve of the A-TiO_2, PC-TiO_2 and FC-TiO_2 samples at the slow scan rate of 0.1 mV s^{-1}, respectively, where the shaded area indicates the capacitive contribution to the charge storage. The capacitive contribution of A-TiO_2, PC-TiO_2 and FC-TiO_2 samples are 57%, 51% and 45% respectively, gradually decreasing with the decrease of disordered component in the structure. More than half of charge storage comes from the capacitive contribution in the A-TiO_2 sample. However, the contribution from the diffusion controlled intercalation overpasses the capacitive contribution in FC-TiO_2 sample.

We conducted GITT of TiO_2 samples (Figure 4.6a) to quantitatively investigate the diffusion-controlled intercalation by calculating the sodium diffusion. The log plot of the sodium diffusivity in the insertion process as a function of voltage is shown in Figure 4.6(b). As for both the FC-TiO_2 and PC-TiO_2 samples, the diffusivity below 1.2V is plotted due to the significant IR drop of the GITT curve (Figure 4.6a). The diffusivity of both the FC-TiO_2 and PC-TiO_2 samples gradually decrease with the sodium insertion process from 1.2V to 0.4V, possibly because the sodium insertion leads to the sluggish formation of a metastable sodium titanate phase and subsequent solid state sodium diffusion.[7] When cycled below 0.4V, the diffusivity of both the FC-TiO_2 and PC-TiO_2 samples slightly increase due to the formation of the amorphous sodium titanate phase[7] where the disordered structure with defects could offer active sites and spatial channels for the sodium diffusion.[15] In terms of an A-TiO_2 sample, the diffusivity gradually

decreases from 0.88V to 0.28V, possibly due to the limited supply of active sites with the continuous insertion of sodium ions. It is worth noting that the diffusivity of the FC-TiO_2 sample is the highest during most of the voltage window and the A-TiO_2 sample had the lowest, suggesting the highest and lowest specific capacity in the rate capability of FC-TiO_2 and A-TiO_2 samples respectively (Figure 4.3).

In addition to electrochemical characterizations, *ex situ* PDF is conducted to investigate the structural evolution of the TiO_2 samples. Though XRD has been successfully applied to investigate the crystalline structure for decades, it is limited to the nanoscale crystallite and highly-disordered structure.[16] The PDF technique, however, reveals the short and intermediate range order of the materials regardless of the degree of disorder, offering a new opportunity to investigate disordered and partially ordered materials.[17] The PDF data of TiO_2 samples at the pristine state with a long spectrum of radial distance (1Å-60 Å) was shown in Figure 4.7 (a). All curves show the featured amplitudes at low real-space region, suggesting the short-term ordering for all of TiO_2 samples. However, the amplitude ramps down at approximately 8 Å, 35 Å and 48 Å for A-TiO_2, PC-TiO_2 and FC-TiO_2 samples, respectively, suggesting the long-term ordering with the increase of crystallinity. Moreover, the stronger amplitude of the FC-TiO_2 sample also indicates better-defined crystallinity than that of the PC-TiO_2 and FC-TiO_2 samples in short-term ordering range. The local atomic feature is emphasized in Figure 4.7 (b) at the low real-space region (1.5 Å-9.0 Å), where 1st discharged and 1st charged samples are plotted together to understand the structural evolution during cycling. After the 1st cycle, all of TiO_2 samples show a weakened amplitude, suggesting decreased ordering after Na ion (de)insertion process. The peaks in the pristine TiO_2 samples at 1.93

Å, 2.51 Å, 3.01 Å and 3.75 Å can be indexed to the Ti-O, O-O, Ti-Ti in edge-sharing and Ti-Ti in corner-sharing TiO_6 octahedral distances respectively.[18,19] At the 1st discharged state where Na ions are inserted, the distinct O-O peak becomes a faint shoulder (2.41 Å) that can be assigned to the newly-formed Na-O distance,[18] suggesting the declined O-O ordering. It is possibly due to the phase transition from anatase TiO_2 (space group: $I4_1/amd$) to layered-like Na_xTiO_2 (space group: R-3m) where cationic mixing and vacancies were created after Na insertion.[18] The O-O ordering does not recover after Na ions are extracted (1st charged state), suggesting the irreversible Na ion insertion process. The unit cell of anatase TiO_2 crystal structure is shown in Figure 4.7 (c) where black and red balls indicate Ti atoms and O atoms respectively. It has been reported that active sites for Na ion insertion are the empty tetrahedral and octahedral sites along zigzag TiO_6 channel.[20,21] The channel for sodium diffusion is directly related to the Ti-Ti distance in corner-sharing TiO_6 octahedra (highlighted in purple in Figure 4.7b and 4.7c).The Ti-Ti distance of A-TiO_2, PC-TiO_2 and FC-TiO_2 samples are 3.75 Å, 3.83 Å and 3.85 Å, which increases with the increase of crystallinity. Because the large Ti-Ti distance offers more active sites and expanded channels for Na ion diffusion, FC-TiO_2 sample with the largest Ti-Ti distance exhibits the highest specific capacity and enhanced rate capability among all of other samples. Though the Ti-Ti distance decreased for all of TiO_2 samples after Na ion insertion and/or extraction process due to the irreversible phase transition, FC-TiO_2 sample shows a strong amplitude and well-defined peak, suggesting the great Ti-Ti ordering which possibly contributes to the great cycle life performance.

4.4 Conclusions

Amorphous, partially-crystalline and fully crystalline TiO_2 nanoparticles are successfully prepared by a sol-gel process with different heat treatments. The uniform particle size distribution of all TiO_2 samples was confirmed by TEM images. The unique amorphous and crystalline features were confirmed in bulk, local and atomic scale by XRD, Raman spectroscopy and TEM respectively. The increase of crystallinity leads to better electrochemical performance in terms of Coulombic efficiency, rate capability and cycle life. CV suggests the irreversible Na insertion process of an A-TiO_2 sample which possibly resulted in the lower specific capacity and Coulombic efficiency than that of the PC-TiO_2 and FC-TiO_2 samples. The Na ion diffusion coefficient is evaluated by GITT where more crystallinity leads to a larger diffusion coefficient that is consistent with the rate capability where the crystalline TiO_2 samples have a higher specific capacity than an amorphous one. In addition to electrochemical evaluation, PDF, which is sensitive to both amorphous and crystalline materials, is conducted to understand the structural evolution related to the performance. The corner-shared Ti-Ti distance through Na ion diffusion pathway increases with the increase of crystallinity, leading to expanded diffusion channels and therefore more active sites and faster diffusion. Though the Ti-Ti distance decreases for all of TiO_2 samples after the Na ion insertion and/or extraction process due to the irreversible phase transition, a FC-TiO_2 sample shows a strong amplitude and well-defined peak, suggesting a great Ti-Ti ordering which possibly contributes to the great rate capability and cycle life performance.

4.5 Figures and Tables

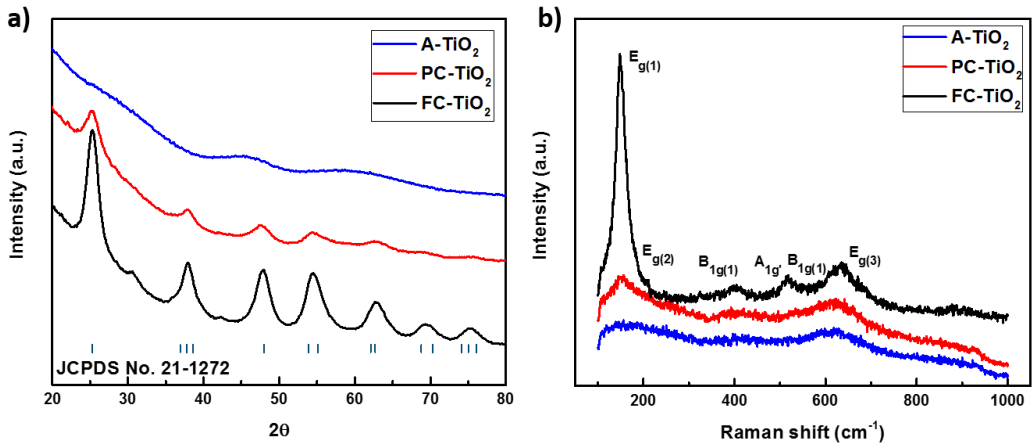

Figure 4. 1: a) XRD and b) Raman of pristine TiO_2 samples

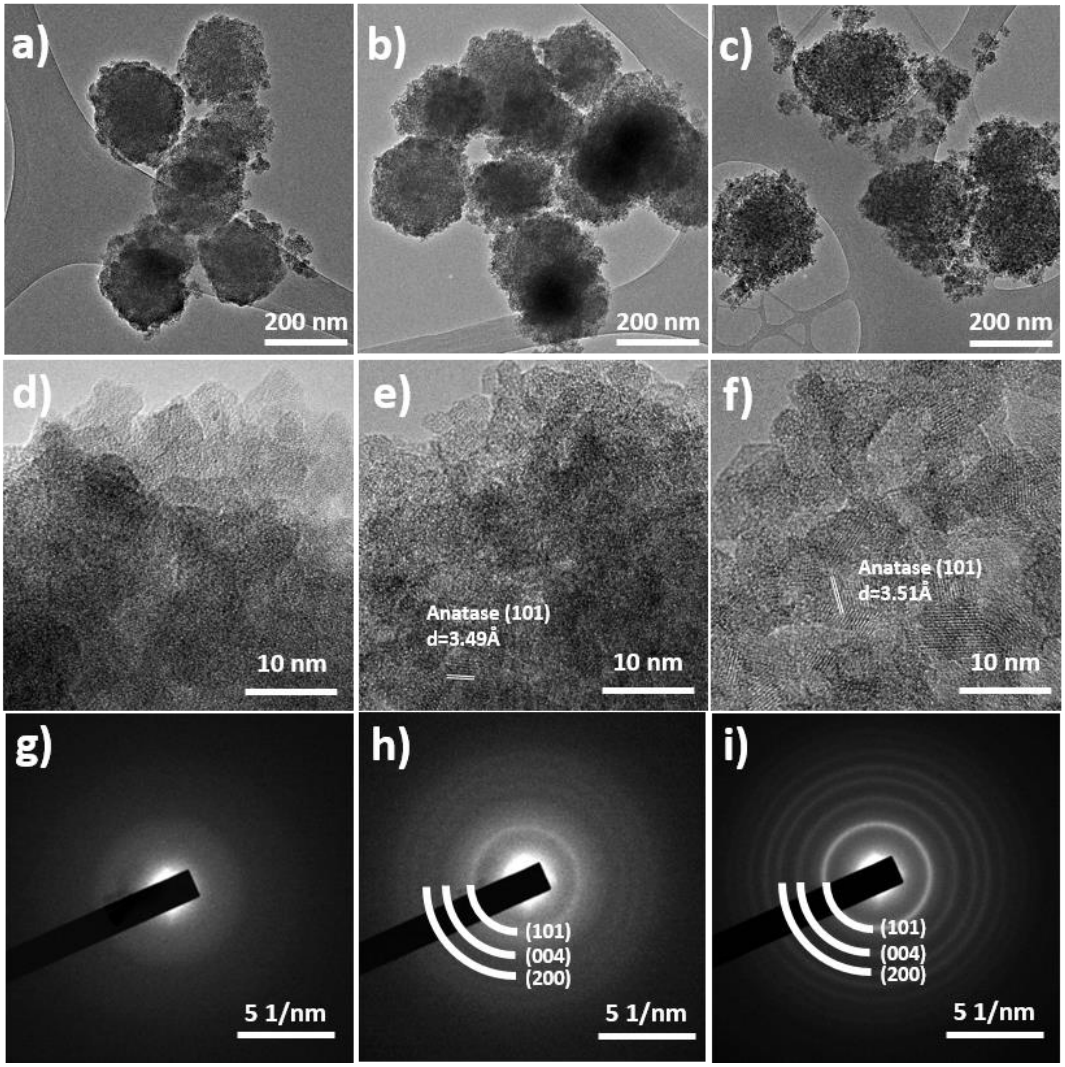

Figure 4. 2: TEM images of a) A-TiO_2, b) PC-TiO_2 and c) FC-TiO_2. HRTEM images of d) A-TiO_2, e) PC-TiO_2 and f) FC-TiO_2. SAED patterns of g) A-TiO_2, h) PC-TiO_2 and i) FC-TiO_2.

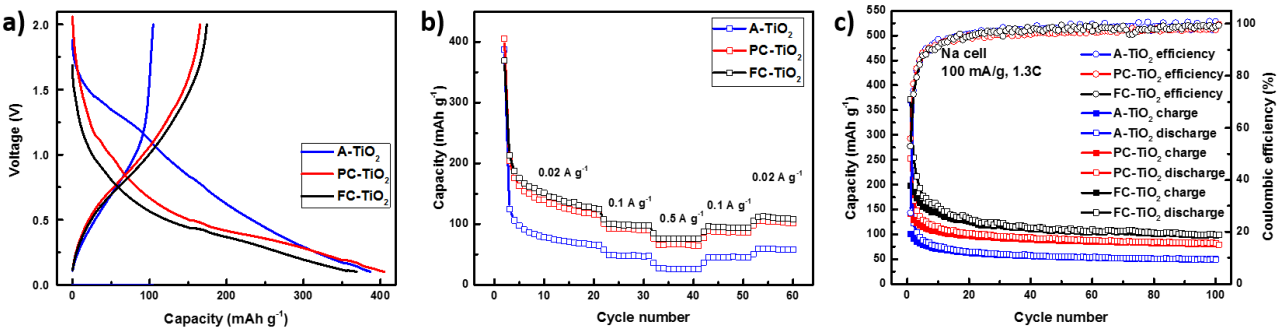

Figure 4. 3: a) voltage profile, b) rate capability and c) cycle life performance of TiO_2 samples. The voltage window for all of galvanic testing is 0.1-2.0V.

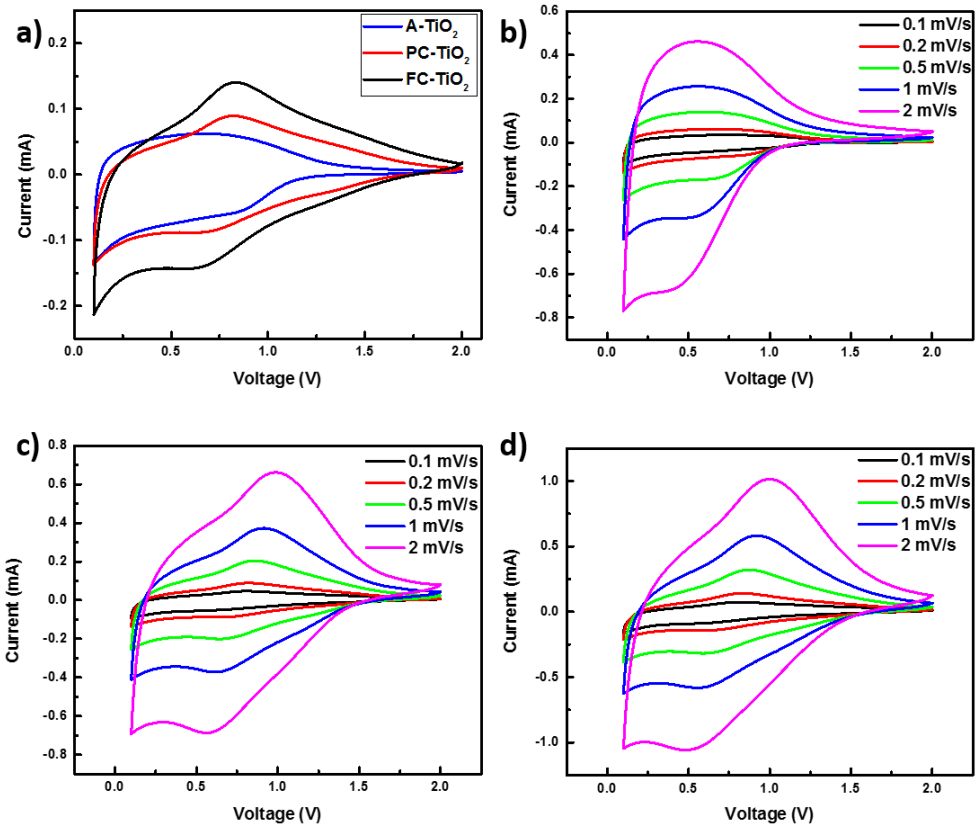

Figure 4. 4: a) CV curves of TiO_2 samples at the scan rate of 0.2 mV s^{-1} with the voltage window of 0.1-2.0V. The CV curves of b) A-TiO_2, c) PC-TiO_2 and d) FC-TiO_2 at various scan rates.

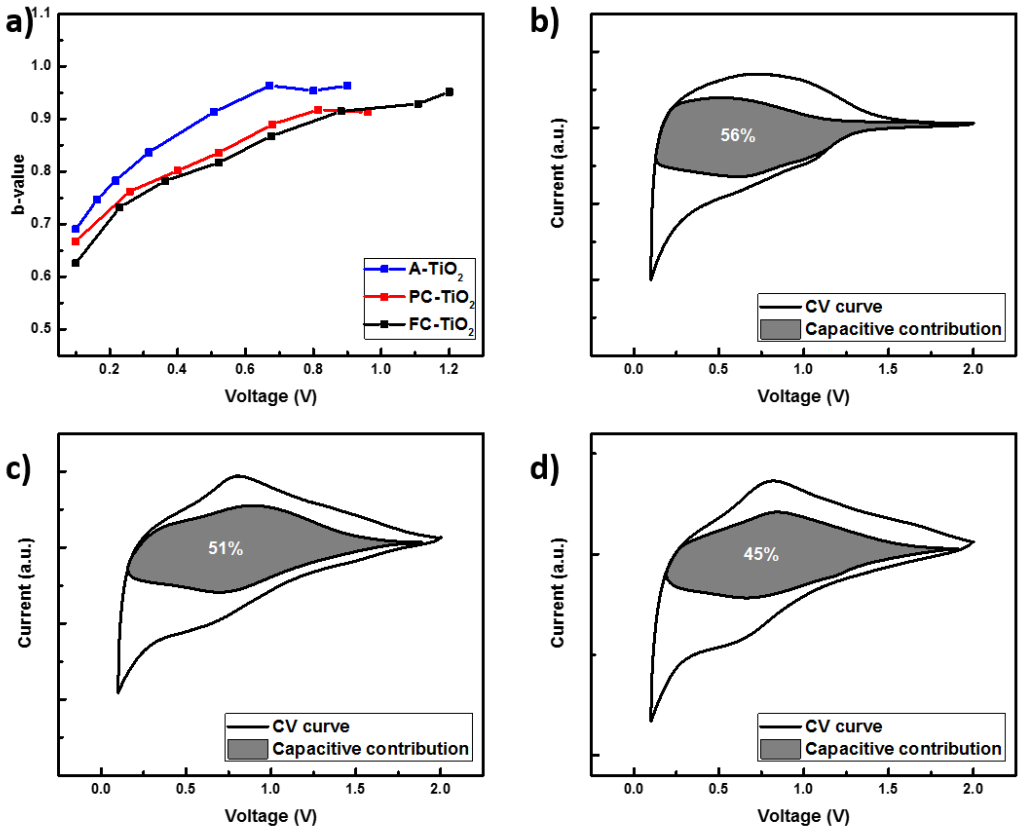

Figure 4. 5: a) The b-value of TiO_2 samples. The charge storage mechanism of b) A-TiO_2, c) PC-TiO_2 and d) FC-TiO_2 samples at the rate of 0.2 mV s^{-1}.

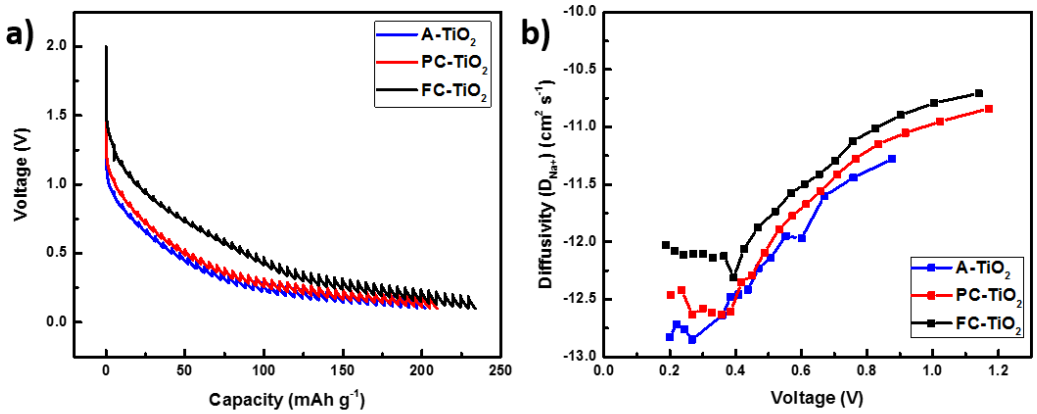

Figure 4. 6: a) GITT profile and b) Diffusivity vs. state of charge of TiO_2 samples

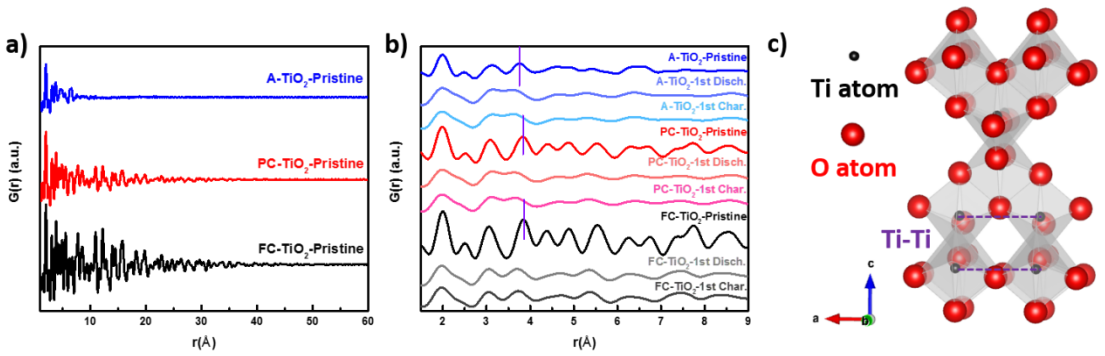

Figure 4. 7: a) The PDF curves of pristine, 1st charged and 1st discharged TiO_2 samples with the atomic distance ranged from 1to 60 Å. b)The pristine, 1st charged and 1st discharged PDF curves of TiO_2 samples with the enlarged range of 1 Å -9 Å. The purple line illustrated the corner-shared Ti-Ti distance. c) The scheme of crystal structure of anatase TiO_2. The purple dashed line represents Ti-Ti in corner-sharing TiO_6 octahedral distances.

4.6 References

(1) Li, N.; Zhang, Q.; Joo, J. B.; Lu, Z. D.; Dahl, M.; Gan, Y.; Yin, Y. D. *Nanoscale* **2016**, *8*, 9113.

(2) Toby, B. H.; Von Dreele, R. B. *J. Appl. Crystallogr.* **2013**, *46*, 544.

(3) Juhas, P.; Davis, T.; Farrow, C. L.; Billinge, S. J. L. *J. Appl. Crystallogr.* **2013**, *46*, 560.

(4) Zhang, W. F.; He, Y. L.; Zhang, M. S.; Yin, Z.; Chen, Q. *J. Phys. D Appl. Phys.* **2000**, *33*, 912.

(5) Smith, K. A.; Savva, A. I.; Deng, C. J.; Wharry, J. P.; Hwang, S.; Su, D.; Wang, Y. Q.; Gong, J.; Xu, T.; Buttf, D. P.; Xiong, H. *J. Mater. Chem. A* **2017**, *5*, 11815.

(6) Stach, E. A. *Mater. Today* **2008**, *11*, 50.

(7) Wu, L. M.; Bresser, D.; Buchholz, D.; Giffin, G. A.; Castro, C. R.; Ochel, A.; Passerini, S. *Adv. Energy Mater.* **2015**, *5*.

(8) Liu, C. F.; Neale, Z. G.; Cao, G. Z. *Mater. Today* **2016**, *19*, 109.

(9) Zhu, C. B.; Mu, X. K.; Popovic, J.; Weichert, K.; van Aken, P. A.; Yu, Y.; Maier, J. *Nano Lett* **2014**, *14*, 5342.

(10) Uchaker, E.; Zheng, Y. Z.; Li, S.; Candelaria, S. L.; Hu, S.; Cao, G. Z. *J. Mater. Chem. A* **2014**, *2*, 18208.

(11) Fang, Y. J.; Xiao, L. F.; Qian, J. F.; Ai, X. P.; Yang, H. X.; Cao, Y. L. *Nano Lett* **2014**, *14*, 3539.

(12) Liu, Y. L.; Xu, Y. H.; Han, X. G.; Pellegrinelli, C.; Zhu, Y. J.; Zhu, H. L.; Wan, J. Y.; Chung, A. C.; Vaaland, O.; Wang, C. S.; Hu, L. B. *Nano Lett* **2012**, *12*, 5664.

(13) Wang, J.; Polleux, J.; Lim, J.; Dunn, B. *J. Phys. Chem. C* **2007**, *111*, 14925.

(14) Deng, C. J.; Lau, M. L.; Barkholtz, H. M.; Xu, H. P.; Parrish, R.; Xu, M.; Xu, T.; Liu, Y. Z.; Wang, H.; Connell, J. G.; Smith, K. A.; Xiong, H. *Nanoscale* **2017**, *9*, 10757.

(15) Xiong, H.; Slater, M. D.; Balasubramanian, M.; Johnson, C. S.; Rajh, T. *J. Phys. Chem. Lett.* **2011**, *2*, 2560.

(16) Petkov, V. *Mater. Today* **2008**, *11*, 28.

(17) Billinge, S. J. L.; Kanatzidis, M. G. *Chem. Commun.* **2004**, 749.

(18) Li, W.; Fukunishi, M.; Morgan, B. J.; Borkiewicz, O. J.; Chapman, K. W.; Pralong, V.; Maignan, A.; Lebedev, O. I.; Ma, J. W.; Groult, H.; Komaba, S.; Damboumet, D. *Chem. Mater.* **2017**, *29*, 1836.

(19) Fernandez-Garcia, M.; Belver, C.; Hanson, J. C.; Wang, X.; Rodriguez, J. A. *J. Am. Chem. Soc.* **2007**, *129*, 13604.

(20) Dawson, J. A.; Robertson, J. *J. Phys. Chem. C* **2016**, *120*, 22910.

(21) Madian, M.; Eychmuller, A.; Giebeler, L. *Batteries-Basel* **2018**, *4*.

CHAPTER FIVE: THE ORIGIN OF IRREVERSIBILITY IN LAYERED CATHODE MATERIALS

5.1 Introduction

Although the electrochemical performance and the structural evolution of $NaNi_yFe_xMn_yO_2$ cathodes have been widely studied, the practical application has been limited by the large irreversibility during the cycling process. The irreversibility reduces the energy density of the cell,[1] complicates the battery management system (BMS),[2] and leads to a low round-trip efficiency.[3] To the best of our knowledge, there is little systematic study on the irreversibility of cathode materials in sodium ion batteries. To this end, we prepared a series of $Na_{1.05}Ni_yFe_xMn_yO_2$ (NaNFM) to study the irreversibility in various cation compositions and different voltage windows. The molar ratio of Na ions over TM ions is set to 1.05 because it has better electrochemical performance than that of 0.95 and 1.1.[4] The molar ratio of Na and transition metal (TM) ions is confirmed by inductively coupled plasma (ICP). The crystalline structure of NaNFM cathodes is investigated by X-ray diffraction (XRD) and Rietveld refinement where the O3-type layered α-$NaFeO_2$ structure (space group: R-3m) is obtained. The irreversibility became increasingly pronounced with the increase of either Fe composition or the upper cutoff potential. The *Ex situ* X-ray adsorption near edge spectroscopy (XANES) and extended X-ray adsorption fine structure (EXAFS) were conducted to understand the evolution of TM valence and bonding structure, respectively. This study unveils the fundamental origin of the irreversibility of layered cathode materials in sodium ion batteries, which

promotes the search for next-generation cathode materials with enhanced energy density and round-trip efficiency.

5.2 Experimental

5.2.1 Synthesis

The nominal $Na_{1.05}Ni_{1/3}Fe_{1/3}Mn_{1/3}O_2$ (NFM-Fe1/3), $Na_{1.05}Ni_{0.25}Fe_{0.5}Mn_{0.25}O_2$ (NFM-Fe0.5) and $Na_{1.05}Ni_{0.1}Fe_{0.8}Mn_{0.1}O_2$ (NFM-Fe0.8) cathodes were synthesized by solid state reaction.[5] For each cathode, an aqueous solution with the desired stoichiometric amount of nickel sulfate, iron sulfate and manganese sulfate was added into a solution of sodium oxalate under stirring. The co-precipitation solution was continuously stirred for 3 hours at 70°C in air. The product was filtered, washed and dried. The dried precursor powder and sodium carbonate were thoroughly mixed with a mole ratio of 2:1.05 respectively. The mixed powder was pressed as the pellets and calcined at 850 °C for 12 hours in air.

5.2.2 Material Characterization

The metal compositions in each cathode were examined by ICP (iCAP 6000 Radial, Thermo Fisher Scientific Inc.). The morphology of the samples was observed by scanning electron microscopy (SEM, Sirion 200, FEI Company). The crystallographic characteristics of the pristine materials were determined by XRD (Rigaku Miniflex 600) with filtered Cu Kα radiation (λ = 1.5418Å) from 5° to 120° with a step of 0.01° and scan rate of 0.8 °/min. The patterns were analyzed by General Structure Analysis System (GSAS) package. The cycled laminated electrodes tested under X-ray absorption spectroscopy (XAS) were carefully sealed in Kapton tape to avoid contact with air. XAS was conducted in Advanced Photon Sources, Argonne National Lab at beamline 12-BM.

XANES data was collected in fluorescent mode and analyzed by Athena program using the IFEFFIT package[6]. The reference spectra of Ni, Fe and Mn foil was collected simultaneously with each sample for energy calibration and data alignment. The normalized extended EXAFS spectra was converted from energy to wave vector k and then weighted by k^3.

5.2.3 Electrochemistry

All laminated electrodes were prepared by mixing 80% active materials, 10% super carbon C45 (Timcal America Inc.) and 10% poly(vinylidene fluoride) (PVDF), and then the slurry was printed on an aluminum current collector. The electrodes were punched into discs with a loading density of ~2.7mg cm^{-2}. The half-cells were prepared with cathode electrodes, glass fiber separators (Celgard) and sodium counter electrode with the electrolyte of 1M $NaPF_6$ in propylene carbonate (PC). The coin cells were cycled on an Arbin battery tester with the potential window of 2.0V-4.0V and 2.0V-4.3V.

5.3 Results and Discussions

The ICP analysis confirms the metal composition of NFM-Fe1/3, NFM-Fe0.5 and NFM-Fe0.8 to be $Na_{1.048}Ni_{0.346}Fe_{0.330}Mn_{0.324}O_2$, $Na_{1.064}Ni_{0.259}Fe_{0.498}Mn_{0.243}O_2$ and $Na_{1.070}Ni_{0.113}Fe_{0.791}Mn_{0.096}O_2$, which are consistent with the expected stoichiometry within acceptable error. The SEM was conducted to observe the morphologies of the cathode samples in Figure 5.1. All of the samples exhibit the mixture of micro-scale particles and flakes with evenly-distributed sizes. The powder XRD patterns of NFM-Fe1/3, NFM-Fe0.5 and NFM-Fe0.8 are shown in Figure 5.2(a), Figure 5.2(b) and Figure 5.2(c) respectively. All of the patterns can be indexed to the space group R -3 m with the α-$NaFeO_2$ structure. Rietveld refinement is conducted to acquire information on the unit

cells which is summarized in Table 5.1. The R_b and R_{wp} factors for all of the refinement are reasonably small, suggesting the O3-type layered structure is the appropriate model and the output parameters of the refinement are reliable. The lattice constants *a* and *c* (Figure 5.3), and the unit cell volume (Figure 5.3) increases with the increase of Fe composition, suggesting the formation of a solid solution of Ni and Mn substituted α-$NaFeO_2$, consistent with previous studies.[7,8] The *c/a* ratio is an important parameter to determine the degree of ordering of the layered structure as well as the amount of TMs in the inter-slab structure.[9] As the Fe composition increases, the *c/a* ratio decreases, demonstrating the Fe ions can introduce disordering in the layered structure.

The cycle life with the rate of 12 mA g^{-1} and rate capability of NFM-Fe1/3, NFM-Fe0.5 and NFM-Fe0.8 samples are evaluated with the potential window of 2.0V-4.0V and 2.0V-4.3V in Figure 5.4. Fe1/3-2-4, Fe05-2-4 and Fe08-2-4 represent the cathode samples cycled with a potential window of 2.0V-4.0V while Fe1/3-2-4.3, Fe05-2-4.3 and Fe08-2-4.3 represent the cathode samples cycled with the potential window of 2.0V-4.3V. Basically, both cycle life and rate capability can be improved by applying either a low upper cutoff potential window (2.0V-4.0V) or less Fe composition in the structure (NFM-Fe1/3). With the same transition metal composition, high upper cutoff potential window (2.0V-4.3V) offers higher specific capacity during the first several activation cycles. However, the irreversible capacity quickly fades and eventually delivers a lower capacity than the low upper cutoff potential window (2.0V-4.0V). With the same potential window, both cycle life and rate capability of NFM-Fe1/3 offers slightly higher capacity than that of NFM-Fe05, and significantly higher capacity than that of NFM-Fe08.

The 1st cycle voltage profiles of NFM-Fe1/3, NFM-Fe0.5 and NFM-Fe0.8 are plotted in Figure 5.5(a), 5.5(b) and 5.5(c), respectively, to investigate the Na ion (de)insertion process. The cathodes are cycled at a current rate of 0.05C (12 mA g^{-1}) with two potential windows of 2.0V-4.0V and 2.0V-4.3V, separately. Each charge curve cycled between 2.0V-4.3V has two plateaus, one at the low voltage (<3.5V) and the other at the high voltage (>4.0V), which corresponds to the phase transition from the O3 to P3 phase and the P3 to O3' phase respectively.[9,10] The sloping profile between two plateaus results from the solid-solution reaction within P3 phase. The plateau above 4.0V of NFM-Fe1/3 and NFM-Fe0.5 is much longer than that of NFM-Fe0.8. However, the Fe-rich NFM-Fe0.8 sample shows a particularly long plateau at ~3.3V, consistent with the voltage profile of α-$NaFeO_2$ cathode.[11] The 1st charge capacity between 2.0-4.3V of NFM-Fe1/3, NFM-Fe0.5 and NFM-Fe0.8 are 226.06 mAh g^{-1}, 221.76 mAh g^{-1} and 181.77 mAh g^{-1} respectively, suggesting more Ni composition can provide a higher specific capacity due to the two-electron compensation of the Ni^{2+}/N^{4+} redox pair. As for the discharge curves, the NFM-Fe1/3 and NFM-Fe0.5 demonstrate the reversible plateau at 3.84V and 3.64V, respectively. However, the curve of the NFM-Fe0.8 sample does not show a reversible plateau at high voltage, even in the 1st discharge, suggesting an irreversible P3 to O3' phase transition. The 1st discharge capacity between 2.0-4.3V of NFM-Fe1/3, NFM-Fe0.5 and NFM-Fe0.8 are 226.06 mAh g^{-1}, 221.76 mAh g^{-1} and 181.77 mAh g^{-1} respectively. The decreasing capacity with increasing Fe content is consistent with the charge capacity, where samples with a higher Ni content (and lower Fe content) will produce a higher capacity.

As for the cathodes cycled between 2.0V-4.0V, there is no plateau observed at high voltage, indicating the phase transition from P3 to O3' phase is prevented. Three cathodes offer similar 1st charge capacity, but the discharge capacity varies and follows the previous observation that the cathode with more Ni composition delivers more capacity. Interestingly, the discharge capacity of NFM-Fe0.8 sample cycled between 2V-4V is larger than that between 2.0V-4.3V, suggesting that the high cutoff voltage will significantly influence the electrochemical performance in the iron rich NFM cathode.

The dQ/dV plots with the voltage window 2.0V-4.3V of the first five cycles are shown in Figure 5.6(a), 5.6(b) and 5.6(c) to examine the plateau characteristics of NFM-Fe1/3 and NFM-Fe0.5 and NFM-Fe0.8 curves respectively. There are two reversible redox pairs for NFM-Fe1/3 and NFM-Fe0.5 samples but only one for the NFM-Fe0.8 sample. The oxidation peak above 4.0V of the NFM-Fe1/3 sample is located at the same voltage (4.12V) from 1st to 5th cycle. However, the high-voltage oxidation peak of the NFM-Fe0.5 sample becomes faint and significantly shifts from 4.13V to 3.90V within the first five cycles. As for the NFM-Fe0.8 sample, the peak disappears after the 1st cycle and there is no redox couple above 4.0V. All of the above results demonstrates that the voltage of P3-O3' phase transition will shift and then disappear with the increase of Fe composition in the structure, indicating the reversibility of the phase transition will be significantly influenced by the increase of Fe composition. After the first cycle, the oxidation peak at low voltage regions of NFM-Fe1/3 and NFM-Fe0.5 samples are consistently located at 2.85V and 2.90V, respectively. As for the NFM-Fe0.8 sample, the oxidation and reduction peak continuously shifted to higher and lower voltage, respectively, resulting in a significant irreversibility at the low potential region. However,

the oxidation and reduction peak below 3.5 V does not shift after the 1st cycle for all cathodes cycled between 2.0V-4.0V (Figure 5.7, supporting information), suggesting the improved reversibility and stability with the lower cutoff voltage window.

Considering the voltage profiles in Figure 5.5, all of the cathode materials cycled between 2.0 V-4.0 V have a smaller irreversibility of that cycled between 2.0 V-4.3V, possibly because the reduced polarization in the 2.0 V-4.0 V potential window causes a smaller overpotential.[12] Moreover, the irreversibility gradually becomes larger with the increase of Fe composition, potentially related to the change of the intrinsic electrochemical properties.

To understand the origin of irreversibility, *ex situ* XAS is conducted to investigate the local chemical and structural environment of transition metals at various states of charge (SOC) such as SOC_0%, SOC_33.3%, SOC_66.7%, SOC_100%. All of samples are activated by 5 pre-cycles to reach the stable structure. The sixth-cycle voltage profile with selected *ex situ* SOC of Fe1/3-2-4.3, Fe1/3-2-4 and Fe08-2-4 are shown in Figure 3. Fe1/3-2-4.3 and Fe1/3-2-4 are selected to explore the irreversibility in different potential windows. In addition, Fe1/3-2-4 and Fe08-2-4 are used to study the irreversibility in different TM compositions.

XANES K-edge spectra of Mn (Figure 5.9 (a), 5.9 (b), 5.9 (c)), Ni (Figure 5.9 (d), 5.9 (e), 5.9 (f)) and Fe (Figure 5.9 (g), 5.9 (h), 5.9 (i)) ions of Fe1/3-2-4.3 (Figure 5.9 (a), 5.9 (d), 5.9 (g)) Fe1/3-2-4 (Figure 5.9 (b), 5.9 (e), 5.9 (h)) and Fe08-2-4 (Figure 5.9 (c), 5.9 (f), 5.9 (i)) sample are shown in Figure 5.9. The onset adsorption is attributed to the symmetry-allowed transitions from the 1s electron to excited vacant bound.[13] The pre-edge adsorption corresponds to the electric dipole-forbidden transitions from the 1s

electron to an unoccupied 3d orbital.[14,15] The first strong adsorption is related to the shake-down process from the ligand-to-metal charge transfer (LMCT).[16,17] The primary adsorption is corresponding to the electric dipole-allowed transition from 1s to a 4p orbitals.[9,18]

Because Mn K-edge position of pristine NFM-Fe1/3 and NFM-Fe08 samples is close to that of the standard MnO_2 instead of $LiMn_2O_4$, the valence of Mn ions in both samples are tetravalent. Within each single Fe1/3-2-4.3, Fe1/3-2-4 and Fe08-2-4 sample, the shape of Mn K-edge spectra changes due to the evolution of the local environment.[8,19] The edge position of *ex situ* Mn K-edge spectra does not clearly shift to the high or low energy region during the charge or discharge process, indicating the electrochemically-inactive feature of Mn^{4+} ions. Moreover, the valence of Mn ions can be determined by the intensity of the pre-edge.[20] The negligible change of the pre-edge intensity of *ex situ* Mn K-edge spectra confirms that tetravalent Mn ions are constant during the Na (de)insertion.

In terms of Ni K-edge spectra, the pristine NFM-Fe1/3 and NFM-Fe08 samples closely resemble the standard NiO sample, indicating the existence of Ni^{2+} ions. However, the oxidation state of Ni ions in NFM-Fe1/3 is slightly higher than that in NFM-Fe08, possibly because more Na composition in the NFM-Fe08 sample (ICP results) creates more oxygen vacancies (Table 5.1) that slightly reduce the oxidation state of Ni ions. The precise shift of the Ni K-edge spectra can be quantitatively interpreted by the energy of first inflection point ($E_{0,Ni}$).[17,21] The SOC vs. $E_{0,Ni}$ plots of Fe1/3-2-4.3, Fe1/3-2-4 and Fe08-2-4 are shown in Figure 5.10 (a), 5.10 (b) and 5.10 (c) respectively. In the NFM- Fe1/3-2-4 sample, the $E_{0,Ni}$ value gradually increases and ramps back during

the charge and discharge process, suggesting the oxidation and reduction of Ni ions respectively. Both $E_{0,Ni}$ values of SOC_0% are slightly smaller than that of the pristine sample, indicating the reversible process after 5 cycles. Moreover, the $E_{0,Ni}$ value of the charge and discharge step at each SOC is similar with each other, implying that the irreversibility resulting from the Ni redox couple in Fe1/3-2-4 sample is negligible. As for the Fe1/3-2-4.3 sample, the $E_{0,Ni}$ of both SOC_0% curves reduced back to the pristine value, which manifests good reversibility of the Ni redox couple. During the charge process from SOC_0% (2.0V) to SOC_66.7% (3.7V), the $E_{0,Ni}$ linearly shifted to a higher value from 8342.56 eV to 8344.96 eV, suggesting the gradual oxidation of Ni ions. As the cell was continuously charged to SOC_100% (4.3V), the $E_{0,Ni}$ value slightly increased to 8345.11 eV, suggesting the subtle oxidation of Ni ions at high potential region. Xie et al. performs *ex situ* XANES analysis on Ni K-edge of $NaNi_{1/3}Fe_{1/3}Mn_{1/3}O_2$ sample and concludes that Ni^{2+}/Ni^{3+} redox couple is active below 4.0V while Ni^{3+}/Ni^{4+} redox couple is active between 4.0V and 4.3V.[22] Therefore, in our case, the pronounced oxidation of Ni ions from SOC_0% to SOC_66.7% and the slight oxidation from SOC_66.7% to SOC_100% can be related to Ni^{2+}/Ni^{3+} and Ni^{3+}/Ni^{4+} redox couple respectively. While during the discharge process from SOC_100% (4.3V) to SOC_66.7% (3.3V), the Ni ions were largely “relaxed” and reduced where the $E_{0,Ni}$ from 8345.11 eV to 8344.42 eV. There is a 0.69 eV gap between the $E_{0,Ni}$ value at SOC_66.7% of the charge and discharge process. As the discharge process continued, the $E_{0,Ni}$ value at SOC_33.3% and SOC_0% almost overlapped with the corresponding steps in the charge process, suggesting good reversibility of Ni redox couple at low operation potential. The irreversibility in terms of the Ni redox couple occurs at a high potential due to the slight

oxidation and relatively large reduction. Note that there is a large overpotential when the cell was discharged from 4.3V to 3.3V. However, the overpotential becomes negligible when discharged from 4.0V in Fe1/3-2-4 and no significant irreversibility in terms of Ni redox couple is observed. Therefore, the irreversibility of Fe1/3-2-4.3 at the high potential window can be attributed to the overpotential.[20,21] In terms of the Fe08-2-4 sample, the oxidation state of Ni ions gradually increases from SOC_0% to SOC_66.7% but barely increase from SOC_66.7% to SOC_100% during the charge process. However, the Ni oxidation state hardly decreases from SOC_100% to SOC_33.3% during the discharge process. Therefore, there is a gap between the $E_{0,Ni}$ value of charge and discharge at SOC_33.3%, which leads to a large irreversibility in low operation potential in terms of Ni oxidation state. This irreversibility continues to the SOC_0% state. Since there is no pronounced irreversibility in the Fe1/3-2-4 sample (Figure 5.10 (b)) as well as both the Fe08-2-4 and Fe1/3-2-4 samples are cycled with the same potential window, the irreversibility in the Fe08-2-4 sample is possibly a result of the increase in Fe composition that converts the intrinsic electrochemical properties of the cathode.[23,24] Note the oxidation state of Ni ions does not return to the pristine state but keeps increasing with cycles. Therefore, the Fe08-2-4 sample shows limited irreversible electrochemical performance in terms of cycle life and rate capability (Figure 5.4).

The shape and edge position of pristine NFM-Fe1/3 and NFM-Fe08 XANES spectra strongly resemble the standard Fe_2O_3 spectra, suggesting that trivalent Fe ions are present. It has been widely reported that the oxidation state of Fe ions can be determined by the energy of the first inflection point ($E_{0,Fe}$) of the XANES Fe K-edge spectra.[10,25] The SOC vs. $E_{0,Fe}$ plots from derived XANES Fe K-edge spectra are shown in Figure

5.10 (d), 5.10 (e) and 5.10 (f) respectively. The $E_{0, Fe}$ value of all three samples are slightly higher than that of pristine ones, possibly due to the Fe ions being irreversibly oxidized during the activation process. The Fe ions are reversibly oxidized and reduced between the state of SOC_66.7% and SOC_100% for all three samples due to the Fe^{3+}/Fe^{4+} redox couple, which contributes to the specific capacity to the total electrochemical performance based on the compensation mechanism. However, the oxidation state of Fe ions only slightly changed between SOC_0% and SOC_66.7%, implying that the Fe^{3+}/Fe^{4+} is electrochemically active at high voltage region.[26,27]

Interestingly, the oxidation state of Fe ions in all three samples does not show pronounced irreversibility during the oxidation and reduction process. In addition, the oxidation state of Mn ions very slightly changed in each sample. Therefore, the irreversibility resulting from the change of oxidation state of TMs only applies to the Ni ions. The irreversibility corresponding to Ni valence can be concluded as 1) large overpotential leads to the irreversibility at a high potential region when the same sample is cycled at higher upper cutoff potential; 2) the increased Fe composition in the cathode results in the irreversibility at the low potential region that is possibly due to the intrinsic electrochemical properties.

We conduct *ex situ* EXAFS to examine the local structural evolution with different operation potential windows and TM composition. The Fourier transform magnitudes of Mn (Figure 5.11 (a), 5.11 (b), 5.11 (c)), Ni (Figure 5.11 (d), 5.11 (e), 5.11 (f)) and Fe (Figure 5.11 (g), 5.11 (h), 5.11 (i)) ions of Fe1/3-2-4.3 (Figure 5.11 (a), 5.11 (d), 5.11 (g)) Fe1/3-2-4 (Figure 5.11 (b), 5.11 (e), 5.11 (h)) and Fe08-2-4 (Figure 5.11 (c), 5.11 (f), 5.11 (i)) sample are shown in Figure 5.11. The first intense peak at low radial

distance is related to the TM-O coordination shell and the second one is TM-TM shell. The quantitative fitting of all *ex situ* EXAFS spectra were conducted (Table 5.2-5.4) and the plots of SOC vs. TM-O radial distance are shown in Figure 5.12, where a) to i) correspond to the a) to i) in Figure 5.11, respectively. The pristine Mn-O distance in NFM-Fe1/3 and NFM-Fe08 sample is 1.89 Å. Shiraishi et al. reported the radial distance of Mn^{4+}-O in the octahedral coordination to be 1.88 Å,[4] and the theoretical distance of Mn^{4+}-O calculated from the ionic radii is 1.91 Å.[28] Thus we claim that the Mn ions in all of pristine samples are tetravalent with octahedral coordination, consistent with the XANES results in Figure 5.10 (a), 5.10 (b) and 5.10 (c). The Mn-O distance at various SOC barely changed due to the change of local environment where Na ions are inserted and/or extracted.

The pristine Ni-O distance of NFM-Fe1/3 sample is 2.06 Å, which is smaller than that of the NFM-Fe08 sample, at 2.08 Å. The larger Ni-O distance in the NFM-Fe08 sample leads to the expansion of the unit cell (Table 1) and the slight reduction of Ni valence (Figure 5.10 (d), 5.10 (e) and 5.10 (f)). Abraham et al. reported the Ni^{2+}-O and Ni^{4+}-O distance in octahedral coordination to be 2.07 Å and 1.90 Å, respectively.[29] Therefore, the oxidation state of Ni ions can be confirmed to be divalent. Moreover, the Ni-O distance of the Fe1/3-2-4.3, Fe1/3-2-4 and Fe08-2-4 samples at SOC_100% are 1.92 Å, 1.94 Å and 1.92 Å respectively, all of which are close to the Ni^{4+}-O distance of 1.90 Å, suggesting the activation of the Ni^{2+}/Ni^{4+} redox couple. The Ni-O distance of the Fe1/3-2-4.3, Fe1/3-2-4 and Fe08-2-4 samples decrease during the charging process due to the oxidation of Ni ions (Figure 5.10 (d), 5.10 (e) and 5.10 (f)) and the shrinkage of the *a*-axis as Na ions were extracted.[30] During the discharging process, the Ni-O distance in

both NFM-Fe1/3 samples reversibly ramped back to the SOC_0% position without significant irreversibility in terms of the evolution of the Ni-O distance. Note that there is a pronounced irreversibility in terms of the Ni oxidation state of the Fe1/3-2-4.3 sample at a high potential window. However, this irreversibility is *not* specifically related to the structural evolution of Ni-O distance, possibly because it stemmed from the large overpotential.[28] As for the discharging process of the Fe08-2-4 sample, the Ni-O distance irreversibly ramped back at SOC_33.3% and SOC_0%, resulting in the irreversibility at the low voltage region. Moreover, Ni-O distance at SOC_0% state did not return to the pristine value but continuously shortened during cycles, suggesting limited rate capability and cycle life performance (Figure 5.4). The irreversibility of the Fe08-2-4 sample at the low potential region results from both the Ni oxidation state and the Ni-O distance, possibly because it stemmed from the intrinsic electrochemical properties.[31]

The Fe-O distance in pristine NFM-Fe1/3 and NFM-Fe08 samples are both 2.02 Å. After the charging process, the Fe-O distance in Fe1/3-2-4.3, Fe1/3-2-4 and Fe08-2-4 at the SOC_100% state decreased to 1.97 Å, 1.98 Å and 1.96 Å respectively. Yabuuchi et al. investigated the Fe^{3+}/Fe^{4+} redox couple in the layered $Na_x(Fe_{0.5}Mn_{0.5})O_2$ cathode and observed the Fe-O distance in pristine and fully charged state are 2.00 Å and 1.90 Å respectively.[31] Then the Fe^{3+}/Fe^{4+} redox couple is confirmed by Mossbauer spectroscopy.[22] In terms of our samples, the shrinkage of Fe-O distance can be interpreted as the partial oxidation of Fe^{3+} ions to Fe^{4+} ions. During the discharging process, the Fe-O distance for all of samples reversibly returned to the state of SOC_0% which is close to the pristine position. No pronounced irreversibility in terms of Fe-O

distance was observed in all of samples, suggesting the great structural reversibility of Fe-O distance, consistent with the evolution of Fe oxidation state.

5.4 Conclusion

We prepared NFM-Fe1/3, NFM-Fe05 and NFM-Fe08 to study the irreversibility in various cation compositions and different operation voltage windows. The molar ratio of Na ions over transition metal (TM) ions is designed to be 1.05 because it provides better electrochemical performance than 0.95 and 1.1.[32] The composition of $Na_{1.05}Ni_yFe_xMn_yO_2$ cathodes is confirmed by ICP. SEM images of all $Na_{1.05}Ni_yFe_xMn_yO_2$ cathodes show the micro-scale particles and flakes with the similar particle size, which makes the possible irreversibility resulted from the overpotential caused by various morphology and particles size negligible. The crystalline structure of $Na_{1.05}Ni_yFe_xMn_yO_2$ cathodes is investigated by XRD and Rietveld refinement where the O3-type layered α-$NaFeO_2$ structure (space group: R-3m) is obtained. The lattice parameters *a, c* and volume of the unit cell linearly increase with the increase of Fe composition, suggesting the formation of a solid solution of Ni and Mn substituted α-$NaFeO_2$. The electrochemical performance of $Na_{1.05}Ni_yFe_xMn_yO_2$ cathodes was evaluated within the potential windows of 2.0-4.0V and 2.0-4.3V. The irreversibility became pronounced and the electrochemical performance became limited with the increase of either Fe composition or the upper cutoff potential. *Ex situ* XANES is conducted to understand the TM valence evolution. It reveals that Ni and Fe^{3+}/Fe^{4+} redox couple contributes to most of the specific capacity. The irreversibility resulted from TM valence is mainly attributed to Ni redox couple. The Fe1/3-2-4 exhibits negligible irreversibility, however, Fe1/3-2-4.3 shows pronounced irreversibility at the high potential region, possibly due to the large

overpotential. Moreover, the Fe08-2-4 shows a large irreversibility at low potential region, possibly resulting from the intrinsic electrochemical propertiesof the material. We also performed the EXAFS to investigate the structural evolution, particularly TM-O radial distance. It confirms that the specific capacity of Fe1/3-2-4, Fe1/3-2-4.3 and Fe08-2-4 mostly corresponds to the Ni^{2+}/Ni^{4+} and Fe^{3+}/Fe^{4+} redox couple. Ni-O distance mainly contributes to the irreversibility as well. Though the Fe1/3-2-4.3 show irreversibility in terms of Ni oxidation state, there is no structural irreversibility related to the Ni-O distance on Fe1/3-2-4.3 sample. The Fe08-2-4 sample has large irreversibility of the Ni-O distance at the low potential region, consistent with the irreversibility of Ni oxidation state. This study explores the origin of irreversibility in layered cathode materials of sodium ion batteries. It offers a great opportunity to increase the energy density as well as round-trip efficiency of next-generation layered cathode materials.

5.5 Figures and Tables

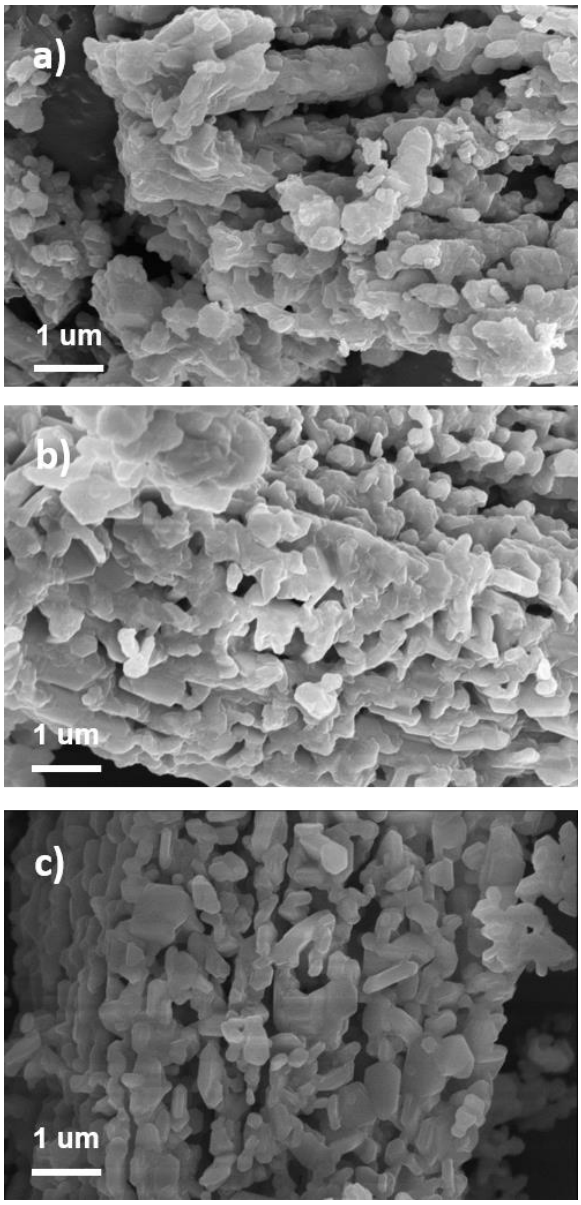

Figure 5. 1: Scanning electron microscopy (SEM) images of a) NFM-Fe1/3, b) NFM-Fe0.5 and c) NFM-Fe0.8

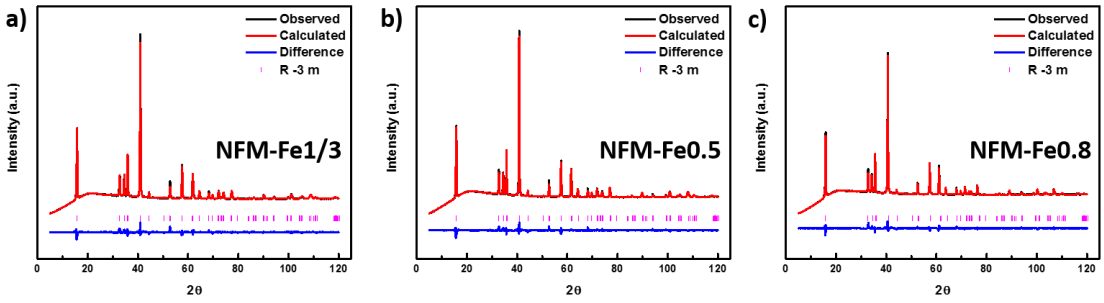

Figure 5. 2: The powder XRD patterns of a) NFM-Fe1/3, b) NFM-Fe0.5 and c) NFM-Fe0.8 sample.

Table 5. 1: The Detailed Results of XRD Rietveld Refinement of NaNFM Cathodes

Sample name	**NFM-Fe1/3**				
Space group	R -3 m				
R_{wp}=0.0181		a=2.969(7) Å			
R_b=0.0103		b=2.969(7) Å			
χ^2=11.69		c=16.054(3) Å			
Atom	Wyckoff	X	Y	Z	Occupancy
Na	3b	0	0	0	1
TM	3a	0	0	0.5	1
O	6c	0	0	0.238(4)	1

Sample name	**NFM-Fe05**				
Space group	R -3 m				
R_{wp}=0.0150		a=2.985(7) Å			
R_b=0.0083		b=2.985(7) Å			
χ^2=8.510		c=16.064(2) Å			
Atom	Wyckoff	X	Y	Z	Occupancy
Na	3b	0	0	0	1
TM	3a	0	0	0.5	1
O	6c	0	0	0.237(4)	0.921(9)

Sample name	**NFM-Fe08**				
Space group	R -3 m				
R_{wp}=0.0141		a=3.010(0) Å			
R_b=0.0076		b=3.010(0) Å			
χ^2=7.943		c=16.079(4) Å			
Atom	Wyckoff	X	Y	Z	Occupancy
Na	3b	0	0	0	1
TM	3a	0	0	0.5	1
O	6c	0	0	0.237(0)	0.923(4)

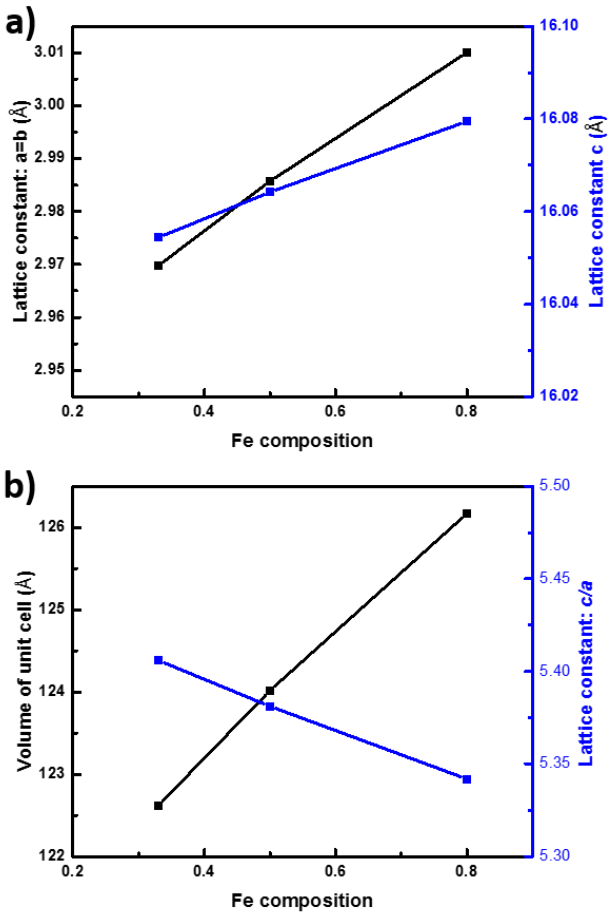

Figure 5. 3: a) lattice constants and b) volume of unit cell and *c/a* ration vs. Fe composition

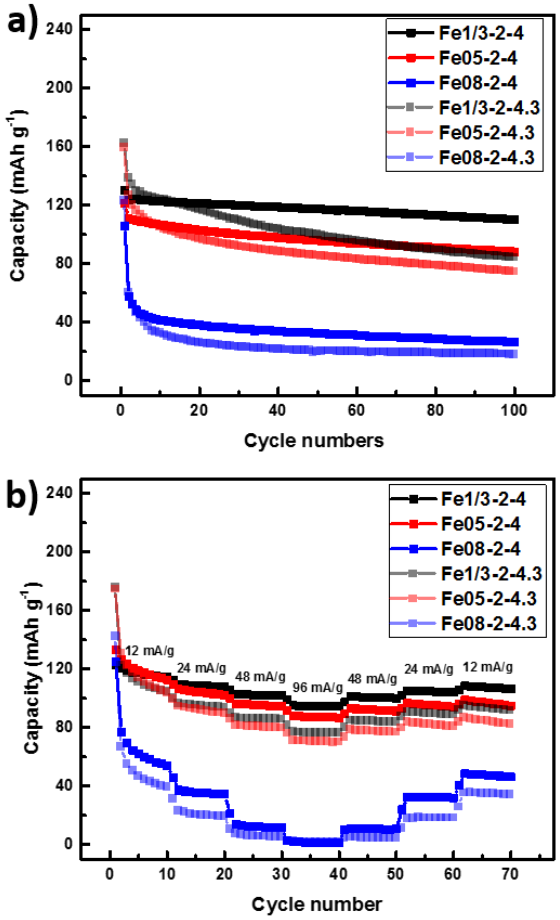

Figure 5. 4: cycle life and b) rate capability of NFM-Fe1/3, NFM-Fe0.5 and NFM-Fe0.8 samples with the potential window of 2.0V-4.0V and 2.0V-4.3V

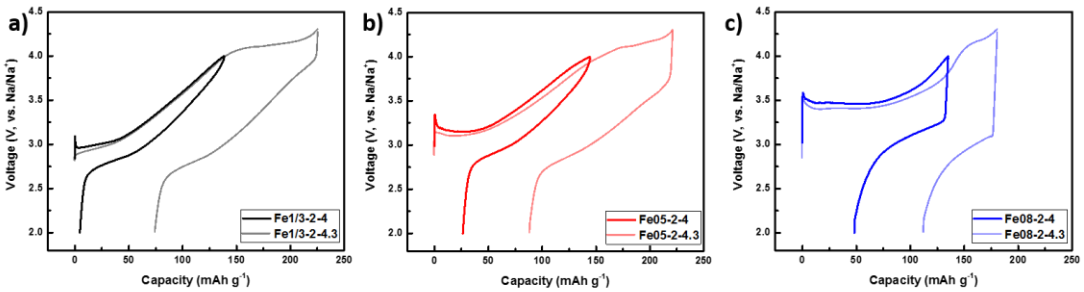

Figure 5. 5: 1st-cycle voltage profile of a) NFM-Fe1/3, b) NFM-Fe0.5 and c) NFM-Fe0.8 with the potential window between 2.0V-4.0V and 2.0V-4.3V

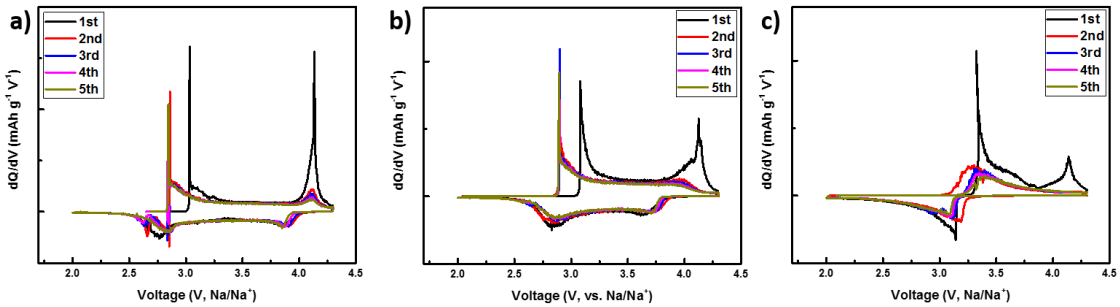

Figure 5. 6: The initial 5-cycle dQ/dV plot of (a) NFM-Fe1/3, (b) NFM-Fe0.5 and (c) NFM-Fe0.8 with the potential window of 2.0V-4.3V.

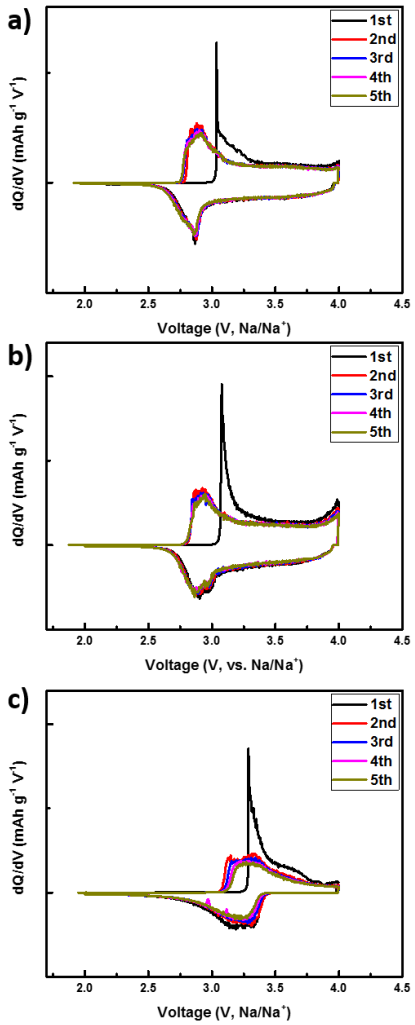

Figure 5. 7: The initial 5-cycle dQ/dV plot of (a) NFM-Fe1/3, (b) NFM-Fe0.5 and (c) NFM-Fe0.8 with the potential window of 2.0V-4.0V.

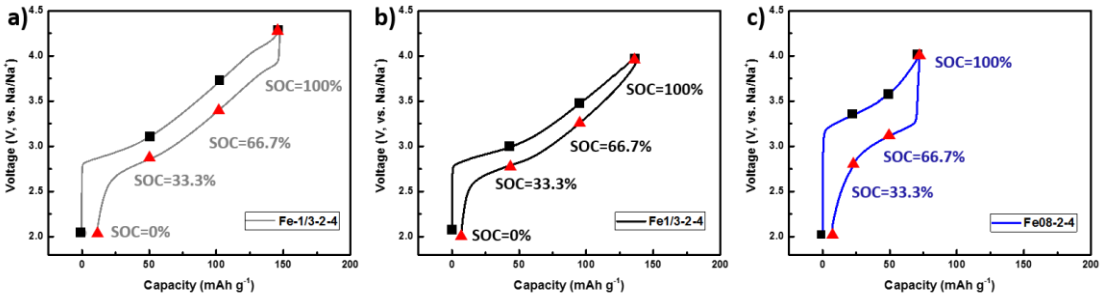

Figure 5. 8: The 6th cycle voltage profile of (a) Fe1/3-2-4.3, (b) Fe1/3-2-4 and (c) Fe08-2-4 with the selected SOC state during cycling. The black squares and red triangles represent the SOC states during charge and discharge process respectively.

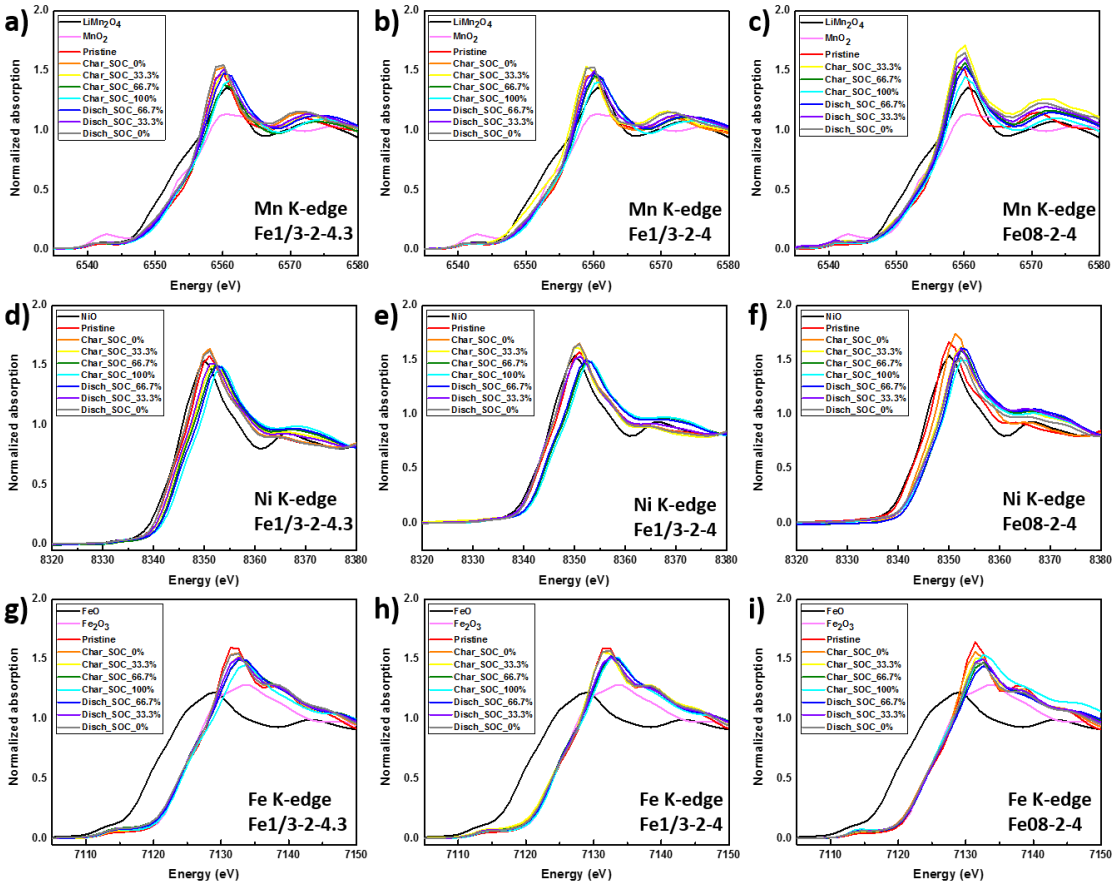

Figure 5. 9: XANES K-edge spectra of (a, b, c) Mn, (d, e, f) Ni and (g, h, i) Fe ions of (a, d, g) Fe1/3-2-4.3, (b, e, h) Fe1/3-2-4 and (c, f, i) Fe08-2-4 sample. The data are collected at various SOC state during 6th cycle corresponding to Figure 5.8.

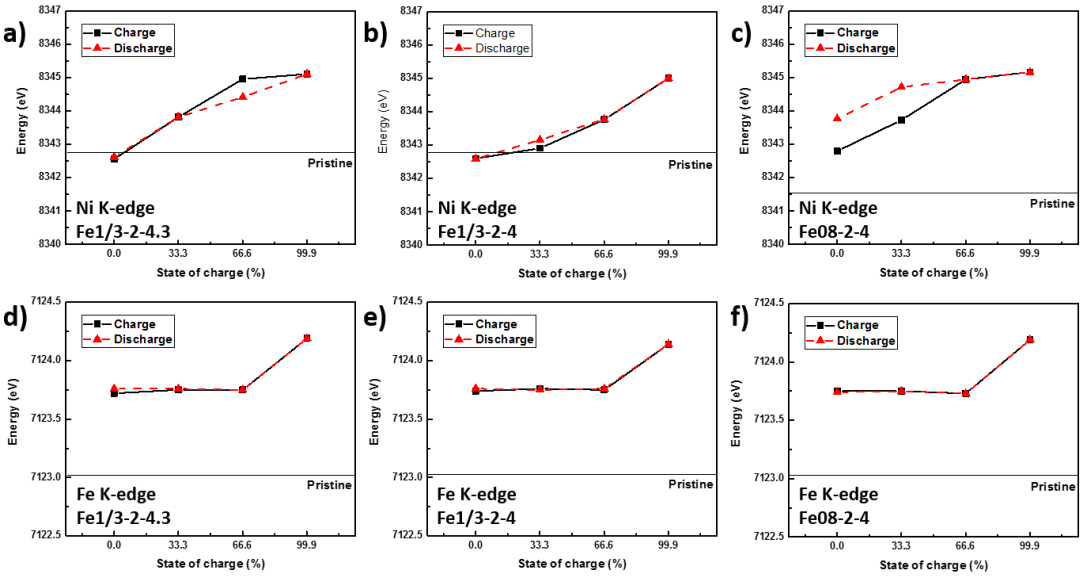

Figure 5. 10: The SOC vs. E0 plots of (a, b, c) Ni (E0,Ni) and (d, e, f) Fe (E0,Fe) ions of (a, d) Fe1/3-2-4.3, (b, e) Fe1/3-2-4 and (c, f) Fe08-2-4 sample. The data are collected at various SOC state during 6th cycle corresponding to Ni and Fe K-edge in Figure 5.8.

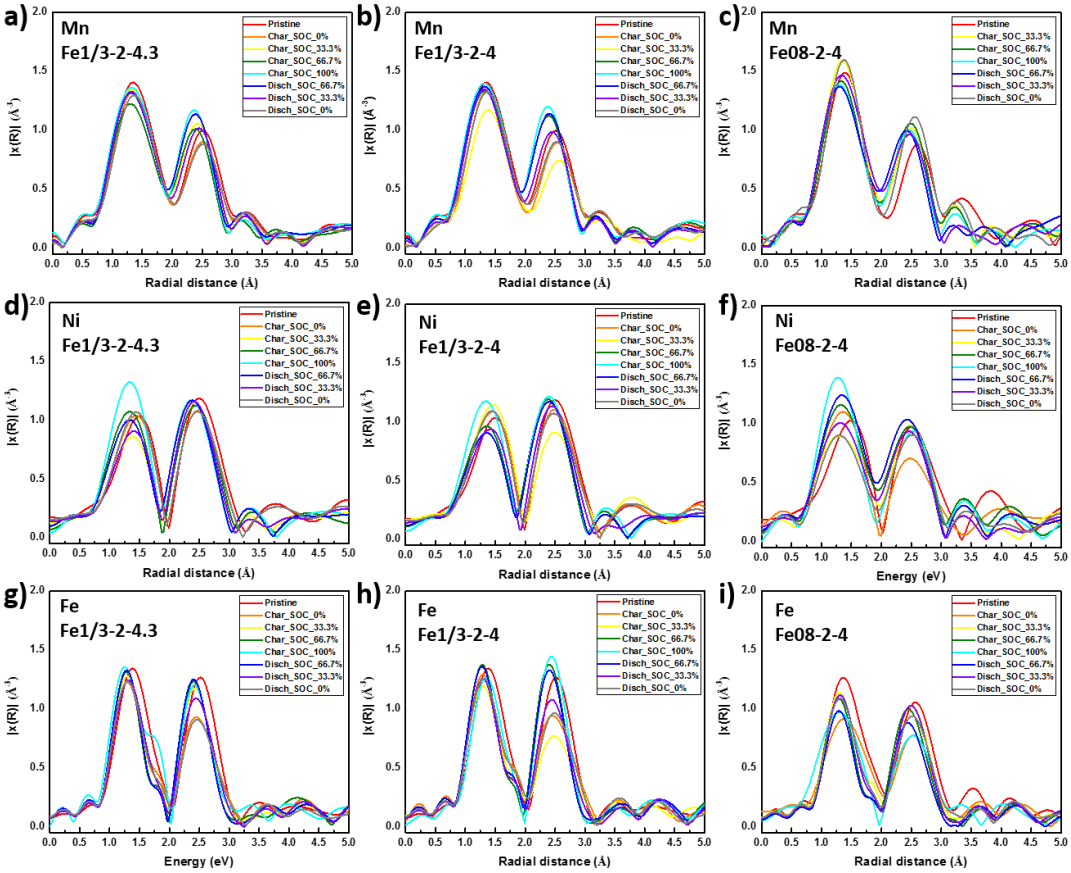

Figure 5. 11: EXAFS spectra of (a, b, c) Mn, (d, e, f) Ni and (g, h, i) Fe ions of (a, d, g) Fe1/3-2-4.3, (b, e, h) Fe1/3-2-4 and (c, f, i) Fe08-2-4 sample. The data are collected at various SOC state during 6th cycle corresponding to Figure 5.8.

Table 5. 2: Mn K-edge EXAFS fitting results of the NaNFM cathodes

	CN_Mn-O	CN_Mn-TM	R_{Mn-O} (Å)	R_{Mn-TM} (Å)	σ^2_Mn-O(*10^{-3} Å^2)	σ^2_Mn-TM(*10^{-3} Å^2)	R-factor	ΔE (eV)	k range (Å)	r range (Å)
Fe1/3-2-4.3-Pristine	5.3511	5.412	1.89470	2.93700	7.7506	8.9120	0.06353	-6.0649	3-9	1-3
Fe1/3-2-4.3-Char_SOC_0%	5.5126	5.473	1.88543	2.93111	7.2970	9.7438	0.04830	-9.9048	3-9	1-3
Fe1/3-2-4.3-Char_SOC_33.3%	5.6228	5.6665	1.87270	2.89099	6.7341	8.6671	0.02871	-10.9258	3-9	1-3
Fe1/3-2-4.3-Char_SOC_66.7%	5.6420	5.6108	1.86279	2.87147	7.5062	9.4096	0.03002	-13.1023	3-9	1-3
Fe1/3-2-4.3-Char_SOC_100%	5.5413	5.6687	1.86940	2.86315	7.3005	8.6898	0.03121	-9.0351	3-9	1-3
Fe1/3-2-4.3-Disch_SOC_66.7%	5.6810	5.6896	1.86680	2.87190	6.4911	8.1097	0.02284	-12.394	3-9	1-3
Fe1/3-2-4.3-Disch_SOC_33.3%	5.6120	5.6283	1.87677	2.90508	7.0561	8.8613	0.02891	-10.534	3-9	1-3
Fe1/3-2-4.3-Disch_SOC_0%	5.5140	5.3987	1.89000	2.93590	7.7315	9.9042	0.05683	-9.5129	3-9	1-3
	CN_Mn-O	CN_Mn-TM	R_{Mn-O} (Å)	R_{Mn-TM} (Å)	σ^2_Mn-O(*10^{-3} Å^2)	σ^2_Mn-TM(*10^{-3} Å^2)	R-factor	ΔE (eV)	k range (Å)	r range (Å)
Fe1/3-2-4-Pristine	5.3512	5.4120	1.89470	2.93703	7.7506	8.9119	0.06353	-6.0649	3-9	1-3
Fe1/3-2-4-Char_SOC_0%	5.4724	5.2976	1.88830	2.93560	7.5244	10.0431	0.06306	-10.0805	3-9	1-3
Fe1/3-2-4-Char_SOC_33.3%	5.4492	5.2767	1.89355	2.95945	9.2974	11.5671	0.0755	-10.0702	3-9	1-3
Fe1/3-2-4-Char_SOC_66.7%	5.6416	5.7089	1.86891	2.87535	6.8508	8.3951	0.02553	-11.107	3-9	1-3
Fe1/3-2-4-Char_SOC_100%	5.5577	5.7370	1.87016	2.87079	6.7895	8.2521	0.0279	-9.2451	3-9	1-3
Fe1/3-2-4-Disch_SOC_66.7%	5.6283	5.7456	1.87288	2.88415	6.6054	8.2309	0.02446	-10.6055	3-9	1-3
Fe1/3-2-4-Disch_SOC_33.3%	5.6258	5.5843	1.87018	2.90186	7.1362	9.2898	0.0306	-11.3486	3-9	1-3
Fe1/3-2-4-Disch_SOC_0%	5.5123	5.3625	1.88834	2.93545	7.4157	9.5535	0.06072	-9.8578	3-9	1-3
	CN_Mn-O	CN_Mn-TM	R_{Mn-O} (Å)	R_{Mn-TM} (Å)	σ^2_Mn-O(*10^{-3} Å^2)	σ^2_Mn-TM(*10^{-3} Å^2)	R-factor	ΔE (eV)	k range (Å)	r range (Å)
Fe08-2-4.3-Pristine	5.4285	5.3879	1.89025	2.97927	7.1123	10.1801	0.06139	-7.9405	3-9	1-3
Fe08-2-4.3-Char_SOC_0%	5.7108	5.4555	1.87207	2.93967	13.1195	11.639	0.06226	-16.4402	3-9	1-3
Fe08-2-4.3-Char_SOC_33.3%	5.8252	5.649	1.86921	2.92358	4.7449	8.3631	0.02023	-12.9167	3-9	1-3
Fe08-2-4.3-Char_SOC_66.7%	5.7128	5.8331	1.87759	2.92771	8.3362	6.5421	0.01731	-11.8888	3-9	1-3
Fe08-2-4.3-Char_SOC_100%	5.6049	5.7546	1.87051	2.91513	7.7176	9.3949	0.024	-9.8581	3-9	1-3
Fe08-2-4.3-Disch_SOC_66.7%	5.8068	5.8693	1.86092	2.89756	6.2404	8.9081	0.01557	-14.0889	3-9	1-3
Fe08-2-4.3-Disch_SOC_33.3%	5.6889	5.8188	1.87256	2.92239	5.616	8.8047	0.0244	-12.1518	3-9	1-3
Fe08-2-4.3-Disch_SOC_0%	5.5945	5.7683	1.8877	2.96193	6.1257	8.0307	0.02721	-9.6734	3-9	1-3

Table 5. 3: Ni K-edge EXAFS fitting results of the NaNFM cathodes

	1st inflection point (eV)	CN_Ni-O	CN_Ni-TM	R_{Ni-O} (Å)	R_{Ni-TM} (Å)	σ^2_Ni-O(*10^{-3} Å^2)	σ^2_Ni-TM(*10^{-3} Å^2)	R-factor	ΔE (eV)	k range (Å)	r range (Å)
Fe1/3-2-4.3-Pristine	8342.77	5.8007	5.8729	2.06438	2.97844	10.1158	6.5796	0.008316	-5.0375	3-8	1-3
Fe1/3-2-4.3-Char_SOC_0%	8342.56	5.8638	5.9372	2.07404	2.99115	9.0604	7.1427	0.004279	-8.2001	3-8	1-3
Fe1/3-2-4.3-Char_SOC_33.3%	8343.82	6.0965	6.1625	2.0066	2.9433	12.0979	6.9568	0.005635	-10.5983	3-8	1-3
Fe1/3-2-4.3-Char_SOC_66.7%	8344.96	6.0369	6.2045	1.96943	2.92192	11.3121	7.9264	0.01116	-7.2933	3-8	1-3
Fe1/3-2-4.3-Char_SOC_100%	8345.11	5.9926	6.1224	1.9233	2.8859	7.8269	7.5116	0.004065	-10.2739	3-8	1-3
Fe1/3-2-4.3-Disch_SOC_66.7%	8344.42	6.1164	6.2325	1.9505	2.9078	10.0308	7.0406	0.009763	-12.2951	3-8	1-3
Fe1/3-2-4.3-Disch_SOC_33.3%	8343.82	6.0612	6.1333	2.0206	2.9502	11.4075	6.9272	0.004959	-10.4854	3-8	1-3
Fe1/3-2-4.3-Disch_SOC_0%	8342.62	5.8723	5.9209	2.0756	2.9901	8.7477	7.2624	0.004333	-8.2198	3-8	1-3
	1st inflection point (eV)	CN_Ni-O	CN_Ni-TM	R_{Ni-O} (Å)	R_{Ni-TM} (Å)	σ^2_Ni-O(*10^{-3} Å^2)	σ^2_Ni-TM(*10^{-3} Å^2)	R-factor	ΔE (eV)	k range (Å)	r range (Å)
Fe1/3-2-4-Pristine	8342.79	5.8007	5.8729	2.06438	2.97844	10.1158	6.5796	0.008316	-5.0375	3-8	1-3
Fe1/3-2-4-Char_SOC_0%	8342.6	5.8455	5.9122	2.08219	2.99685	8.19639	6.98442	0.006373	-7.8465	3-8	1-3
Fe1/3-2-4-Char_SOC_33.3%	8342.91	5.855	5.8311	2.06543	2.9698	7.1148	12.06	0.005432	-7.731	3-8	1-3
Fe1/3-2-4-Char_SOC_66.7%	8343.77	6.1029	6.2069	1.95774	2.91251	10.2322	6.7601	0.008167	-12.0855	3-8	1-3
Fe1/3-2-4-Char_SOC_100%	8345.01	6.05278	6.1806	1.9408	2.9031	9.122	6.8973	0.006715	-9.9176	3-8	1-3
Fe1/3-2-4-Disch_SOC_66.7%	8343.78	6.1392	6.2456	1.97326	2.92512	11.2004	6.9497	0.01164	-11.6772	3-8	1-3
Fe1/3-2-4-Disch_SOC_33.3%	8343.76	6.0471	6.1212	2.04146	2.96714	10.8084	7.1956	0.004231	-8.8712	3-8	1-3
Fe1/3-2-4-Disch_SOC_0%	8342.59	5.8357	5.9059	2.08205	2.99612	7.0881	8.4558	0.006321	-8.1469	3-8	1-3
	1st inflection point (eV)	CN_Ni-O	CN_Ni-TM	R_{Ni-O} (Å)	R_{Ni-TM} (Å)	σ^2_Ni-O(*10^{-3} Å^2)	σ^2_Ni-TM(*10^{-3} Å^2)	R-factor	ΔE (eV)	k range (Å)	r range (Å)
Fe08-2-4.3-Pristine	8341.54	5.8376	5.6979	2.07749	3.00239	9.278	8.4692	0.01615	-5.91	3-8	1-3
Fe08-2-4.3-Char_SOC_0%	8342.8	5.8872	5.7209	2.01945	3.0195	8.3808	10.7359	0.015821	-7.61619	3-8	1-3
Fe08-2-4.3-Char_SOC_33.3%	8343.73	6.1186	6.0244	1.97797	2.99327	10.0141	8.1094	0.006145	-10.5084	3-8	1-3
Fe08-2-4.3-Char_SOC_66.7%	8344.95	5.9807	6.0835	1.92479	2.95522	6.526	7.5239	0.004183	-13.8856	3-8	1-3
Fe08-2-4.3-Char_SOC_100%	8345.17	5.9899	6.0513	1.92284	2.93754	7.9472	8.8758	0.001716	-10.6808	3-8	1-3
Fe08-2-4.3-Disch_SOC_66.7%	8344.95	6.0262	6.1813	1.91828	2.9409	5.5535	7.01717	0.005059	-14.3818	3-8	1-3
Fe08-2-4.3-Disch_SOC_33.3%	8344.72	5.96576	6.13965	1.94188	2.96411	8.4115	8.5	0.00461	-13.6425	3-8	1-3
Fe08-2-4.3-Disch_SOC_0%	8343.77	5.998	6.0667	1.96168	2.98017	10.6435	8.8007	0.004751	-11.8717	3-8	1-3

Table 5. 4: Fe K-edge EXAFS fitting results of the NaNFM cathodes

	1st inflection point (eV)	CN_Fe-O	CN_Fe-TM	R_{Fe-O} (Å)	R_{Fe-TM} (Å)	σ^2_Fe-O(*10^{-3} Å^2)	σ^2_Fe-TM(*10^{-3} Å^2)	R-factor	ΔE (eV)	k range (Å)	r range (Å)
Fe1/3-2-4.3-Pristine	7123.02	5.704	5.5209	2.01663	2.96731	7.6241	7.6881	0.02743	-5.5665	3-10	1-3
Fe1/3-2-4.3-Char_SOC_0%	7123.72	5.7258	5.5461	2.01358	2.97314	9.742	10.3981	0.02222	-7.7627	3-10	1-3
Fe1/3-2-4.3-Char_SOC_33.3%	7123.75	5.8577	5.8193	1.9978	2.9454	9.6295	9.1699	0.007408	-8.2096	3-10	1-3
Fe1/3-2-4.3-Char_SOC_66.7%	7123.75	5.8958	5.8754	1.99363	2.93079	9.94474	9.06134	0.009279	-9.2871	3-10	1-3
Fe1/3-2-4.3-Char_SOC_100%	7124.19	5.6514	5.8627	1.96929	2.91925	13.2466	11.2427	0.01577	-7.832	3-10	1-3
Fe1/3-2-4.3-Disch_SOC_66.7%	7123.75	5.8935	5.9138	1.9873	2.9242	9.4208	8.9288	0.007416	-9.8197	3-10	1-3
Fe1/3-2-4.3-Disch_SOC_33.3%	7123.76	5.671	5.7413	2.0028	2.9536	9.1823	9.4638	0.01408	-8.09	3-10	1-3
Fe1/3-2-4.3-Disch_SOC_0%	7123.76	5.7388	5.5008	2.00845	2.9725	9.7141	10.7277	0.02708	-8.2924	3-10	1-3
	1st inflection point (eV)	CN_Fe-O	CN_Fe-TM	R_{Fe-O} (Å)	R_{Fe-TM} (Å)	σ^2_Fe-O(*10^{-3} Å^2)	σ^2_Fe-TM(*10^{-3} Å^2)	R-factor	ΔE (eV)	k range (Å)	r range (Å)
Fe1/3-2-4-Pristine	7123.03	5.704	5.5209	2.01663	2.96731	7.6241	7.6881	0.02743	-5.5665	3-10	1-3
Fe1/3-2-4-Char_SOC_0%	7123.74	5.6941	5.4659	2.02064	2.97994	9.14216	9.71641	0.02974	-7.4047	3-10	1-3
Fe1/3-2-4-Char_SOC_33.3%	7123.76	5.6673	5.2252	2.0106	2.98286	9.7478	11.5196	0.05207	-8.9655	3-10	1-3
Fe1/3-2-4-Char_SOC_66.7%	7123.75	5.9225	5.9348	1.99165	2.92478	8.63307	7.83351	0.004014	-9.9158	3-10	1-3
Fe1/3-2-4-Char_SOC_100%	7124.14	5.8702	5.9461	1.98838	2.91936	9.1771	7.8048	0.005028	-6.1557	3-10	1-3
Fe1/3-2-4-Disch_SOC_66.7%	7123.76	5.9478	5.8702	1.99961	2.93701	8.9247	8.103	0.005014	-9.3001	3-10	1-3
Fe1/3-2-4-Disch_SOC_33.3%	7123.75	5.8787	5.7046	2.00091	2.9584	10.1114	9.6092	0.01202	-8.2346	3-10	1-3
Fe1/3-2-4-Disch_SOC_0%	7123.76	5.7264	5.4107	2.0178	2.9847	9.0832	9.4353	0.0343	-7.4343	3-10	1-3
	1st inflection point (eV)	CN_Fe-O	CN_Fe-TM	R_{Fe-O} (Å)	R_{Fe-TM} (Å)	σ^2_Fe-O(*10^{-3} Å^2)	σ^2_Fe-TM(*10^{-3} Å^2)	R-factor	ΔE (eV)	k range (Å)	r range (Å)
Fe08-2-4.3-Pristine	7123.03	5.7137	5.3683	2.02461	3.00729	7.8651	7.9413	0.04332	-6.0976	3-10	1-3
Fe08-2-4.3-Char_SOC_0%	7123.75	5.7232	5.3037	2.01268	3.01514	10.2392	10.8534	0.04395	-9.2658	3-10	1-3
Fe08-2-4.3-Char_SOC_33.3%	7123.75	5.8154	5.6478	2.00982	2.99193	10.8692	8.8687	0.01399	-8.0632	3-10	1-3
Fe08-2-4.3-Char_SOC_66.7%	7123.73	5.827	5.8035	1.98563	2.96895	11.9264	9.7071	0.00607	-10.2367	3-10	1-3
Fe08-2-4.3-Char_SOC_100%	7124.19	5.8165	5.8197	1.96055	2.96021	12.7906	11.7308	0.006691	-7.4548	3-10	1-3
Fe08-2-4.3-Disch_SOC_66.7%	7123.73	5.8635	5.7607	1.98117	2.97075	13.518	11.2469	0.008967	-10.0308	3-10	1-3
Fe08-2-4.3-Disch_SOC_33.3%	7123.75	5.7562	5.7199	2.00184	2.98314	11.2051	9.2825	0.01345	-8.3484	3-10	1-3
Fe08-2-4.3-Disch_SOC_0%	7123.74	5.6304	5.6027	2.0076	2.99158	9.6468	11.0035	0.02373	-8.332	3-10	1-3

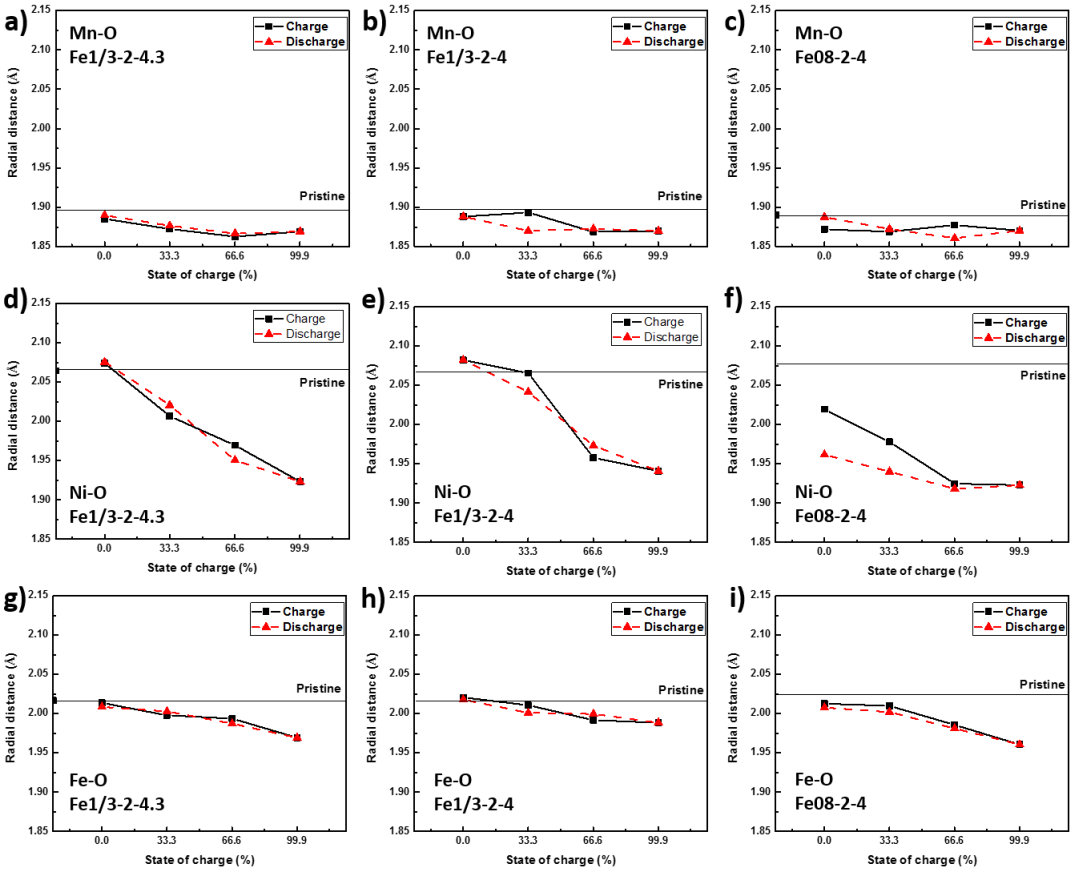

Figure 5. 12: The SOC vs. TM-O distance plots of (a, b, c) Mn-O, (d, e, f) Ni-O and (g, h, i) Fe-O ions of (a, d, g) Fe1/3-2-4.3, (b, e, h) Fe1/3-2-4 and (c, f, i) Fe08-2-4 sample. The data are collected at various SOC state during 6th cycle corresponding to Figure 5.8.

5.6 References

(1) Ryu, W. H.; Nam, D. H.; Ko, Y. S.; Kim, R. H.; Kwon, H. S. *Electrochim. Acta* **2012**, *61*, 19.

(2) Yabuuchi, N.; Yano, M.; Yoshida, H.; Kuze, S.; Komaba, S. *J Electrochem. Soc.* **2013**, *160*, A3131.

(3) Larson, A. C.; Von Dreele, R. B. *General Structure Analysis System (GSAS)*, Los Alamos National Laboratory, 2004.

(4) Xie, Y. Y.; Wang, H.; Xu, G. L.; Wang, J. J.; Sheng, H. P.; Chen, Z. H.; Ren, Y.; Sun, C. J.; Wen, J. G.; Wang, J.; Miller, D. J.; Lu, J.; Amine, K.; Ma, Z. F. *Adv. Energy Mater.* **2016**, *6*.

(5) Park, Y.; Shin, S. H.; Hwang, H.; Lee, S. M.; Kim, S. P.; Choi, H. C.; Jung, Y. M. *J. Mol. Struct.* **2014**, *1069*, 157.

(6) Balasubramanian, M.; Lee, H. S.; Sun, X.; Yang, X. Q.; Moodenbaugh, A. R.; McBreen, J.; Fischer, D. A.; Fu, Z. *Electrochem. Solid St.* **2002**, *5*, A22.

(7) Yang, L.; Ravdel, B.; Lucht, B. L. *Electrochem Solid St* **2010**, *13*, A95.

(8) Li, X.; Wu, D.; Zhou, Y. N.; Liu, L.; Yang, X. Q.; Ceder, G. *Electrochem. Commun.* **2014**, *49*, 51.

(9) Yuan, D. D.; Wang, Y. X.; Cao, Y. L.; Ai, X. P.; Yang, H. X. *Acs Appl. Mater. Inter.* **2015**, *7*, 8585.

(10) Komaba, S.; Yabuuchi, N.; Nakayama, T.; Ogata, A.; Ishikawa, T.; Nakai, I. *Inorg. Chem.* **2012**, *51*, 6211.

(11) Pan, H. L.; Hu, Y. S.; Chen, L. Q. *Energ Environ. Sci.* **2013**, *6*, 2338.

(12) Chagas, L. G.; Buchholz, D.; Wu, L. M.; Vortmann, B.; Passerini, S. *J. Power Sources* **2014**, *247*, 377.

(13) Yi, L. H.; Liu, Z. S.; Yu, R. Z.; Zhao, C. X.; Peng, H. F.; Liu, M. H.; Wu, B.; Chen, M. F.; Wang, X. Y. *Acs Sustain. Chem. Eng.* **2017**, *5*, 11005.

(14) Luo, D.; Li, G. S.; Fu, C. C.; Zheng, J.; Fan, J. M.; Li, Q.; Li, L. P. *Adv. Energy Mater.* **2014**, *4*.

(15) Nayak, P. K.; Grinblat, J.; Levi, M. D.; Haik, O.; Levi, E.; Talianker, M.; Markovsky, B.; Sun, Y. K.; Aurbach, D. *Chem. Mater.* **2015**, *27*, 2600.

(16) Nayak, P. K.; Levi, E.; Grinblat, J.; Levi, M.; Markovsky, B.; Munichandraiah, N.; Sun, Y. K.; Aurbach, D. *Chemsuschem* **2016**, *9*, 2404.

(17) Bhaskar, A.; Krueger, S.; Siozios, V.; Li, J.; Nowak, S.; Winter, M. *Adv. Energy Mater.* **2015**, *5*.

(18) Wang, P. F.; Yao, H. R.; Liu, X. Y.; Zhang, J. N.; Gu, L.; Yu, X. Q.; Yin, Y. X.; Guo, Y. G. *Adv. Mater.* **2017**, *29*.

(19) Li, X.; Wang, Y.; Wu, D.; Liu, L.; Bo, S. H.; Ceder, G. *Chem. Mater.* **2016**, *28*, 6575.

(20) McBreen, J. *J. Solid State Electr.* **2009**, *13*, 1051.

(21) Yoon, W. S.; Balasubramanian, M.; Chung, K. Y.; Yang, X. Q.; McBreen, J.; Grey, C. P.; Fischer, D. A. *J. Am. Chem. Soc.* **2005**, *127*, 17479.

(22) Qiao, R. M.; Dai, K. H.; Mao, J.; Weng, T. C.; Sokaras, D.; Nordlund, D.; Song, X. Y.; Battaglia, V. S.; Hussain, Z.; Liu, G.; Yang, W. L. *Nano Energy* **2015**, *16*, 186.

(23) Ito, A.; Sato, Y.; Sanada, T.; Hatano, M.; Horie, H.; Ohsawa, Y. *J Power Sources* **2011**, *196*, 6828.

(24) Oh, S. M.; Myung, S. T.; Yoon, C. S.; Lu, J.; Hassoun, J.; Scrosati, B.; Amine, K.; Sun, Y. K. *Nano Lett.* **2014**, *14*, 1620.

(25) Yue, J. L.; Yin, W. W.; Cao, M. H.; Zulipiya, S.; Zhou, Y. N.; Fu, Z. W. *Chem. Commun.* **2015**, *51*, 15712.

(26) Zhang, W.; Duchesne, P. N.; Gong, Z. L.; Wu, S. Q.; Ma, L.; Jiang, Z.; Zhang, S.; Zhang, P.; Mi, J. X.; Yang, Y. *J. Phys. Chem. C* **2013**, *117*, 11498.

(27) Ammundsen, B.; Jones, D. J.; Roziere, J.; Burns, G. R. *Chem. Mater.* **1996**, *8*, 2799.

(28) Lin, F.; Liu, Y. J.; Yu, X. Q.; Cheng, L.; Singer, A.; Shpyrko, O. G.; Xing, H. L. L.; Tamura, N.; Tian, C. X.; Weng, T. C.; Yang, X. Q.; Meng, Y. S.; Nordlund, D.; Yang, W. L.; Doeff, M. M. *Chem. Rev.* **2017**, *117*, 13123.

(29) Yang, W.; Devereaux, T. P. *J. Power Sources* **2018**, *389*, 188.

(30) Lin, F.; Nordlund, D.; Markus, I. M.; Weng, T. C.; Xin, H. L.; Doeff, M. M. *Energ Environ. Sci.* **2014**, *7*, 3077.

(31) Liu, X. S.; Wang, D. D.; Liu, G.; Srinivasan, V.; Liu, Z.; Hussain, Z.; Yang, W. L. *Nat. Commun.* **2013**, *4*.

(32) Qiao, R. M.; Wang, Y. S.; Olalde-Velasco, P.; Li, H.; Hu, Y. S.; Yang, W. L. *J. Power Sources* **2015**, *273*, 1120.

CHAPTER SIX: LI-SUBSTITUTED LAYERED-SPINEL CATHODE MATERIAL

6.1 Introduction

Inspired by the advantages of O3-$Na(Ni_xFe_yMn_z)O_2$ cathode materials, the design strategies of Li substitution, layered-tunneled intergrown phases and tunneled spinel phase with improved structural stability and Na mobility, we report here a Li-substituted layered-tunneled O3/spinel $Na(Ni_xFe_yMn_z)O_2$ cathode material, $Na_{0.87}Li_{0.25}Ni_{0.4}Fe_{0.2}Mn_{0.4}O_{2+\delta}$ (LS-NFM) for enhanced sodium ion storage and cycling stability. The LS-NFM electrode was prepared by adjusting the stoichiometric ratio of the Na ion over the sum of Li and transition metal ions below 1. The Rietveld refinement of XRD data indicated that the cathode is composed of 94% layered and 6% spinel components. The great structural compatibility and connectivity of the two phases are confirmed by XRD, selected area electron diffraction (SAED) and high-resolution transmission electron microscopy (HRTEM). The galvanostatic intermittent titration (GITT) analysis suggested that the Na ion diffusivity of LS-NFM has significantly improved compared to the single-phased un-doped NFM control. When cycled at a high current density of 100 mA g^{-1}, LS-NFM cathode exhibited a first-cycle Coulombic efficiency of 88% and reversible discharge capacity of 96 mAh g^{-1} after 100 cycles with the capacity retention of 86%. Structural characterization by *ex situ* soft and hard x-ray absorption spectroscopy (XAS) suggested that the capacity of LS-NFM largely resulted from the N^{2+}/Ni^{4+} redox couple and slightly from Fe^{3+}/Fe^{4+} redox couple.

6.2 Experimental Section

6.2.1 Materials Synthesis.

All of the chemicals were purchased from Sigma-Aldrich, (purity≥99%). LS-NFM was prepared by a solid state reaction of the co-precipitated precursor $(Ni_{0.4}Fe_{0.2}Mn_{0.4})C_2O_4$, Li_2CO_3 and Na_2CO_3. For precursor synthesis, the stoichiometric amount of $NiSO_4 \cdot 6H_2O$, $FeSO_4 \cdot 7H_2O$, $MnSO_4 \cdot H_2O$ was dissolved in water and then added into the $Na_2C_2O_4$ solution. The solution was then kept at 70 ^oC for 3 hours under stirring in air, and the resultant powder was filtered, washed, and dried in air at 105 ^oC.[1] The as-prepared precursor powder was grinded together with stoichiometric amounts of Li_2CO_3 and Na_2CO_3 for one hour and then pressed into pellets. The pellets were heated at 500 ^oC for 8 hours followed by 800 ^oC for 8 hours in the tube furnace with the flow of mixed oxygen/Argon gas (O_2:Ar = 1:4 v/v). Un-doped $NaNi_{0.4}Fe_{0.2}Mn_{0.4}O_2$ (NFM) was also prepared by a solid state reaction of co-precipitated precursor $Ni_{1/2}Mn_{1/2}(OH)_2$, Fe_2O_3 and Na_2CO_3 for comparison.[2] The stoichiometric amounts of chemicals were grinded for one hour and then pressed into pellets. The pellets were heated at 800 ^oC for 24 hours in air. Both cathodes were transferred into glove box immediately to avoid contact with moisture in the air.

6.2.2 Structural Characterizations

XRD patterns were obtained by a Rigaku Miniflex 600 with Cu-Kα radiation (λ = 1.5418Å) and powder samples were tested in a flat sample stage and scanned from 5° to 120° (2θ) at the rate of 0.8˚/min and 0.01˚ /step. Then the structure was analyzed by General Structure Analysis System (GSAS) package.[3] The cycled laminated electrodes were scanned in the range of 10° to 80^o (2θ). The morphology of LS-NFM sample was

characterized by a field-emission scanning electron microscope (FESEM, FEI Teneo) at an accelerating voltage of 15 kV. The TEM images were acquired by a JEOL 2100F with the accelerating voltage of 200 kV. TEM specimens of cycled samples were prepared in an Ar-filled dry glove box (O_2 < 0.5 ppm). A Gatan vacuum transfer holder was employed to transfer the specimen from the glove box to a JEOL 2100F microscope directly without exposure to air. The soft X-ray adsorption spectroscopy (XAS) measurements were carried out at beamline 8−2 at the Stanford Synchrotron Radiation Lightsource (SSRL). Data was acquired under ultrahigh vacuum (10−9 Torr.) conditions in a single load at room temperature, using total electron yield (TEY) via the drain current. Hard XAS measurements for the Ni, Fe, and Mn K-edge were performed at the Advanced Photon Source on beam-line 5-BM-D in transmission mode. All the *ex situ* samples were harvested from the cycled cells, cleaned, and sealed with Kapton tape in Ar-filled dry glove box. The samples were subjected to the measurements immediately after they were taken out from sealed containers. EXAFS data processing and analysis were performed using the IFEFFIT package.[4] The normalized extended X-ray absorption fine structure (EXAFS) spectra was converted from energy to wave vector *k* and then weighted by k^3. The coordination number was fixed as 6 for the first shell transition metal-oxygen (TM-O), 6 for the second shell transition metal-transition metal (TM-TM).

6.2.3 Electrochemical Characterizations

Both LS-NFM and NFM laminated electrodes were prepared by mixing 80% active materials, 10% super carbon C45 (Timcal America Inc.) and 10% poly(vinylidene fluoride) (PVDF), and screen-printed on an aluminum current collector. The electrode was punched into 1.5 cm dia. discs using Precision Disc Cutter (MTI) with a loading density of ~2.7 mg

cm^{-2}. The half-cells were prepared with LS-NFM or NFM cathode electrodes, glass fiber separators (Celgard) and sodium counter electrode in an electrolyte of 1M $NaPF_6$ in propylene carbonate (PC). Both cathodes were cycled on an Arbin battery tester with the potential window of 2 - 4.2 V. GITT was conducted on a Maccor battery tester with the cell charged/discharged at a current density of 12 mA g^{-1} for a pulse of 30 min followed by a relaxation of 12 h to approach the steady state value where the voltage variation is less than 3 mV h^{-1}. All of samples were pre-cycled prior to GITT measurements.

6.3 Results and Discussion

The LS-NFM is designed such that a mixed-phased O3/spinel structure can be formed. Specifically, the ratio between Na ions over the sum of Li and transition metal ions is adjusted to be below 1 as it has been shown that O3 phase may not form at high Na content.[5,6] In addition, the separate spinel phase is more favorable over pure layered phase when the Li content is high. However, if the Li content is too high it can lead to P2 phase evolution.[5] At the same time, we also need to consider that there are limited cation sites in the structure but sufficient Na sources should be put in order to provide high capacity. Therefore, the final composition was designed as $Na_{0.87}Li_{0.25}Ni_{0.4}Fe_{0.2}Mn_{0.4}O_{2+\delta}$, which was confirmed by ICP-MS.

The morphology of the LS-NFM electrode is investigated by SEM. Figure 6.1 shows that the material is composed of plate-shaped particles. The XRD patterns of as-prepared LS-NFM and un-doped NFM samples are presented in Figure 6.2 and Figure 6.3, respectively. Structural parameters through Rietveld refinement are summarized in Table 6.1. The lattice parameters of LS-NFM were refined based on the rhombohedral α-$NaFeO_2$ structure (space group: R-3m) and cubic spinel structure (space group: Fd-3m) as the

secondary phase. The calculated pattern is in good agreement with the experimental data where R_{wp}=2.35% and R_p=1.37%. The Rietveld refinement result suggests that the LS-NFM material is composed of 94 % of a dominant α-$NaFeO_2$ phase with the lattice parameters of $a = b$ = 2.9550(2) Å, c = 15.903(1) Å and 6% of a secondary spinel phase with a = 8.1806(8) Å. For the XRD pattern of NFM, single α-$NaFeO_2$ phase was refined with the lattice parameters of $a = b$ = 2.96894(4) Å, c = 16.0119(4) Å. A slight lattice shrinkage along *z*-axis was observed in the LS-NFM sample compared to the NFM sample, which may due to partial oxidation of Ni^{2+}(0.69 Å) to Ni^{3+}(0.56 Å) because of the substitution of Li ions in the transition metal layer, and the result is consistent with previous report.[7] Moreover, we conducted *ex situ* XRD on the as-prepared and 1st discharged (sodiated) laminated electrodes to investigate the structural evolution (Figure 6.4) upon cycling. The cycled samples were covered by Kapton tape to prevent exposure to air. Both XRD patterns showed a dominant O3-type layered structure with the secondary spinel phase. The asterisk-marked peaks at 18.29 ^{o}, 43.77^o and 63.80^o correspond to the (111), (400) and (511) planes of the spinel phase, respectively. In terms of the layered O3 phase, the (003) and (006) planes shifted to a higher angle after the 1st discharging process, suggesting a slight decrease in *c*. Due to the electrostatic attraction between Na^+ and O^{2-} ions, the decrease in *c* can be ascribed to a higher concentration of Na^+ ions into the layered structure, filling in the Na vacancies in the as-prepared sample (Table 6.1).[8]

The as-prepared, 1st discharged and 50th discharged LS-NFM samples were also investigated by TEM (Figure 6.5). The HRTEM images are shown in Figure 6.5 (a), 6.5 (b) and 6.5 (c) where the red and white dashed square indicate the spinel and layered components, respectively, and the insets are the corresponding fast Fourier transform (FFT)

images. The HRTEM image of the as-prepared LS-NFM sample (Figure 6.5 (a)) exhibits the (003) plane of the layered phase and the (111) plane of the spinel phase where nanoscale domains of the layered and spinel components are structurally integrated. It is worth noting the great structural compatibility and connectivity of the two close-packed structures.[9] After the 1st discharge, the close-packed layered and spinel phase in the LS-NFM sample remained in the structure (Figure 6.5 (b)), which is consistent with the *ex situ* XRD results (Figure 6.4). Note that after 50 cycles, the layered and spinel structure still preserve, suggesting the great structural reversibility and stability. The SAED images of the as-prepared, 1st discharged and 50th discharged LS-NFM sample are shown in Figure 6.5 (d), 6.5 (d) and 6.5 (f), respectively where the red circles and white arrows indicate planes from the spinel and layered phase, respectively. SAED pattern of the as-prepared LS-NFM displays a dominant polycrystalline layered O3-type structure and the minor spinel phase, consistent with the XRD result that the LS-NFM cathode contains a large amount of layered structure (94%) and a small fraction of the spinel phase (6%). The existence of the spinel phase in the 1st discharged sample (Figure 6.5 (e)) as well as the 50th charged sample (Figure 6.5 (f)) suggests good structural stability of the LS-NFM cathode.

The voltage profiles of LS-NFM and NFM electrodes cycled with a potential window of 2 - 4.2 V at 12 mA g^{-1} are presented in Figure 6.6 (a) and 6.6 (b), respectively. The corresponding d*Q*/d*V* plots are shown in Figure 6.7. Both cathodes have a similar plateau region during the charging (~2.75-2.9 V) and discharging (2.8 - 2.5 V) process, which correspond to the reversible phase transitions between O3 and P3 phases.[10-15] In addition, both cathodes exhibit a plateau at ~4.16 V (Figure 6.6 (a) and 6.6 (b)) as can be also indicated by the oxidation peak in the dQ/dV plots (Figure 6.7) during the charging

process, which could be associated with the phase transition from P3 to O3' (also known as O3 phase at high voltage).[10,12,13] Moreover, side reactions with electrolyte, formation of solid electrolyte interphase (SEI) and/or polarization may also contribute to the plateau at high voltage.[16-18] For the discharging process of the NFM cathode, a distinct plateau at 3.9 - 4.1V gradually became sloping after 10 cycles and the corresponding peak intensity in the dQ/dV plot significantly decreased (Figure 6.7), which can be attributed to the irreversible transition from O3' to P3 phase[10] and/or detrimental co-insertion of solvent in the electrolyte at high voltages.[11,19] On the other hand, the plateau at ~4.16 V of the LS-NFM cathode maintains for subsequent cycles (Figure 6.7) during the discharging process, suggesting a reversible phase transition. The sloping profiles between the plateaus at higher and lower voltages, for both cathodes could be related to a solid-solution reaction with P3 structure.[11] The first charge capacity of LS-NFM and NFM is 180 mAh g^{-1} and 205 mAh g^{-1}, respectively. And the first-cycle Coulombic efficiency of the LS-NFM cathode (73%) has been significantly enhanced compared to the NFM cathode (52%), which is possibly due to the structural stabilization by the spinel phase in the mixed phased LS-NFM cathode. Although the Coulombic efficiency has been improved in LS-NFM cathode, it is not high possibly due to the irreversible side reaction at the surface or the formation of SEI at high upper cutoff potential (4.2V).[20-22]

We have studied the cycling performance of both LS-NFM and NFM electrodes (Figure 6.6 (c)) at a current rate of 100 mA g^{-1}. The 1st discharge capacity of NFM (104 mAh g^{-1}) is much smaller than that of LS-NFM (112 mAh g^{-1}). Moreover, LS-NFM exhibits a higher discharge capacity and capacity retention (96 mAh g^{-1}, 86%) than the NFM control (75 mAh g^{-1}, 70%) after 100 cycles, indicating a significantly improved

cycling performance of LS-NFM cathode. The first-cycle Coulombic efficiency of LS-NFM is 88% and approaches 99% after 5 cycles, much faster than the NFM cathode, which reaches 99% Coulombic efficiency after 28 cycles. The improved Coulombic efficiency is possibly due to the unique design of the LS-NFM cathode with the inter-grown spinel phase stabilizing the layered structure.

One of the advantages of the layered-spinel cathodes used for lithium-ion batteries is the enhanced rate capability due to the shortened diffusion path that is created by the integration of 3D channels (spinel phase), and 2D channels (layered phase).[23,24] We also investigated the rate capability of our layered-spinel cathode for sodium ion batteries (Figure 6.6 (d)). Both LS-NFM and NFM cathodes were cycled at the rate of 12 mA g^{-1}, 36 mA g^{-1}, 120 mA g^{-1}, 36 mA g^{-1}, and back to 12 mA g^{-1}. The LS-NFM cathode delivered 129 mAh g^{-1} at 12 mA g^{-1} and 101 mAh g^{-1} at 120 mA g^{-1}. When cycled back to the low current rate of 12 mA g^{-1}, it delivered a capacity of 118 mAh g^{-1}, with a 92 % capacity retention. In contrast, the NFM cathode delivered 106 mAh g^{-1} and 66 mAh g^{-1} in capacity at the initial rates of 12 mA g^{-1} and 120 mA g^{-1}. It exhibited a capacity of 84 mAh g^{-1} when cycled back to the low rate of 12 mA g^{-1}, with an 80% capacity retention. The LS-NFM electrode exhibited a better rate capability and capacity retention compared to the NFM electrode. The improved rate capability in LS-NFM electrode suggests faster charge transport kinetics within the LS-NFM cathode, thus we conducted GITT to investigate the Na^+ diffusion coefficient of cycled LS-NFM and NFM electrodes (Figure 6.8 (a)). The diffusion coefficient can be expressed as the following equation:

$$D_{Na+} = \frac{\pi}{4}\left(\frac{m_B V_M}{M_B S}\right)^2 \left(\frac{\Delta E_S}{\tau\left(dE_\tau / d\sqrt{\tau}\right)}\right)^2, \tau \ll \frac{L^2}{D_{Na+}} \quad (1)$$

where m_B, V_M, M_B, S and τ are the mass (g), molecular volume (cm^3/mol), molecular weight (g/mol), active surface area (cm^2) and current pulse time (s) of the active material. If E versus $\sqrt{\tau}$ shows a linear behavior during the current pulse (Figure 6.9), the equation can be transformed into:

$$D_{Na+} = \frac{\pi}{4\tau}\left(\frac{m_B V_M}{M_B S}\right)^2\left(\frac{\Delta E_S}{\Delta E_\tau}\right)^2, \tau \ll \frac{L^2}{D_{Na+}} \quad (2)$$

Where ΔE_S and ΔE_τ for each titration are illustrated in Figure 6.9.

For the LS-NFM and NFM electrode, the molecular volume is calculated by the information obtained by the XRD Rietveld refinement where V_M of LS-NFM and NFM is 120.2584 $Å^3$ and 122.2295 $Å^3$, respectively. The molecular weight is calculated by the nominal composition of the materials where LS-NFM and NFM is 110.3557 g/mol and 111.6094 g/mol, respectively. The active surface area of LS-NFM and NFM is measured by nitrogen gas adsorption and desorption isotherms and calculated by the standard multipoint Brunauer-Emmett-Teller (BET) method. The active surface area of LS-NFM and NFM is 2.3715 m^2/g and 2.6727 m^2/g, respectively.

At the beginning of the charging process, the diffusion coefficient of LS-NFM (2.4 x 10^{-13} cm^2 s^{-1} at 2.67 V) is about one magnitude higher than that of NFM (1.44 x 10^{-14} cm^2 s^{-1} at 2.80 V), and the diffusivity of LS-NFM surpasses that of the NFM cathode until the electrodes are charged to 3.75 V. Moreover, the diffusivity of the LS-NFM electrode during the discharge process is also approximately one magnitude higher than that of the NFM electrode throughout the whole potential window. The LS-NFM electrode exhibits a faster Na^+ diffusivity in both charge and discharge processes compared to NFM electrode. This result is in good agreement with the rate capability study discussed above. The improved Na^+ diffusivity in LS-NFM is possibly due to the 3D diffusion channels from the spinel

structure that provide direct connectivity between layered and spinel components, which greatly shorten the ion diffusion distance. This hypothesis has been investigated in layered-spinel cathode materials for lithium ion batteries.[23,25-27] The diffusion coefficients of LS-NFM drops when the voltage is near 2.82 V, and recovers at 2.93 V, which can be explained by the phase transformation between O3 and P3 phases,[11] consistent with the plateau region in the voltage profiles (Figure 6.6). This sluggish electrochemical reaction implies the O3-P3 phase transformation is a kinetically controlled process associated with the complex Na ion/vacancy ordering and host rearrangement.[28] At the region of 2.93-3.63 V, the diffusion coefficients in both LS-NFM and NFM electrodes remain stable, indicating a relatively low kinetic barrier of Na ion extraction from the host materials. When the electrodes are charged above 3.63 V, the significant decrease of the diffusion coefficient of LS-NFM can be ascribed to the sluggish phase transformation from P3 to O3' phase, which was observed in *in situ* XRD studies elsewhere.[10,12] On the other hand, the decrease of diffusion coefficient at high voltage is not observed in the NFM cathode, possibly due to the irreversible P3-O3' phase transition during the initial cycle. Indeed, the long plateau at ~4.16 V during the 1st charge (Figure 6.6) becomes sloping after 1st cycle and the corresponding peak intensity in dQ/dV (Figure 6.7) significantly decreases, both of which suggest the irreversible P3-O3' phase transition.

The *ex situ* XAS was conducted to explore the chemical environment of transition metals at various states of charge (SOC) including: pristine, charged to 4.0 V, charged to 4.2 V, discharged to 2.4 V and discharged to 2.0 V (Figure 6.10). X-ray absorption near edge structure (XANES) spectra at Ni, Mn and Fe K-edges are shown in Figure 6.10 (a), 6.10 (b) and 6.10 (c), respectively. The onset of the transition metal k-edge is resulted from

the symmetry-allowed transitions from the 1s core electron to excited vacant bound states.[29] The pre-edge absorption is formally electric dipole-forbidden transition of a 1s electron to an unoccupied 3d orbital.[29,30] The first strong absorption in the low-energy region is corresponding to a shakedown process originally, from the ligand-to-metal charge transfer (LMCT).[23,31] The main absorption edge is due to the electric dipole allowed transition from 1s to a 4p state.[29,30,32] The Ni k-edge spectra of the pristine sample and the NiO standard closely resemble each other, indicating the existence of Ni^{2+}. A significant shift of the edge to higher energy is observed during the charge process, suggesting the oxidation of Ni^{2+} ions during the extraction of Na^{+} ions. The Ni k-edge spectra gradually shift back to the pristine low-energy region during the discharge process, suggesting the reversible reduction of high oxidation state Ni ions back to Ni^{2+}. The edge position of the Mn k-edge spectrum of the pristine LS-NFM sample is similar to that of the MnO_2 standard, indicating the pristine sample contains tetravalent Mn ions. As the Na ions are (de)intercalated, the shape of Mn k-edge spectra changes due to the changes in the Mn local environment but there is not a rigid shift to higher energy. A small shift of edge position during the charge and discharge process is observed, which is consistent with a previous study on NFM ($NaNi_{0.25}Fe_{0.5}Mn_{0.25}O_2$) electrodes.[33] Since it is very difficult to oxidize Mn^{4+} to a higher valence state electrochemically, the small shift can be presumably attributed to the change of the local structure of manganese coordination.[19,34] Figure 6.10 (b) inset shows the pre-edge features of Mn k-edge spectra of samples at different states of charge (SOC) where P1 and P2 correspond to transitions from 1s to $3de_g$ and $3dt_{2g}$ with a weak crystal field, respectively. A very subtle increase in intensity confirms the negligible valence change of Mn ions. The oxidation state of Fe ions can be determined by the

inflection point of the Fe k-edge spectra, which is indicated by the peak maxima in the first-derivative curve (Figure 6.10 (c) inset).[35,36] The inflection points of the pristine, 4.3V-charged and 2.0V-discharged samples locate at 7129.8 eV, 7131.4 eV and 7130.0 eV, respectively. A small shift of the inflection points to higher energy when charged above 4.0 V indicates that the Fe ions are slightly oxidized. When discharged back to 2.0 V, the peak maxima shifted back to the position of pristine sample, suggesting a reversible Fe ion redox reaction, consistent with a previous study.[13] In summary, in this layered-spinel cathode material, nickel is the dominant electrochemical redox species and largely contributes to the specific capacity along with minor contribution from Fe.

In addition to the investigation of the chemical state in the bulk material, soft XAS (sXAS) is used to probe chemical environments at the surface with depth sensitivities. The incident X-rays are absorbed by the sample through excitation of core-level electrons to unoccupied states above the vacuum or Fermi level.[37,38] Total electron yield (TEY) accounts for all the electrons escaping from the surface of the material, and is measured by the net current that flows into the sample to neutralize the positively charged sample by escaped electrons.[39] The probing depth of TEY mode is approximately 2-5 nm due to the mean free path of electrons in the sample, largely representing the surface environment of examined materials.[37] Figure 6.10 (d) shows the TEY mode of Ni L3 edge of the LS-NFM samples. The splitting of the edge can be attributed to the Ni2p-Ni3d electrostatic interaction and crystal field effect.[40] The integrated peak ratio of split edge at high energy ($L3_{high}$) over low energy ($L3_{low}$) has a positive relation with the oxidation state of nickel.[40] The split edge ratio of pristine, 4.0 V-charged and 4.3V-charged sample are 0.56, 1.73 and 2.22, respectively, suggesting the cathode is gradually oxidized during the charging

process. While during the discharging process, the ratios of 2.8V-discharged, 2.4V-discharged and 2.0V-discharged states are 0.90, 0.58 and 0.56, respectively, suggesting the reduction of Ni ions. The ratio of pristine and fully-discharged samples are both 0.56, suggesting great reversibility of Ni redox couple. The TEY mode spectra of Mn L3 edge of the *ex situ* samples are also shown in Figure 6.10 (e). The peak at 640 eV corresponds to Mn^{2+} ions, the peak at 641.36 and 641.97 eV to Mn^{3+} ions, and the peak at 640.71 and 643.05 eV to Mn^{4+} ions, as illustrated by the dashed lines.[31,41] The pristine sample shows dominant Mn^{4+} ions in the structure. Little change is observed during the charging process to 4.2V. However, a significant amount of Mn^{4+} ions are reduced to Mn^{3+} and Mn^{2+} ions when discharged to 2.8V. The reduction of Mn^{4+} ions continued during the discharging process to 2.0V. Note that in the traditional O3-type layered NFM cathode ($NaNi_{0.25}Fe_{0.5}Mn_{0.25}O_2$), Mn^{4+} ion in the bulk is not electrochemically active during both charging and discharging processes.[33] However, Mn^{4+} ions possibly react with trace amount of moisture in the electrode-electrolyte interface, leading to the slight reduction of Mn^{4+} ions to Mn^{3+} ions, which has been observed in a previous study of a single-phased R -3 m Li-doped NFM cathode ($Na[Li_{0.05}(Ni_{0.25}Fe_{0.25}Mn_{0.5})_{0.95}]O_2$) where a small shift during the charging process from Mn^{4+} to Mn^{3+} ions was observed by XPS.[7] In the layered-spinel cathode, a small amount of Mn^{2+} ions are generated during the charging process, presumably indicating that Mn^{4+} ions are firstly reduced to Mn^{3+} ions, followed by the disproportionate reaction $2Mn^{3+} = Mn^{2+} + Mn^{4+}$ of the specific and particular spinel composition at the electrode surface.[42] This reaction might form a surface layer, blocking the insertion of the solvent molecules and/or electrolyte anions into the layered structure, and therefore enhance the structural stability.[11,19] Furthermore, a reduction of Mn^{4+} ions to

Mn^{3+} and Mn^{2+} ions is observed during the discharging process. As for Fe L3 edge, the ratio of split edge at high energy over low energy has a positive relation with the oxidation state of iron.[43] The ratio of integrated intensity at high energy over that at low energy increases from pristine to charged-4.0 V sample, suggesting Fe ions are oxidized when charged above 4.0V, consistent with the XANES result (Figure 6.10 (c)) and the practical 1st charge capacity (Figure 6.6 (a)).

We have examined the local structural evolution of the LS-NFM cathode by hard x-ray EXAFS spectra. Figure 6.11 (a), 6.11 (b) and 6.11 (c) show the Fourier transform magnitudes of Ni, Mn and Fe K-edge spectra, respectively. The first intense peak is attributed to the TM-O coordination shell and the second is TM-TM shell. The quantitative fitting of EXAFS spectra shown in Figure 6.11(d), 6.11(e) and 6.11(f) (fitting details are provided in Table 6.2) provides the distances of TM-O and TM-TM bonds. For the pristine sample, the distances of Ni-O, Mn-O and Fe-O are 2.07 Å, 1.91 Å and 2.02 Å, respectively, consistent with the Shannon's ionic radii where the distance of Ni^{II}-O, Mn^{IV}-O and Fe^{III}-O are 2.09 Å, 1.93 Å and 2.01 Å, respectively, suggesting the good fitting of EXAFS spectra.[44,45] The distance of Ni-TM, Mn-TM and Fe-TM are comparable to each other, indicating the uniform distribution of Ni, Mn and Fe ions. When charged to 4.0 V, the Ni-O distance significantly decreases to 1.92 Å, and the Fe-O distance slightly decreases to 1.97 Å, suggesting the oxidation of Ni and Fe ions. However, the negligible decrease in Mn-O distance indicated the change of local environment of Mn ion but not the change of oxidation state. Therefore, we conclude that Ni redox couple contributed to most of capacity in the LS-NFM cathode. When discharged at 2.0V, the distance of Ni-O, Mn-O and Fe-O return to 2.06 Å, 1.90 Å and 2.01 Å, respectively, suggesting the good

reversibility of all redox pairs. Moreover, all of the TM-TM distances decrease when the sample is charged above 4.0V, which is probably due to the decrease of the lattice parameter corresponding to the in-plane interatomic distance.[19] When discharged to 2.0V, all of the TM-TM distance reversibly increased. In summary, the EXAFS results exhibit the reversible evolution of both redox couple and crystal structure of a LS-NFM cathode, which is determined by the evolution of TM-O and TM-TM bonding length that decreases during the charging process and reversibly increases during the charging process. This reversible evolution presumably results from the intergrowth of spinel and layered phase that stabilized the crystal structure above 4.0V.

6.4 Conclusion

We successfully prepared a layered-spinel cathode material for sodium ion batteries by Li substitution. In the traditional Li-substituted cathode, Li ions are located at the transition metal sites and form a single phase. However, we prepared a mixed-phased layered-spinel cathode by increasing the Li stoichiometry. The Rietveld refinement on the XRD pattern suggests that the as-prepared material is composed of a 94 % dominant O3-type layered phase and 6% secondary spinel phase. The HRTEM results show the remarkable structural compatibility and connectivity of the two components, indicating an intergrowth structure. In terms of the electrochemical performance, both cycling stability and rate capability have been significantly improved in LS-NFM cathodes compared to the un-doped NFM control. It maintains a discharge capacity retention of 86% after 100 cycles at a current rate of 100 mA g^{-1} in a potential window of 2 - 4.2V, which is much better than that of the NFM control (70% capacity retention). The diffusion coefficient of LS-NFM is one magnitude higher than that of the NFM at the beginning of the charging process.

Moreover, the diffusivity of LS-NFM during the discharge process is also approximately one magnitude higher than that of the NFM sample throughout the whole potential window. It explains the superior rate capability of the LS-NFM electrode. The enhanced charge transport kinetics can be explained by the improved ion diffusion through direct channels between the 2D layered and 3D spinel component. The voltage profile of LS-NFM shows a reversible plateau above 4.0V while the high voltage plateau of the NFM cathode is irreversible, suggesting the enhanced structural and electrochemical stability of the LS-NFM cathode by the addition of the spinel phase. We further investigated the origin of the enhanced electrochemical performance in the LS-NFM cathode by *ex situ* XAS. Both hard/soft XAS results suggest that Ni^{2+}/Ni^{4+} and Fe^{3+}/Fe^{4+} redox couple are electrochemically active while the Ni^{2+}/Ni^{4+} redox couple contributes to most of the capacity in the LS-NFM cathode. Moreover, the XAS results suggest great reversibility of the redox pairs and crystal structure, which presumably is associated with the intergrowth of spinel and layered phase that stabilized the crystal structure above 4.0V. In addition to the substitution of various transition metals or the modification of the stoichiometry of each transition metal, this study provides a new strategy to improve electrochemical performance of layered cathode materials for sodium ion batteries.

6.5 FIGURES AND TABLES

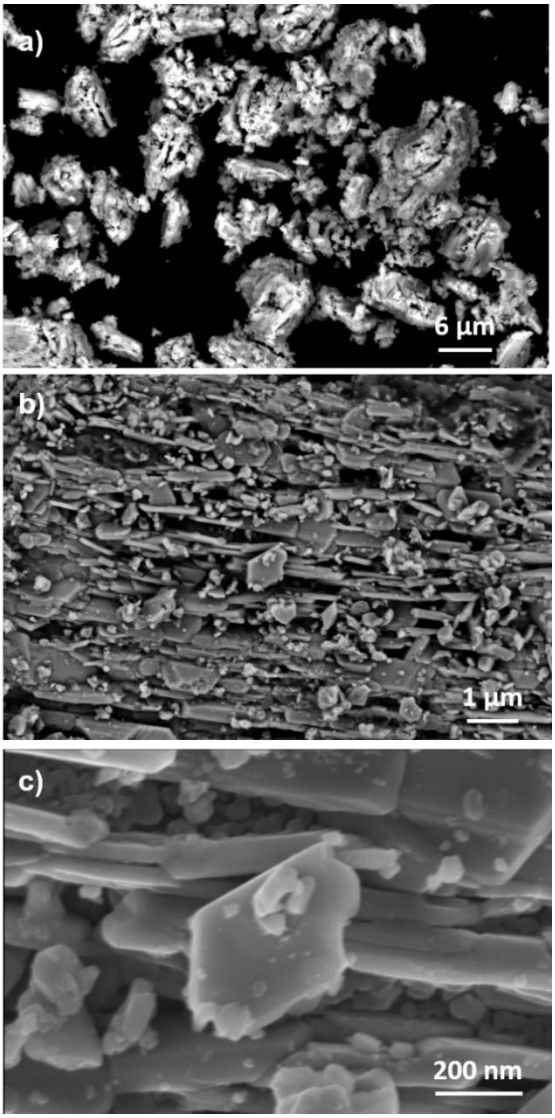

Figure 6. 1: SEM images of LS-NFM.

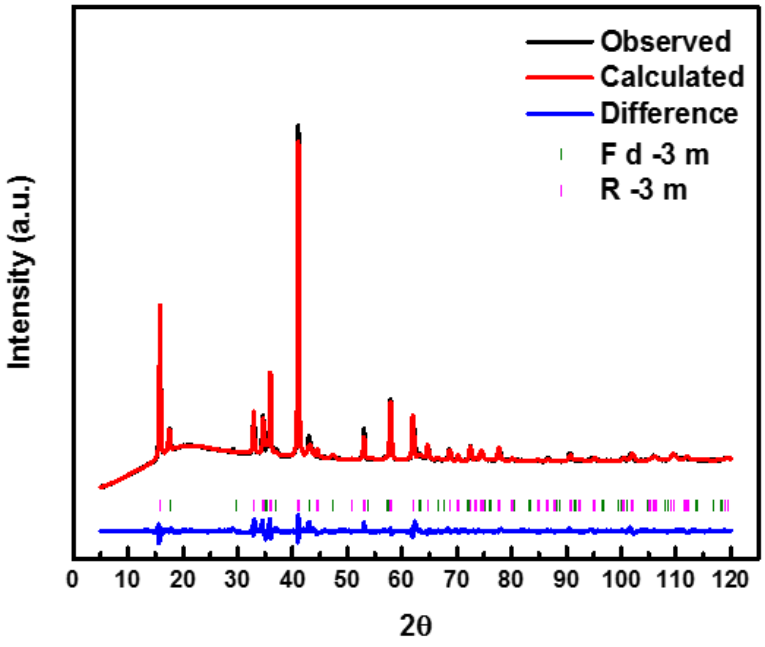

Figure 6. 2: X-ray diffraction pattern and Rietveld refinement of the as-prepared LS-NFM powders.

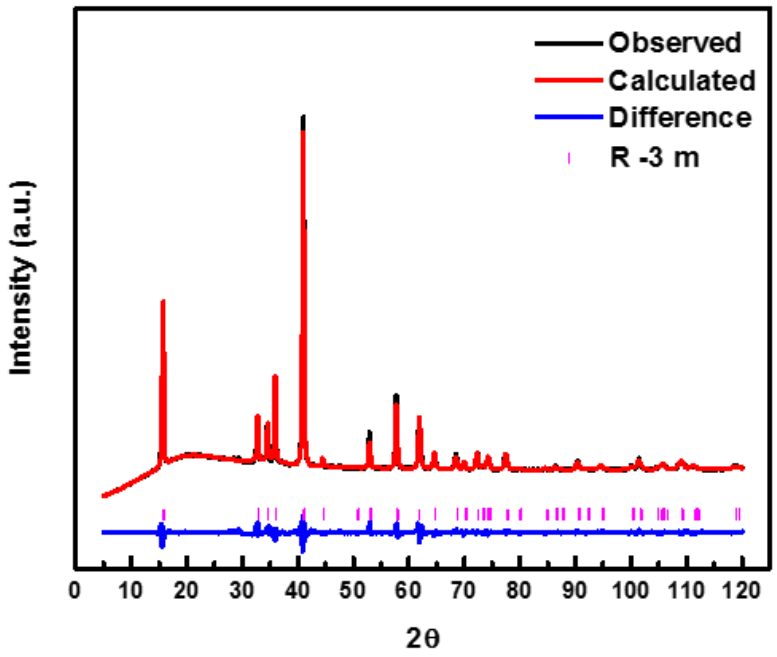

Figure 6. 3: X-ray diffraction pattern and Rietveld refinement of the as-prepared NFM powders.

Table 6. 1: Refinement results of LS-NFM and NFM cathode.

LS-NFM: R-3m phase (94 wt%)

a=2.9550(2) Å, c=15.903(1) Å, R_{wp}=2.35%, R_p=1.37%

Atom	Wyckoff	X	Y	Z	Occupancy
Na	3b	0	0	0	1
TM/Li	3a	0	0	0.5	0.857(4)
O	6c	0	0	0.2363(1)	1

LS-NFM: F d -3 m phase (6 wt%)

a=8.1806(8) Å, R_{wp}=2.35%, R_p=1.37%

Atom	Wyckoff	X	Y	Z	Occupancy
Li	8a	0.125	0.125	0.125	1
Mn	6d	0.5	0.5	0.5	1
O	32e	0.2428(1)	0.2428(1)	0.2428(1)	1

NFM: R-3m phase (Single)

a=2.96894(4) Å, c=16.0119(4) Å, R_{wp}=2.22%, R_b=1.33%

Atom	Wyckoff	X	Y	Z	Occupancy
Na	3b	0	0	0	1
TM/Li	3a	0	0	0.5	0.897(3)
O	6c	0	0	0.23581(9)	1

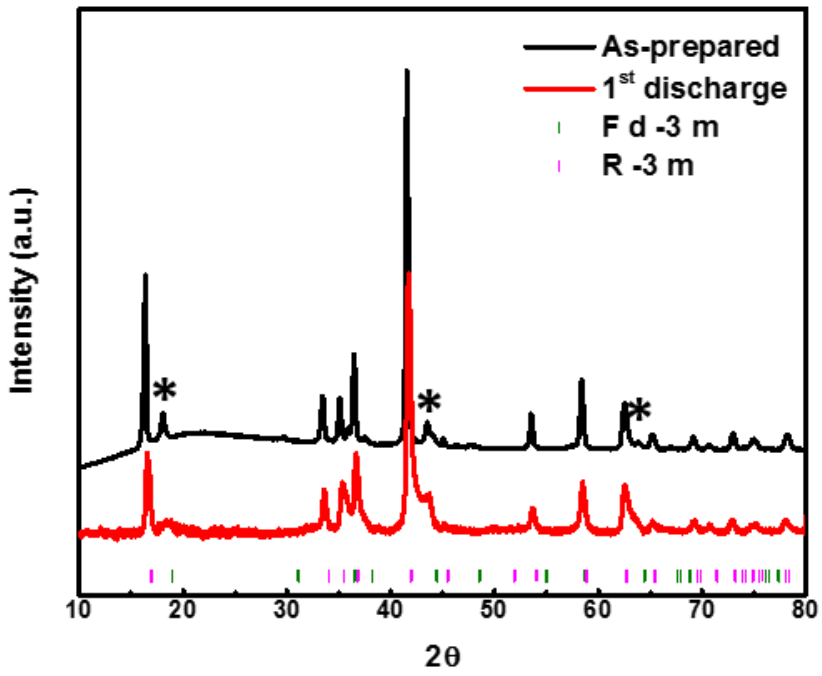

Figure 6. 4: XRD patterns of as-prepared and 1st discharged laminated LS-NFM electrode. The * mark in the figure indicates the pronounced spinel planes.

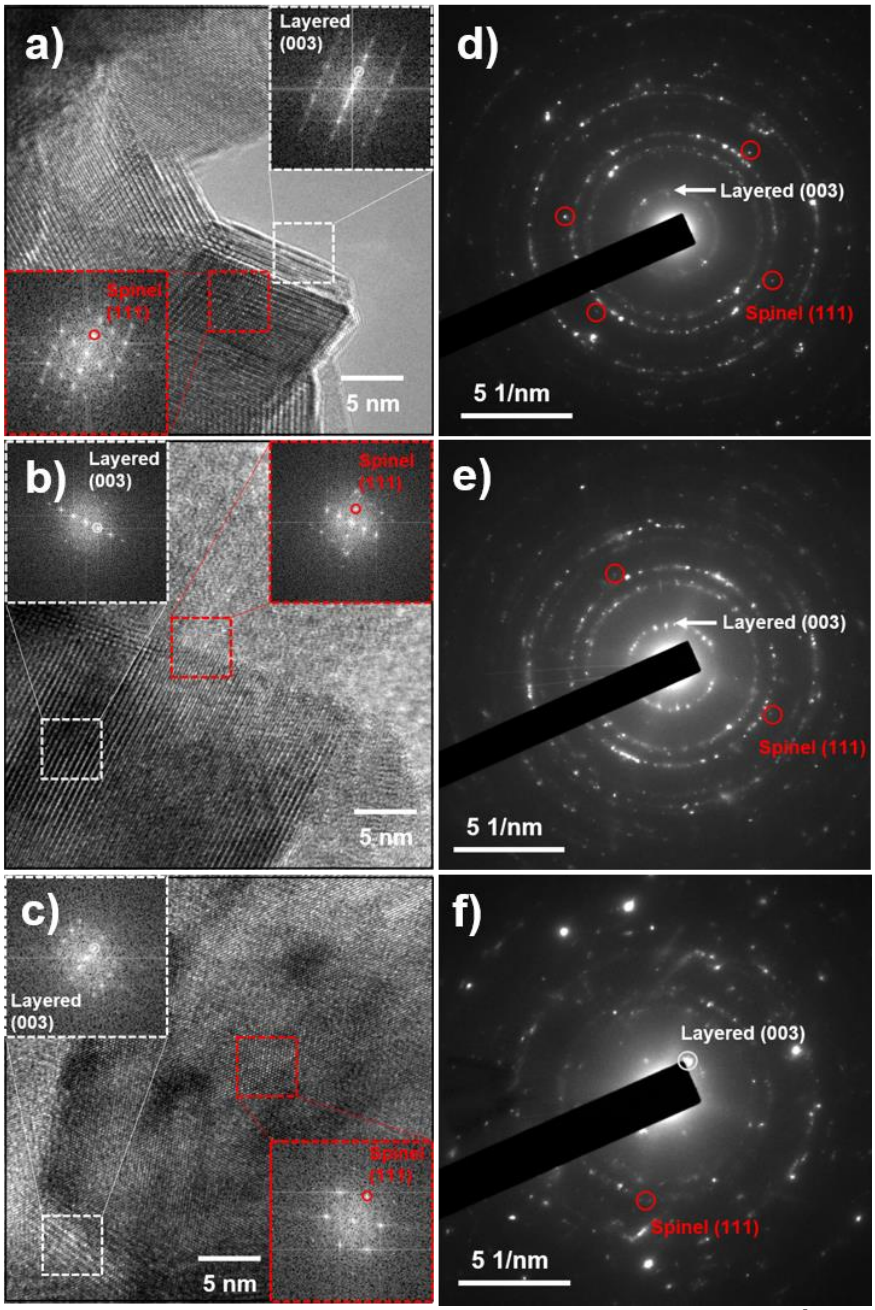

Figure 6. 5: HRTEM images of a) as-prepared, b) 1st discharged and c) 50th discharged LS-NFM sample. The red and white dashed square indicates the spinel and layered components, respectively, where the corresponding FFT images are shown as insets. The red and white circle indicate the spinel (111) plane with the zone axis [110] and layered (003) plane with the zone axis [100], respectively. The SAED images of d) as-prepared, e) 1st discharged and f) 50th discharged LS-NFM sample where the red circles and white arrows or circle indicate the planes from spinel and layered phase, respectively.

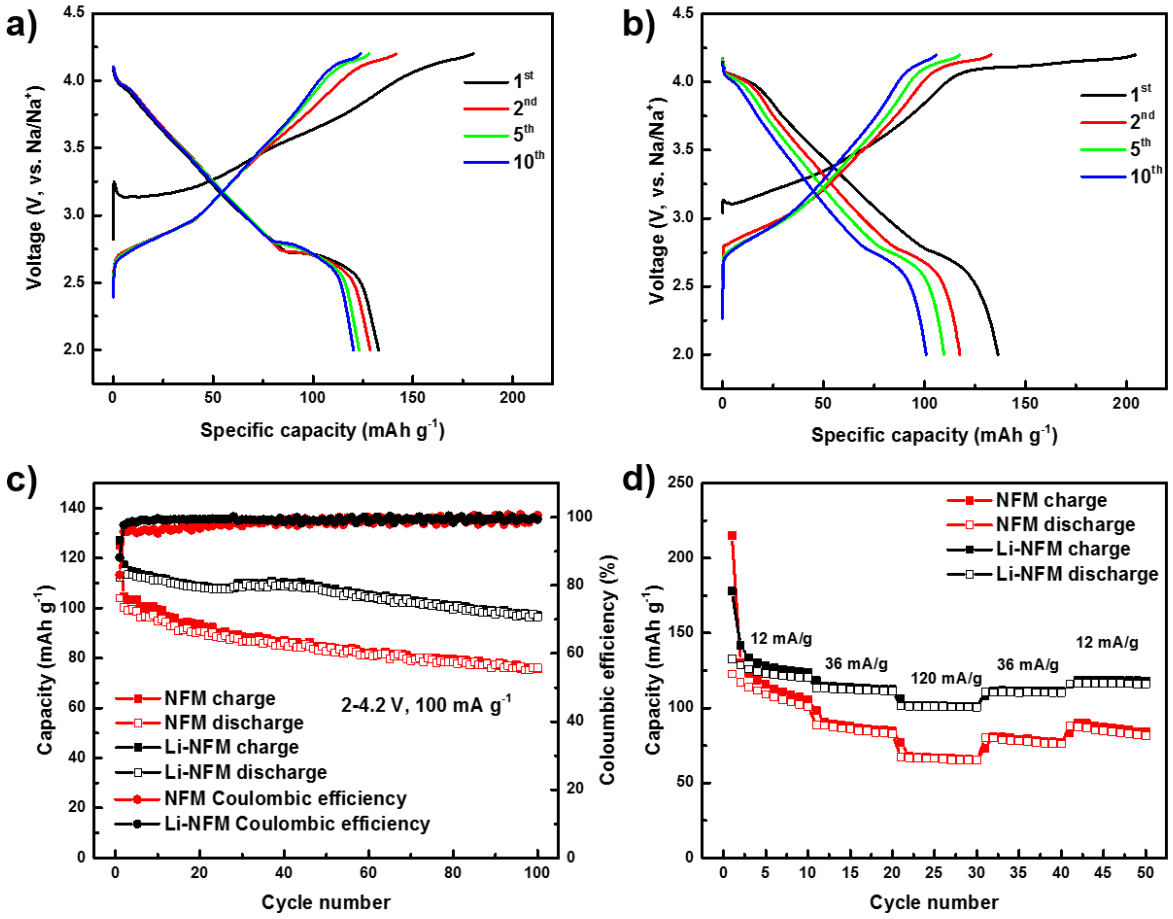

Figure 6. 6: Voltage profile of (a) LS-NFM and (b) NFM cathode cycled at a current rate of 12 mA g-1. (c) The cycling performance and (d) rate capability of LS-NFM and NFM cathode materials.

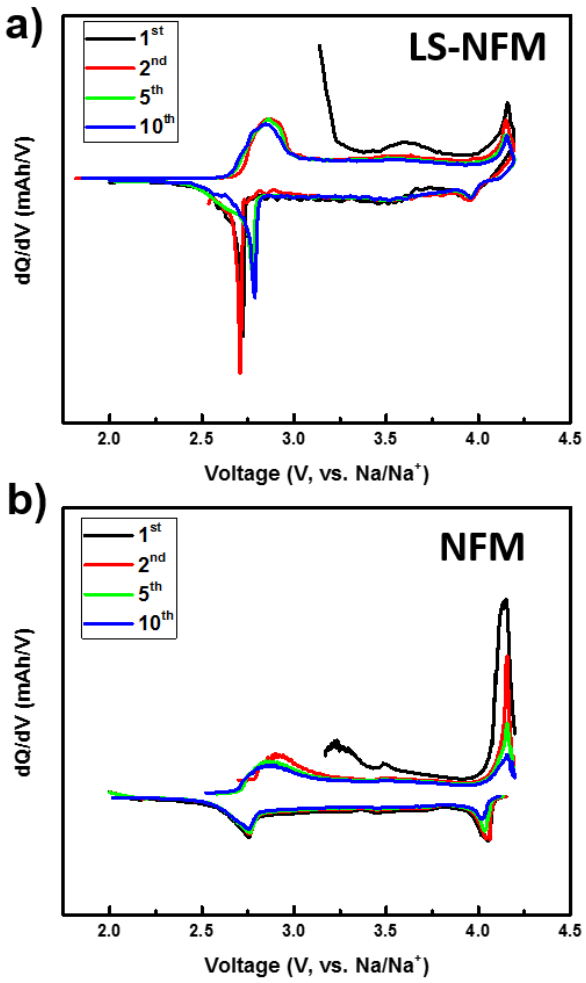

Figure 6. 7: The dQ/dV plots of a) LS-NFM and b) NFM sample

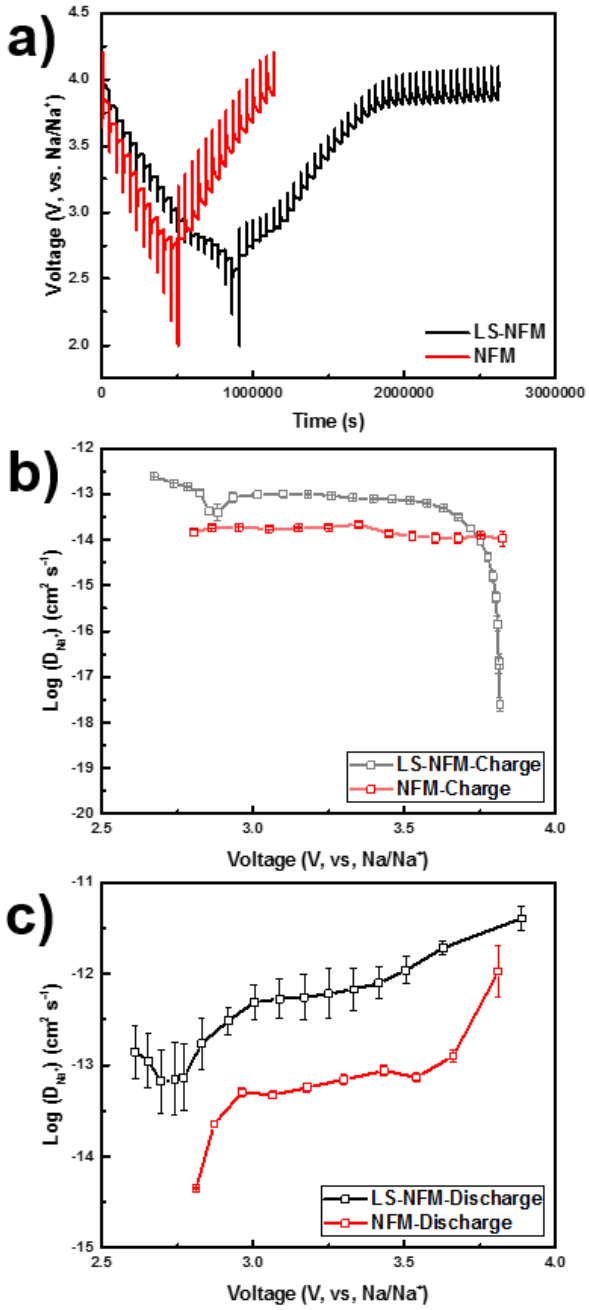

Figure 6. 8: (a) GITT profile. Na+ diffusivity as a function of voltage of LS-NFM and NFM cathodes in (b) charge and (c) discharge process.

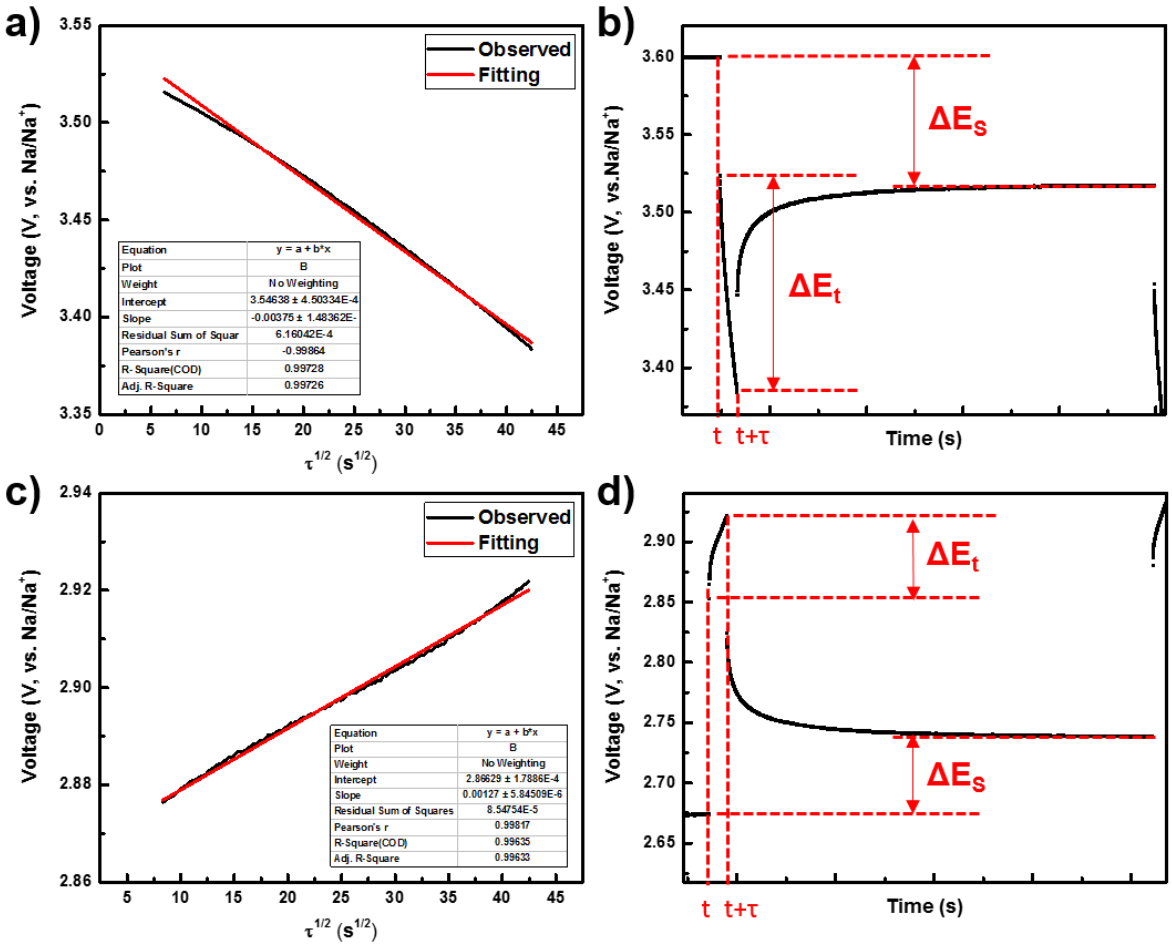

Figure 6. 9: Linear behavior of the E vs τ1/2 relationship in (a) discharge and (c) charge process. Schematic of GITT technique in (b) discharge and (d) charge process.

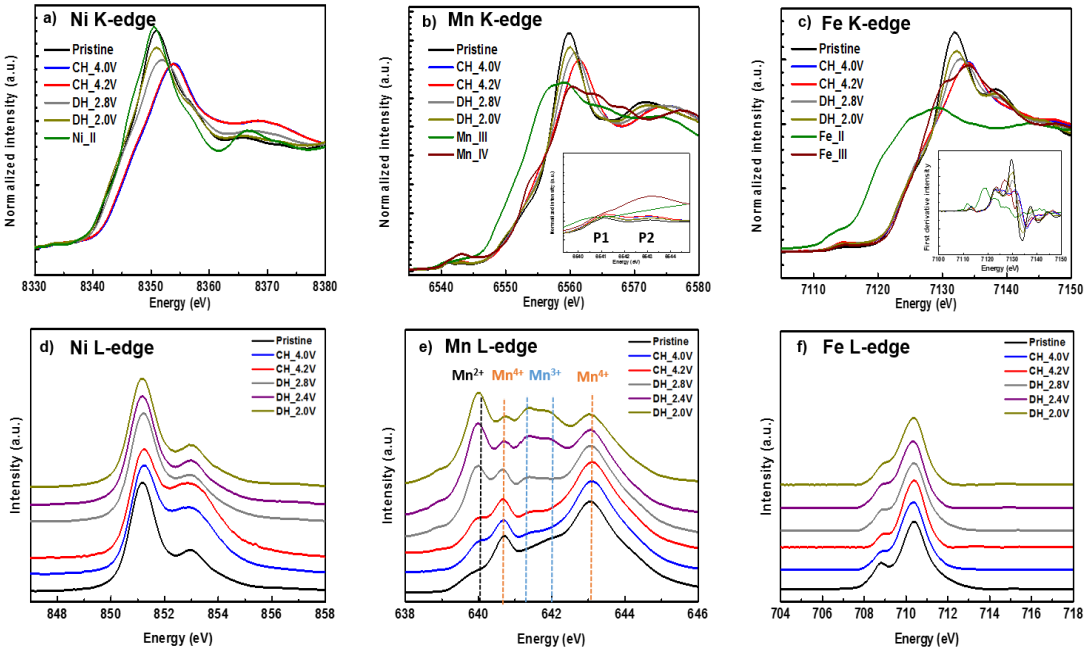

Figure 6. 10: ***Ex situ*** **(a) Ni, (b) Mn, (c) Fe K-edge XANES spectra of LS-NFM electrode at different SOCs during the first charging and discharging process. The inset in (b) shows the pre-edge features of Mn k-edge spectra of samples at different SOCs where P1 and P2 correspond to transitions from 1s to 3deg and 3dt2g with a weak crystal field, respectively. The inset in (c) shows the first-derivative curves of the original data. Ex situ (d) Ni, (e) Mn, (f) Fe L-edge sXAS spectra of LS-NFM electrode at different SOCs during the first charging and discharging process. The data were recorded under TEY mode.**

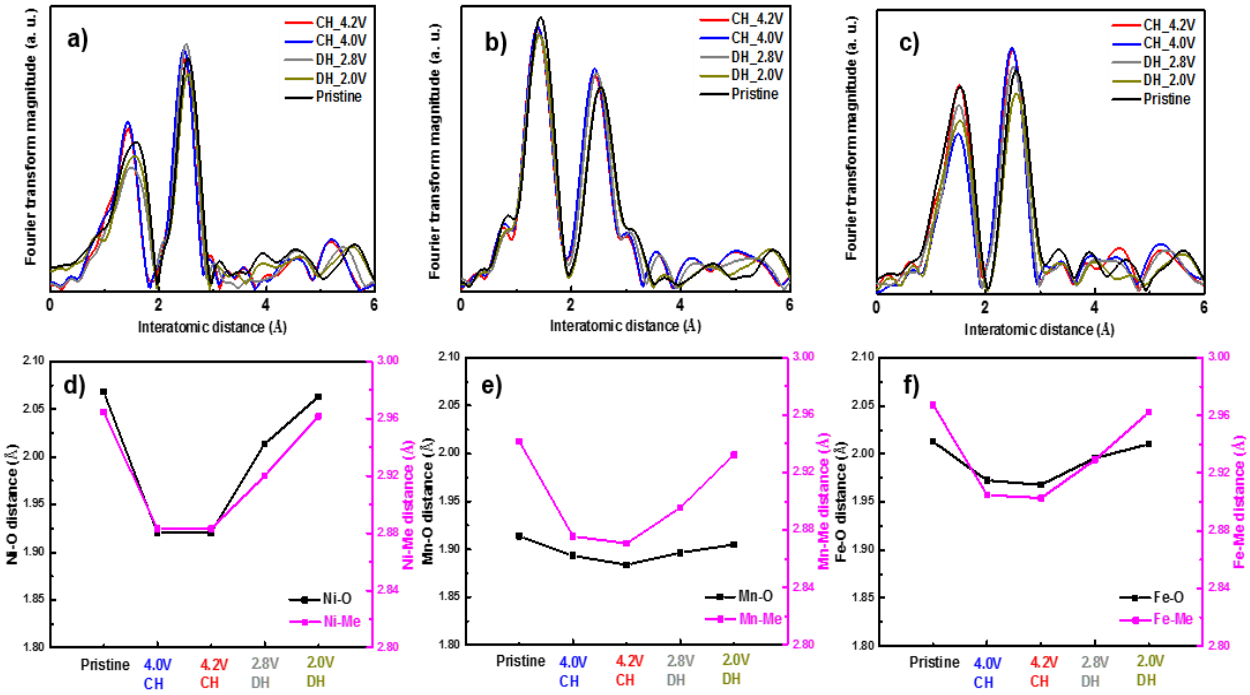

Figure 6. 11: ***Ex situ*** **Fourier transformed (a) Ni, (b) Mn, (c) Fe K-edge EXAFS spectra of LS-NFM electrode at different SOCs during the first charging and discharging process. Simulated TM-TM and TM-O distances of (d) Ni, (e) Mn, (f) Fe.**

Table 6.2 EXAFS fitting result of LS-NFM cathode.

	CN_Fe-O	CN_Fe-Me	R-factor	ΔE (eV)	σ^2_Fe-O (x10^{-3} Å^2)	σ^2_Fe-Me (x10^{-3} Å^2)	R_{Fe-O} (Å)	R_{Fe-Me} (Å)	k range (Å)	r range (Å)
Fe-AsPrep	6	6	0.016265	-7.0182	6.66864	5.38233	2.01284	2.96731	3~12	1~3
Fe-char-4V	6	6	0.156745	-7.7365	12.13892	6.13947	1.97241	2.90489	3~12	1~3
Fe-char-4.2V	6	6	0.021761	-3.0315	9.37328	6.71866	1.96781	2.9027	3~12	1~3
Fe-Dis-2.8V	6	6	0.012082	-7.4162	8.70901	6.80846	1.99566	2.92926	3~12	1~3
Fe-dis-2.0V	6	6	0.01471	-7.2333	8.59873	6.64996	2.01025	2.96228	3~12	1~3
	CN_Mn-O	CN_Mn-Me	R-factor	ΔE (eV)	σ^2_Mn-O (x10^{-3} Å^2)	σ^2_Mn-Me (x10^{-3} Å^2)	R_{Mn-O} (Å)	R_{Mn-Me} (Å)	k range (Å)	r range (Å)
Mn-AsPrep	6	6	0.023851	-5.9896	9.78389	4.0472	1.91375	2.94187	3~12	1~3
Mn-char-4V	6	6	0.021841	-7.4809	5.59903	4.17578	1.89319	2.87574	3~12	1~3
Mn-char-4.2V	6	6	0.024603	-8.9913	5.55543	4.89835	1.88377	2.87071	3~12	1~3
Mn-Dis-2.8V	6	6	0.016574	-7.1166	5.85161	5.18614	1.89643	2.89567	3~12	1~3
Mn-dis-2.0V	6	6	0.038514	-7.1010	6.887	4.17724	1.90484	2.93251	3~12	1~3
	CN_Ni-O	CN_Ni-Me	R-factor	ΔE (eV)	σ^2_Ni-O (x10^{-3} Å^2)	σ^2_Ni-Me (x10^{-3} Å^2)	R_{Ni-O} (Å)	R_{Ni-Me} (Å)	k range (Å)	r range (Å)
Ni-AsPrep	6	6	0.005136	-6.636	6.76932	5.19269	2.06801	2.96454	3~12	1~3
Ni-char-4V	6	6	0.014329	-11.3206	7.90576	5.55776	1.92072	2.88331	3~12	1~3
Ni-char-4.2V	6	6	0.01234	-10.6070	8.68799	5.94378	1.92051	2.88306	3~12	1~3
Ni-Dis-2.8V	6	6	0.006976	-4.3747	11.63148	5.88576	2.01353	2.91998	3~12	1~3
Ni-dis-2.0V	6	6	0.005932	-6.9073	8.13756	5.9196	2.06283	2.96158	3~12	1~3

6.6 References

(1) Ryu, W. H.; Nam, D. H.; Ko, Y. S.; Kim, R. H.; Kwon, H. S. *Electrochim. Acta* **2012**, *61*, 19.

(2) Yabuuchi, N.; Yano, M.; Yoshida, H.; Kuze, S.; Komaba, S. *J. Electrochem. Soc.* **2013**, *160*, A3131.

(3) Larson, A. C.; Von Dreele, R. B. *General Structure Analysis System (GSAS)*, Los Alamos National Laboratory, 2004.

(4) Newville, M. *J. Synchrotron Radiat.* **2001**, *8*, 322.

(5) Lee, E.; Lu, J.; Ren, Y.; Luo, X. Y.; Zhang, X. Y.; Wen, J. G.; Miller, D.; DeWahl, A.; Hackney, S.; Key, B.; Kim, D.; Slater, M. D.; Johnson, C. S. *Adv. Energy Mater.* **2014**, *4*.

(6) Clément, R. J.; Bruce, P. G.; Grey, C. P. *J. Electrochem. Soc.* **2015**, *162*, A2589.

(7) Oh, S. M.; Myung, S. T.; Hwang, J. Y.; Scrosati, B.; Amine, K.; Sun, Y. K. *Chem. Mater.* **2014**, *26*, 6165.

(8) Wang, X. F.; Liu, G. D.; Iwao, T.; Okubo, M.; Yamada, A. *J. Phys. Chem. C* **2014**, *118*, 2970.

(9) Nayak, P. K.; Grinblat, J.; Levi, M.; Levi, E.; Zitoun, D.; Markovsky, B.; Aurbach, D. *Materials Science and Engineering B-Advanced Functional Solid-State Materials* **2016**, *213*, 131.

(10) Li, X.; Wu, D.; Zhou, Y. N.; Liu, L.; Yang, X. Q.; Ceder, G. *Electrochem. Commun.* **2014**, *49*, 51.

(11) Yuan, D. D.; Wang, Y. X.; Cao, Y. L.; Ai, X. P.; Yang, H. X. *Acs Appl. Mater. Interfaces* **2015**, *7*, 8585.

(12) Li, X.; Wang, Y.; Wu, D.; Liu, L.; Bo, S. H.; Ceder, G. *Chem. Mater.* **2016**, *28*, 6575.

(13) Xie, Y. Y.; Wang, H.; Xu, G. L.; Wang, J. J.; Sheng, H. P.; Chen, Z. H.; Ren, Y.; Sun, C. J.; Wen, J. G.; Wang, J.; Miller, D. J.; Lu, J.; Amine, K.; Ma, Z. F. *Adv. Energy Mater.* **2016**, *6*.

(14) Sathiya, M.; Hemalatha, K.; Ramesha, K.; Tarascon, J. M.; Prakash, A. S. *Chem. Mater.* **2012**, *24*, 1846.

(15) Lei, Y. C.; Li, X.; Liu, L.; Ceder, G. *Chem. Mater.* **2014**, *26*, 5288.

(16) Park, Y.; Shin, S. H.; Hwang, H.; Lee, S. M.; Kim, S. P.; Choi, H. C.; Jung, Y. M. *J. Mol. Struct.* **2014**, *1069*, 157.

(17) Balasubramanian, M.; Lee, H. S.; Sun, X.; Yang, X. Q.; Moodenbaugh, A. R.; McBreen, J.; Fischer, D. A.; Fu, Z. *Electrochem. Solid-State Lett.* **2002**, *5*, A22.

(18) Yang, L.; Ravdel, B.; Lucht, B. L. *Electrochem. Solid-State Lett.* **2010**, *13*, A95.

(19) Komaba, S.; Yabuuchi, N.; Nakayama, T.; Ogata, A.; Ishikawa, T.; Nakai, I. *Inorg. Chem.* **2012**, *51*, 6211.

(20) Pan, H. L.; Hu, Y. S.; Chen, L. Q. *Energ. Environ. Sci.* **2013**, *6*, 2338.

(21) Chagas, L. G.; Buchholz, D.; Wu, L. M.; Vortmann, B.; Passerini, S. *J. Power Sources* **2014**, *247*, 377.

(22) Park, K.; Han, D.; Kim, H.; Chang, W. S.; Choi, B.; Anass, B.; Lee, S. *Rsc Adv.* **2014**, *4*, 22798.

(23) Bhaskar, A.; Krueger, S.; Siozios, V.; Li, J.; Nowak, S.; Winter, M. *Adv. Energy Mater.* **2015**, *5*.

(24) Yi, L. H.; Liu, Z. S.; Yu, R. Z.; Zhao, C. X.; Peng, H. F.; Liu, M. H.; Wu, B.; Chen, M. F.; Wang, X. Y. *Acs Sustain. Chem. Eng.* **2017**, *5*, 11005.

(25) Luo, D.; Li, G. S.; Fu, C. C.; Zheng, J.; Fan, J. M.; Li, Q.; Li, L. P. *Adv. Energy Mater.* **2014**, *4*.

(26) Nayak, P. K.; Grinblat, J.; Levi, M. D.; Haik, O.; Levi, E.; Talianker, M.; Markovsky, B.; Sun, Y. K.; Aurbach, D. *Chem. Mater.* **2015**, *27*, 2600.

(27) Nayak, P. K.; Levi, E.; Grinblat, J.; Levi, M.; Markovsky, B.; Munichandraiah, N.; Sun, Y. K.; Aurbach, D. *Chemsuschem* **2016**, *9*, 2404.

(28) Wang, P. F.; Yao, H. R.; Liu, X. Y.; Zhang, J. N.; Gu, L.; Yu, X. Q.; Yin, Y. X.; Guo, Y. G. *Adv. Mater.* **2017**, *29*.

(29) McBreen, J. *J. Solid State Electr.* **2009**, *13*, 1051.

(30) Yoon, W. S.; Balasubramanian, M.; Chung, K. Y.; Yang, X. Q.; McBreen, J.; Grey, C. P.; Fischer, D. A. *J. Am. Chem. Soc.* **2005**, *127*, 17479.

(31) Qiao, R. M.; Dai, K. H.; Mao, J.; Weng, T. C.; Sokaras, D.; Nordlund, D.; Song, X. Y.; Battaglia, V. S.; Hussain, Z.; Liu, G.; Yang, W. L. *Nano Energy* **2015**, *16*, 186.

(32) Ito, A.; Sato, Y.; Sanada, T.; Hatano, M.; Horie, H.; Ohsawa, Y. *J. Power Sources* **2011**, *196*, 6828.

(33) Oh, S. M.; Myung, S. T.; Yoon, C. S.; Lu, J.; Hassoun, J.; Scrosati, B.; Amine, K.; Sun, Y. K. *Nano Lett.* **2014**, *14*, 1620.

(34) Yue, J. L.; Yin, W. W.; Cao, M. H.; Zulipiya, S.; Zhou, Y. N.; Fu, Z. W. *Chem. Commun.* **2015**, *51*, 15712.

(35) Zhang, W.; Duchesne, P. N.; Gong, Z. L.; Wu, S. Q.; Ma, L.; Jiang, Z.; Zhang, S.; Zhang, P.; Mi, J. X.; Yang, Y. *J. Phys. Chem. C* **2013**, *117*, 11498.

(36) Ammundsen, B.; Jones, D. J.; Roziere, J.; Burns, G. R. *Chem. Mater.* **1996**, *8*, 2799.

(37) Lin, F.; Liu, Y. J.; Yu, X. Q.; Cheng, L.; Singer, A.; Shpyrko, O. G.; Xing, H. L. L.; Tamura, N.; Tian, C. X.; Weng, T. C.; Yang, X. Q.; Meng, Y. S.; Nordlund, D.; Yang, W. L.; Doeff, M. M. *Chem. Rev.* **2017**, *117*, 13123.

(38) Yang, W.; Devereaux, T. P. *J. Power Sources* **2018**, *389*, 188.

(39) Lin, F.; Nordlund, D.; Markus, I. M.; Weng, T. C.; Xin, H. L.; Doeff, M. M. *Energ. Environ. Sci.* **2014**, *7*, 3077.

(40) Liu, X. S.; Wang, D. D.; Liu, G.; Srinivasan, V.; Liu, Z.; Hussain, Z.; Yang, W. L. *Nat. Commun.* **2013**, *4*.

(41) Qiao, R. M.; Wang, Y. S.; Olalde-Velasco, P.; Li, H.; Hu, Y. S.; Yang, W. L. *J. Power Sources* **2015**, *273*, 1120.

(42) Hunter, J. C. *J. Solid State Chem.* **1981**, *39*, 142.

(43) Yang, S. L.; Wang, D. N.; Liang, G. X.; Yiu, Y. M.; Wang, J. J.; Liu, L. J.; Sun, X. L.; Sham, T. K. *Energ. Environ. Sci.* **2012**, *5*, 7007.

(44) Brown, I. D.; Shannon, R. D. *Acta Crystallogr. A* **1973**, *A 29*, 266.

(45) Shannon, R. D. *Acta Crystallogr. A* **1976**, *32*, 751.

CONCLUSIONS

This dissertation investigates the fundamental mechanism and potential improvement of TiO_2 anode and layered $NaNi_xFe_yMn_xO_2$ cathodes for sodium ion batteries (SIB). SIBs are attractive for large-scale energy storage system due to its high round trip efficiency and long cycle life as well as low cost and abundant raw materials. Recent studies suggest that various TiO_2 polymorphs are capable of anode materials. However, the impact of crystallinity on the electrochemical performance is lacking ininvestigation. Meanwhile, a $NaNi_xFe_yMn_xO_2$ cathode exhibits promising performance but detrimental irreversibility as well as poor stability and rate capability remain a problem.

In this dissertation, the TiO_2 anode and layered oxide cathode materials are investigated for sodium ion batteries, which contain three subjects: 1. The impact of crystallinity on anatase TiO_2 anode material (Chapter 4); 2. The origin of irreversibility in layered cathode materials (Chapter 5); 3. Li-substituted layered-spinel cathode material (Chapter 6).

In Chapter 4, amorphous, partially-crystalline and fully crystalline TiO_2 nanoparticles are successfully prepared by a sol-gel process with different heat treatments. The increase of crystallinity leads to better electrochemical performance in terms of Coulombic efficiency, rate capability and cycle life. CV suggests the irreversible Na insertion process of an A-TiO_2 sample which possibly resulted in the lower specific capacity and Coulombic efficiency than that of the PC-TiO_2 and FC-TiO_2 samples. GITT

suggests that more crystallinity leads to a larger diffusion coefficient. It is consistent with the rate capability where the crystalline TiO_2 sampleshave a higher specific capacity than amorphous ones. In addition to electrochemical evaluation, PDF is conducted to understand the structural evolution related to the performance. The corner-shared Ti-Ti distance through Na ion diffusion pathway increases with the increase of crystallinity, leading to expanded diffusion channels and therefore more active sites and faster diffusion. Though the Ti-Ti distance decreases for all TiO_2 samples after the Na ion insertion and/or extraction process due to the irreversible phase transition, the FC-TiO_2 sample shows a strong amplitude and well-defined peak, suggesting a great Ti-Ti ordering which possibly contributes to the great rate capability and cycle life performance.

In Chapter 5, we prepared NFM-Fe1/3, NFM-Fe05 and NFM-Fe08 to study the irreversibility in various cation compositions and different operation voltage windows. SEM images of all $Na_{1.05}Ni_yFe_xMn_yO_2$ cathodes show the micro-scale particles and flakes with similar particle size. The crystalline structure of $Na_{1.05}Ni_yFe_xMn_yO_2$ cathodes is investigated by XRD and Rietveld refinement where the O3-type layered α-$NaFeO_2$ structure (space group: R-3m) is obtained. The electrochemical performance of $Na_{1.05}Ni_yFe_xMn_yO_2$ cathodes was evaluated within the potential windows of 2.0-4.0V and 2.0-4.3V. The irreversibility became pronounced and the electrochemical performance became limited with the increase of either Fe composition or the upper cutoff potential. *Ex situ* XANES is conducted to understand the TM valence evolution. It reveals that Ni and Fe^{3+}/Fe^{4+} redox couple contributes to most of the specific capacity. The irreversibility resulted from TM valence is mainly attributed to Ni redox couple. The Fe1/3-2-4 exhibits

negligible irreversibility, however, Fe1/3-2-4.3 shows pronounced irreversibility at the high potential region, possibly due to the large overpotential. Moreover, the Fe08-2-4 shows a large irreversibility at low potential region, possibly resulting from the intrinsic electrochemical properties of the material. We also performed the EXAFS to investigate the structural evolution, particularly TM-O radial distance. It confirms that the specific capacity of Fe1/3-2-4, Fe1/3-2-4.3 and Fe08-2-4 mostly corresponds to the Ni^{2+}/Ni^{4+} and Fe^{3+}/Fe^{4+} redox couple. Ni-O distance mainly contributes to the irreversibility as well. Though the Fe1/3-2-4.3 show irreversibility in terms of Ni oxidation state, there is negligible structural irreversibility related to the Ni-O distance on Fe1/3-2-4.3 sample. The Fe08-2-4 sample has large irreversibility of the Ni-O distance at the low potential region, consistent with the irreversibility of Ni oxidation state.

In Chapter 6, we successfully prepared a layered-spinel cathode material for sodium ion batteries by Li substitution. The Rietveld refinement on the XRD pattern suggests that the as-prepared material is composed of a 94 % dominant O3-type layered phase and 6% secondary spinel phase. The HRTEM results show the remarkable structural compatibility and connectivity of the two components, indicating an intergrowth structure. In terms of the electrochemical performance, both cycling stability and rate capability have been significantly improved in LS-NFM cathodes compared to the un-doped NFM control. Moreover, the diffusivity of Na ions in LS-NFM during the discharge process is also approximately one magnitude higher than that in the NFM sample throughout the whole potential window. It explains the superior rate capability of the LS-NFM electrode. The enhanced charge transport kinetics can be explained by the improved ion diffusion through direct channels between the 2D layered and 3D spinel

component. The voltage profile of LS-NFM shows a reversible plateau above 4.0V while the high voltage plateau of the NFM cathode is irreversible, suggesting the enhanced structural and electrochemical stability of the LS-NFM cathode by the addition of the spinel phase. We further investigated the origin of the enhanced electrochemical performance in the LS-NFM cathode by *ex situ* XAS. Both hard/soft XAS results suggest that Ni^{2+}/Ni^{4+} and Fe^{3+}/Fe^{4+} redox couple are electrochemically active while Ni^{2+}/Ni^{4+} redox couple contributes to most of the capacity in LS-NFM cathode. Moreover, the XAS results suggest great reversibility of the redox pairs and crystal structure, which presumably is associated with the intergrowth of spinel and layered phase that stabilized the crystal structure above 4.0V.

Overall, we studied the fundamentals and improvements of TiO_2 anodes and layered $NaNi_xFe_yMn_xO_2$ cathodes for sodium ion batteries. With this study, we have broadened the field of knowledge on the crystallinity of TiO_2 anode, irreversibility and Li-substitution of $NaNi_xFe_yMn_xO_2$ cathodes. Sodium ion batteries are a promising candidate for the surging demand of large-scale energy storage systems. This study provides perspectives on basic understanding and performance enhancement of TiO_2 anodes as well as $NaNi_xFe_yMn_xO_2$ cathodes. We believe it will contribute to both academic research and commercial application of sodium ion batteries.